frontiers in
NEUROENGINEERING

ORIGINAL RESEARCH ARTICLE
published: 19 April 2012
doi: 10.3389/fneng.2012.00006

# Non-linear blend coding in the moth antennal lobe emerges from random glomerular networks

***Alberto Capurro*[1]*, *Fabiano Baroni*[2], *Shannon B. Olsson*[3], *Linda S. Kuebler*[3], *Salah Karout*[1], *Bill S. Hansson*[3] *and Timothy C. Pearce*[1]**

[1] *Department of Engineering, Centre for Bioengineering, University of Leicester, Leicester, UK*
[2] *Department of Electrical and Electronic Engineering, The University of Melbourne, Melbourne, VIC, Australia*
[3] *Department of Evolutionary Neuroethology, Max-Planck-Institute for Chemical Ecology, Jena, Germany*

***Edited by:***
*Thomas Nowotny, University of Sussex, UK*

***Reviewed by:***
*Martin Nawrot, Freie Universität Berlin, Germany*
*Kerem Muezzinoglu, SAS Institute, USA*

***Correspondence:**
*Alberto Capurro, Department of Engineering, University of Leicester, Leicester LE1 7RH, UK.*
*e-mail: ac331@le.ac.uk; alberto.capurro@gmail.com*

Neural responses to odor blends often exhibit non-linear interactions to blend components. The first olfactory processing center in insects, the antennal lobe (AL), exhibits a complex network connectivity. We attempt to determine if non-linear blend interactions can arise purely as a function of the AL network connectivity itself, without necessitating additional factors such as competitive ligand binding at the periphery or intrinsic cellular properties. To assess this, we compared blend interactions among responses from single neurons recorded intracellularly in the AL of the moth *Manduca sexta* with those generated using a population-based computational model constructed from the morphologically based connectivity pattern of projection neurons (PNs) and local interneurons (LNs) with randomized connection probabilities from which we excluded detailed intrinsic neuronal properties. The model accurately predicted most of the proportions of blend interaction types observed in the physiological data. Our simulations also indicate that input from LNs is important in establishing both the type of blend interaction and the nature of the neuronal response (excitation or inhibition) exhibited by AL neurons. For LNs, the only input that significantly impacted the blend interaction type was received from other LNs, while for PNs the input from olfactory sensory neurons and other PNs contributed agonistically with the LN input to shape the AL output. Our results demonstrate that non-linear blend interactions can be a natural consequence of AL connectivity, and highlight the importance of lateral inhibition as a key feature of blend coding to be addressed in future experimental and computational studies.

**Keywords: olfaction, computational modeling, neural circuits, mixture processing, synaptic input, inhibitory interneurons, *Manduca sexta***

## INTRODUCTION

Biological neural networks organize sensory inputs to produce a meaningful experience of the environment, but the way in which complex perceptual representations are produced by the olfactory system is not completely understood. For this reason, an understanding of the relation between the neural representation of a mixture and its single components constitutes an important problem in basic neuroscience. Moreover, such analyses can reveal general properties of perceptual representation in the nervous system, and derive principles that may be widely extended across species and sensory modalities (e.g., Rabinovich et al., 2008).

Natural odors are complex mixtures of different compounds. Within the olfactory system, the components of a blend often interact in a non-linear fashion within the olfactory system to affect the resultant neuronal response. This gives rise to so-called mixture interactions (Laing et al., 1989; Duchamp-Viret et al., 2003). The first interaction type is suppression, where the response to the mixture is less than at least one of the single components alone. A related category, in which the mixture evokes a response that is equivalent to the most effective single component, is known as hypoadditivity. The final interaction type is synergism, in which the mixture induces a response that is greater than the addition of the responses to the single components. A special case is linear addition, in which there is no interaction between the components, so the mixture evokes a response that is equal to the component sum.

The antennal lobe (AL) is the first synaptic relay in the olfactory pathway of insects, analogous to the mammalian olfactory bulb (for recent comparative review, see Martin et al., 2011). It consists of spheroidal bundles of neuropil known as glomeruli that contain synaptic contacts between receptors and second-order neurons. The axons of olfactory sensory neurons (OSNs) in the antennal nerve contact projection neurons (PNs) that constitute the output of the AL, and local interneurons (LNs) that communicate with other glomeruli. OSNs having the same type of receptor protein contact a specific glomerulus, giving rise to a spatial representation of chemical identity. In moths, approximately 250,000 OSNs from the antenna converge onto roughly 900 PNs and 360 LNs (Homberg et al., 1989; **Figure 1**). Interneurons in moths generally exhibit a broad symmetrical arborization pattern, contacting the majority of AL glomeruli (Manduca sexta: Matsumoto and Hildebrand, 1981; Kuebler et al., 2011; Reisenman et al., 2011). Although excitatory LNs have been found in *Drosophila* (Shang et al., 2007; Huang et al.,

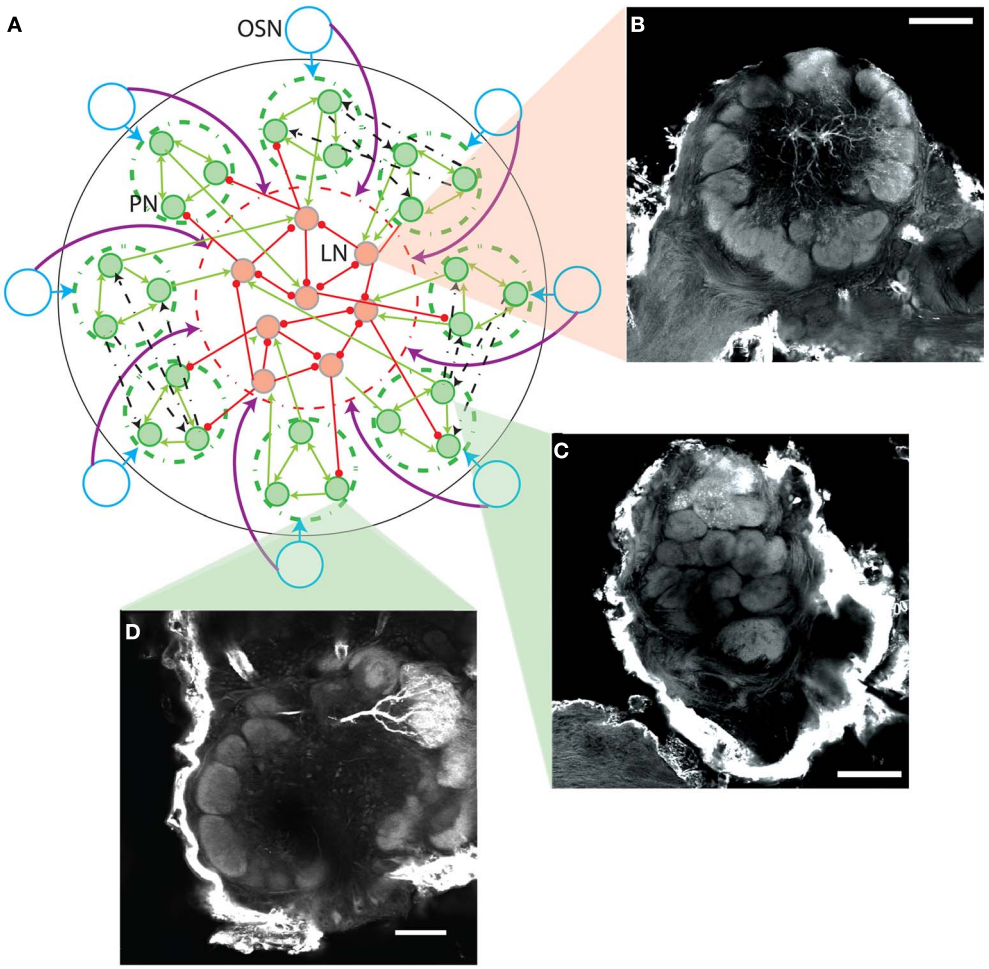


**FIGURE 1 | (A) Scheme of AL model network connectivity.** Each of the eight OSN types (blue circles) contact only PNs in their corresponding glomerulus (green dashed circles) as indicated by the blue arrows. OSN types contact every LN, as indicated by the purple arrows reaching the dashed red circle containing the LNs. The PNs have reciprocal excitation within the same glomerulus (green arrows within the dashed green circles), can contact the LNs (green arrows entering the dashed red circle), and have reciprocal multiglomerular excitatory contacts with another single glomerulus (dashed black arrows show a few examples). The LNs have reciprocal inhibition and can contact the PNs (red lines ending in circles). **(B–D)** Neuromorphic basis for the AL model. Confocal micrographs show three female *M. sexta* ALs with lines indicating their representative location in the model schema of **A**. Each panel extracts a single optical orthogonal slice. Neurobiotin-injected cells were stained with Alexa-conjugated Streptavidin. Pictures were obtained by confocal microscopy of three separate whole mount brain preparations using a 10×, 0.45-NA objective lens (C-Apochromat, Zeiss). Optical sections (1024 × 1024 pixel) were taken at intervals of 0.8 μm. **B** displays a lateral interneuron, while **C** and **D** show a multiglomerular and uniglomerular PN, respectively; scale bar: 100 μm.

2010), to date only inhibitory LNs have been located in moths (e.g., Reisenman et al., 2011). However, excitatory PNs that innervate two or more neighboring glomeruli have been identified in *Manduca sexta* hawkmoths (Homberg et al., 1988; Kuebler et al., 2011; **Figure 1**), and could provide a form of potential lateral excitation within the moth AL.

There exists considerable evidence indicating that the insect AL is not simply a relay station in the olfactory pathway, but constitutes the primary processing centre for blend information of the insect brain (e.g., Joerges et al., 1997; Linster and Smith, 1997; Hansson and Anton, 2000; Galizia and Menzel, 2001; Linster et al., 2005; Deisig et al., 2006, 2010; Carlsson et al., 2007; Silbering and Galizia, 2007; Krofczik et al., 2008; Lei and Vickers, 2008; Fernandez et al., 2009; Riffell et al., 2009a,b; Yamagata et al., 2009; Kuebler et al., 2011; Meyer and Galizia, 2011). Odor mixtures have been found to elicit mainly suppressive and hypoadditive responses within the insect AL, while examples of synergism are rare, as evidenced by both calcium imaging (e.g., Deisig et al., 2006, 2010; Carlsson et al., 2007; Silbering et al., 2008; Yamagata et al., 2009) and electrophysiological studies (e.g., Krofczik et al., 2008; Riffell et al., 2009a; Kuebler et al., 2011). In moths in particular, mixture interactions have been suggested to occur at the level of OSNs (e.g., Carlsson and Hansson, 2002; Hillier and Vickers, 2011) but are more commonly observed in second order neurons (e.g., Christensen et al., 1991; Lei and Vickers, 2008; Pinero et al., 2008).

In this study, we are interested in the network processing within the AL as a potential source of non-linear interactions between single components in the response to a blend. To assess this, we constructed a morphologically based computational model including populations of interconnected PNs and LNs using probabilistic rules. Parameters were calibrated to match the excitation/inhibition proportion observed in physiological recordings of AL neurons of the moth *M. sexta* (Kuebler et al., 2011). The model predicted most of the proportions of blend interactions found in the data, and the results are robust to changes in many parameters due to the underlying probabilistic connectivity. Finally, we used the model to investigate how different types of non-linear blend interactions could arise in terms of the synaptic input received by the PNs and LNs. We focused on the mean values of synaptic input during odor stimulus and control conditions, leaving the influence of the dynamic patterns of neural activity for a future study. Our results indicate that the array of blend interactions observed in the biological data can arise from network connectivity alone via sub-networks of inhibitory interneurons without requiring special intrinsic properties of the neurons themselves.

## METHODS

### NEURONAL RECORDINGS AND ODOR STIMULATION

We used intracellular recordings and morphological observations of AL neurons performed in the moth *M. sexta* (Lepidoptera, Sphingidae) by Kuebler et al. (2011), in addition to previous studies (see citations in "Network connectivity of the model") to construct a computational model of AL processing. The model parameters were calibrated to reproduce the proportion excitation/inhibition found in their physiological recordings (see "Network connectivity of the model"), and subsequently the proportions of blend interactions predicted by the model were independently compared with the recordings as a way of validating the model (**Figures 3** and **4**), which was in turn used to assess the role of synaptic input on the emergence of blend interactions (**Figures 5–8**). We include here a brief description of the recording methods (for full details see Kuebler et al., 2011).

Projection and interneurons were recorded intracellularly using sharp glass electrodes and stimulated for 500 ms at $10^{-4}$ dilution (in mineral oil) with (+) linalool, (−) linalool, phenyl acetataldehyde, benzaldehyde, hexanol, nonanal, or *trans*-2-hexenyl acetate (used instead of nonanal in some experiments), and *cis*-3-hexenyl acetate. Stimulus concentrations were equilibrated according to vapor pressure using a multicomponent stimulus device (Olsson et al., 2011). Neurons were presented with each of the seven odors separately, and the odors eliciting a response were tested together at the same concentration as a "blend." Active single components were finally tested separately at the total blend concentration. Mixture interactions were assessed as described below from response frequencies for each stimulus presentation, normalized to spontaneous activity as a ratio (Hz 1.5 s after stimulus onset/Hz 1.5 s before onset; including mechanical stimulus delay).

The complete data set consisted of 31 neurons tested each in one trial with the complete stimulus protocol. From this number, 20 neurons responded with excitation (including biphasic responses) and 11 responded with inhibition. Most of the recorded neurons (29 out of 31) could be classified as PNs or LNs by morphological analysis or by measuring the spike width, which nearly twice as large in LNs (for details see Kuebler et al., 2011). The cells that were morphologically labeled were 9 PNs and 5 LNs, while the criterion of the spike width allowed to classify 12 cells as PNs and 5 as LNs.

### COMPUTATIONAL MODEL

#### *Neuronal model*

Individual neuron dynamics of LNs and PNs were modeled using a first-order differential equation (Chong et al., 2012) that described the evolution of the firing-rate activation variable of a neuron over time:

$$\tau \frac{da_i}{dt} = -a_i(t) + S\left(\sum_{j\in P} w_{i,j}a_j(t) + \sum_{k\in L} w_{i,k}a_k(t) + \sum_{d\in R} v_{i,d}r_d\right)$$

with $S(x) = x^3/(0.5^3 + x^3)$ for $x \geq 0$,

and $S(x) = 0$ for $x < 0$,

where $a_i$ is the activation level of the $i$-th neuron, $P$ is the subset of PN neurons, $L$ is the subset of LN neurons, $R$ is the subset of OSN neurons, $w_{i,j}$ is the strength of synaptic influence of $j$ on the activity of $i$ (similarly for $w_{i,k}$), $v_{i,d}$ is the strength of synaptic influence of the $d$-th OSN type on the activity of cell $i$-th, and $r_d$ is the activity of the $d$-th OSN type. For PNs, $v_{i,d}$ is non-zero only for the connections coming from its corresponding OSN. $S$ is a sigmoid function that limits the neuronal activity to values between 0 and 1. $\tau$(10 ms for PNs and 20 ms for LNs) is the time constant of neuronal dynamics. We assumed that the larger dendritic ramifications of LNs can make them slower than the PNs, as has been done in previous articles that modeled the AL (e.g., Linster and Cleland, 2010; Chong et al., 2012).The neuronal activation function $S(x)$ (Chong et al., 2012) has a sigmoidal shape that accounts for saturation in activation level at high input values. We did not include noise added to each time step, but the initial values of $a_i$ used in each realization were taken from a Gaussian random distribution with $\mu = 0.01$ and $\sigma = 0.0025$. The pre-stimulation control period started 200 ms after the onset of the simulation, when the system had already reached its resting state, so the transients due to the initial conditions (visible at times <50 ms in **Figure 2**) did not influence the results shown in **Figures 3–8**.

#### *Network connectivity of the model*

**Figure 1A** shows a general scheme of the network connectivity pattern. For simplicity only a few neurons of each type are represented, PNs with green filled circles and LNs with red filled circles. Excitatory synaptic contacts are represented with lines ending in arrow heads, and inhibitory contacts with lines ending in circles.

The model considers eight OSN types and eight glomeruli with 15 PNs each, making a total of 120 PNs. The total number of LNs was set to 40, resulting in a ratio PN/LN of three, which is realistic for the moth AL (Homberg et al., 1989). Thus, we are making a proportional reduction ($x = 8.75$) of the glomeruli number in the biological system of *M. sexta* (which is around 70; Grosse-Wilde et al., 2011), keeping a realistic number of PNs per glomerulus

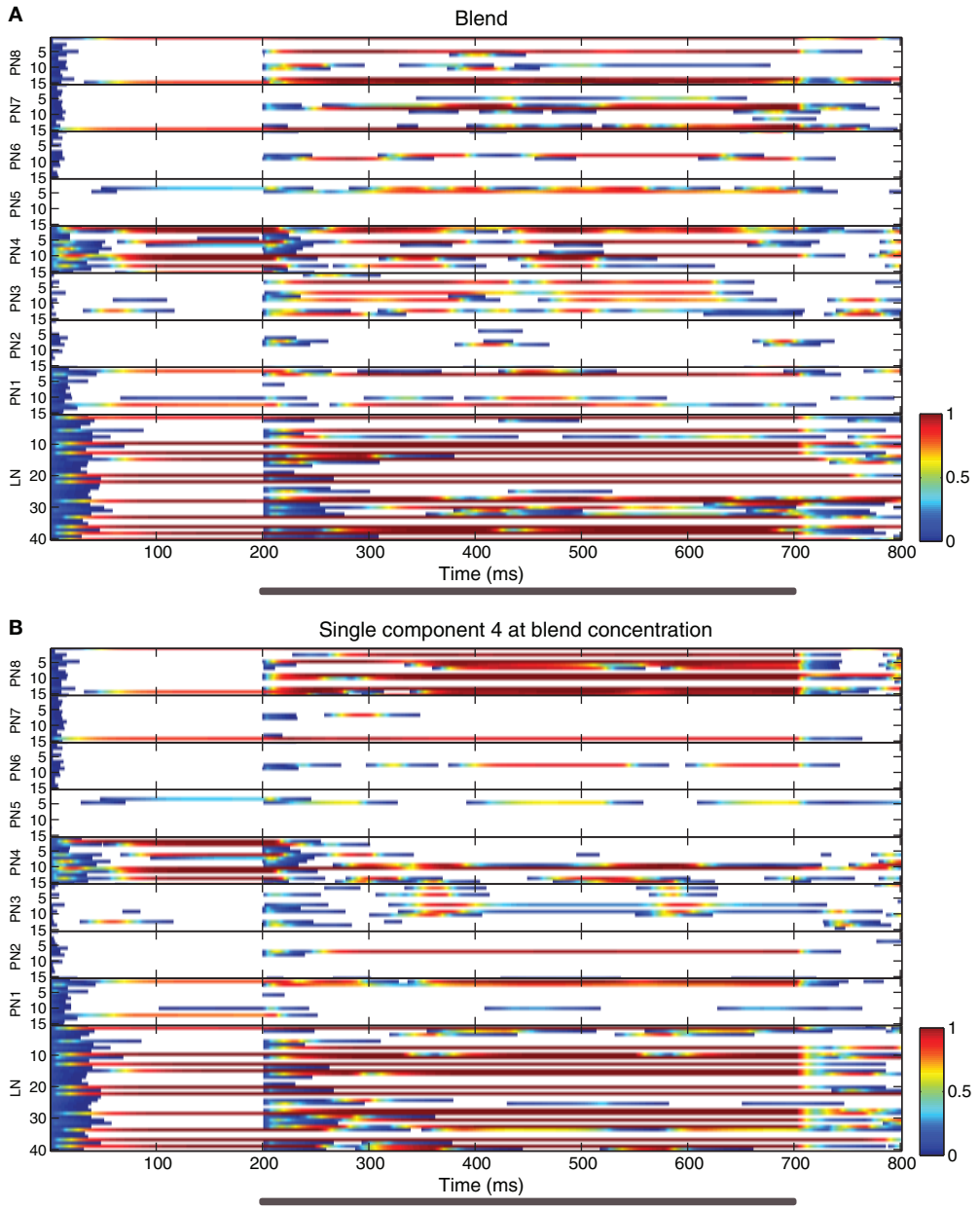


**FIGURE 2 | Raster plots showing neuron activity in an example realization of the AL model. (A)** Response to the homogeneous blend. **(B)** Response to a single component at blend concentration. The activity variable of each neuron is represented by a color code (shown in the scale bars at the lower right side of each panel) plotted against time. The ordinate's axis indicates the index numbers of the neurons: PNs belonging to each of the eight glomeruli (labeled PN 1 to PN 8, with 15 PNs per glomerulus) and 40 multiglomerular LNs (labeled LN). Odor stimulus duration is marked with gray bars under the abscissas.

and PN/LN proportions. This reduction resulted in a network scale in which the dynamic behavior of the model can be captured without an excessive increase in computational burden. We checked that the results regarding the proportions of blend interactions did not change significantly for a scaled-up version of the model having 64 glomeruli.

The connectivity between the different cell types is specified by its weight and connection probability. In each realization of the model, the values provided below for the weights were perturbed with Gaussian noise of mean zero and σ equal to 5% of the weight. OSNs of a given type are represented as a single unit (blue circles and arrows in **Figure 1A**) and only project to PNs of the corresponding glomerulus (dashed green circles) with a synaptic weight of 2.0. This configuration retains the generally dogmatic 1:1 principle between OSN type and glomerulus (Ressler et al., 1994; Mombaerts, 1996; Vosshall, 2000; Baker, 2008; Bruyne and Baker, 2008). Thus, the PNs of each glomerulus were activated only by their corresponding receptor type, as indicated by the blue

arrows. In contrast, the eight receptor types contacted every LN with a synaptic weight of 2.0, as indicated by the purple arrows of **Figure 1A**. Given the high convergence ratio between OSNs and other AL neurons within each glomerulus (300:1 for OSNs:PNs, ∼1000:1 for OSNs:LNs; Homberg et al., 1989), the connection probability of OSN to PN or LN contacts was set at 1.0.

The probabilistic rules used to establish the connectivity pattern of the network shown in **Figure 1A** are based on morphological studies of the *M. sexta* moth AL (e.g., Homberg et al., 1989), and also on direct observations performed by members of our group (**Figures 1B–D**). The location of the cells displayed in the morphological images in the context of the network scheme is indicated with triangular zooms. Here, we show the three major types of AL neurons recorded in the physiological study (Kuebler et al., 2011). As noted previously (Kuebler et al., 2011; Reisenman et al., 2011), LNs in the AL of the moth exhibited a broad, symmetrical arborization pattern throughout the AL (**Figure 1B**), interconnecting a large proportion of the glomeruli, as originally described (Matsumoto and Hildebrand, 1981). PNs exhibited two types of arborization patterns (Homberg et al., 1988). The majority of recorded PNs arborized in a single AL glomerulus, thus synapsing only with other PNs and LNs within that glomerulus (**Figure 1D**). However, a small proportion (2:8) of the stained PNs (Kuebler et al., 2011) arborized in two or more glomeruli (**Figure 1C**), thus synapsing with neurons within neighboring glomeruli.

To reflect these morphological observations in our model, PNs could have excitatory connections with other PNs of the same glomerulus with probability 0.8 and weight 0.37 (green arrows within the green dashed circles). In each glomerulus, we also randomly chose two PNs that could potentially contact PNs of another randomly chosen glomerulus with probability of 0.8 and weight 1.25 (the dashed black arrows in **Figure 1A** show only some examples). When a given glomerulus A received this type of contact from another glomerulus B, then B also innervated A with the same rule. In this way, each glomerulus was paired with another single glomerulus through this reciprocal excitatory connectivity (e.g., multi-glomerular PNs; **Figure 1C**). In the morphological data, we observed that multi-glomerular PNs generally innervated 2–3 neighboring glomeruli (Kuebler et al., 2011), however, our model does not include spatial representation. LNs could contact other LNs with a synaptic weight of −8.0 and probability of 0.25 (red lines within the dashed red circle of **Figure 1A**). In this way, both the PNs and the LNs had multiglomerular connectivity. LNs could contact PNs with a synaptic weight of −1.8 and a probability of 0.25, irrespectively of the glomerulus to which each PN belonged (red lines going beyond the dashed red circle in **Figure 1A**). PNs could feedback to LNs with a synaptic weight of 1.4 and probability of 0.15, as shown by the green arrows entering the dashed red circle in **Figure 1A**. This relatively sparse bidirectional connectivity between PNs and LNs ensured that not all PNs were inhibited during odor presentation, avoiding an exaggerated activation of the LN population at the same time (Chong et al., 2012). Synaptic weights of PN to PN and LN to LN connections were selected to reproduce the proportion of neurons responding with excitation/inhibition observed in the data (see below).

The values of synaptic weights and connection probabilities that we used in the model are biologically plausible. We selected them because they produced very sparse responses (involving less than 30% of the neuron population) with a proportion excitation/inhibition around 1.8:1, as observed in the physiological recordings (Kuebler et al., 2011). This ratio was particularly sensitive to the mean synaptic weight of lateral excitation and lateral inhibition. For uniglomerular PN to PN connection weight values of 0–0.3, we obtained ratios of around 2.5:1.0, while for larger weights the ratios decreased in a monotonic manner, reaching 1.0:1.0 for a weight of 0.6. In order to match the proportion observed in the recorded data we used a weight of 0.37, as indicated above. For multi-glomerular PN to PN connections, the proportion also decreased with an increase in weight, varying from 2.4:1.0 to 1.26:1.0 for weights of 1.0–1.5, so we chose the intermediate weight of 1.25 that matched the recordings. In the case of the LN to LN connections the proportion excitation/inhibition showed a U-shaped profile for a weight range from −4.0 (4.0:1.0) to −10.0 (2.2:1.0) with a minimum in −6.0 (1.5:1), and so we selected a weight of −8.0 that matched the ratio observed in the data (1.8:1.0). We did not optimize the parameters to match the proportions of blend interactions being the main focus of our study, which were indeed very robust to changes in the lateral excitation and to increases in the lateral inhibition. Some parameters were selected following a previous study (Chong et al., 2012), such as the probability of LN to LN contacts and uniglomerular PN to PN contacts, as well as the use of low levels of bidirectional coupling between PNs and LNs. Note that reliable estimates for these parameters are not available in the moth. Furthermore, the high dimensionality of our model prevents an exhaustive parameter search. Hence, even if our parameters are within a physiological range, we cannot rule out the existence of another physiologically plausible parameter set that also results in the 1.8:1 ratio between excited and inhibited responses.

### *Odor stimulus in the model*

In line with the blends used in the physiological experiments, we considered odor stimuli to exist within a five-dimensional space ($Q = 5$), where each coordinate represents the concentration, $c_h$, of a single chemical component, $h$. The network was stimulated independently with the single component odors, the homogeneous blend and the single component odors at blend concentration. Single component odorants had zero concentration for each odor dimension but one, such that the five separate stimulus vectors ($q = 1, \ldots, Q$)

$$\overrightarrow{c_q} = [c_{q1}, \ldots, c_{qh}, \ldots, c_{qQ}],$$

contain the components $c_{qh} = 0$ for $h \neq j$ and $c_{hq} = 1$ for $h = q$. Thus, all component concentrations were normalised to one and dimensionless for simplicity. The homogeneous blend stimulus was defined as all components combined simultaneously, $c_h = 1 \,\forall\, h$, and the single component odors at blend concentrations were derived from the single component odors $\overrightarrow{c_{q(\text{blend})}} = 5\overrightarrow{c_q}$. Thus, in total there are eleven concentration vectors, five single component odors, $\overrightarrow{c_q}$, the homogeneous blend concentration, $\overrightarrow{c_{\text{blend}}}$, and the single component odors at blend concentration

$\overrightarrow{c_{q(\text{blend})}}$. The range of input concentrations used in the simulations (0–5) was selected to match the range used in the experiments.

OSN activation in response to stimulus presentation was calculated as follows. First, each OSN type odor dimension pair was assigned a binding value, $a$ (analogous to affinity to quantify the strength of binding), drawn from a Gaussian distribution with mean 0.5 and standard deviation 0.1. These values characterise the binding strength of the different pure chemicals for each of the molecular receptor types. Then, for a given OSN type, the different input concentration vectors, $\overrightarrow{c}$, were multiplied component by component with the binding values $\overrightarrow{a} = [a_1,\ a_2, \ldots,\ a_5]$ to obtain the binding vector $\overrightarrow{z} = [c_1 a_1,\ c_2 a_2, \ldots,\ c_5 a_5]$. This scheme provided a plausible description of the typical binding properties found in insect olfaction systems (Hallem and Carlson, 2006), since it captures the common observation that generalist molecular receptors have variable affinity for many chemicals, and cases of very high or very low affinity are relatively rare among general odors.

For a given odor presented to the model, the eight binding vectors corresponding to each OSN type were merged into a matrix $z_{dq}$ of 40 numbers (five columns and eight rows), each specifying the binding of a given compound $q$ (columns) to each of the OSN types $d$ (rows). Each binding value $z_{dq}$ was then passed through a sigmoid function that represented the dose-response curve of OSN activity to a given component

$$r_{dq} = \frac{\lambda}{1 + e^{-\alpha(z_{dq}-\gamma)}} + \eta$$

to obtain a matrix $r_{dq}$ which specifies the activities of each OSN type due to each component. The parameters $\alpha$, $\gamma$, $\eta$, and $\lambda$ control the slope, horizontal shift, vertical shift, and amplitude of the sigmoid, respectively. For each element of the match in order to create a diversity of tunings, parameter values were drawn from uniform distributions in the range [0,5], [0,4], [0,0.1], and [0,1], respectively. In this way, we obtained 40 different sigmoid functions (corresponding to each element of the matrix) that were used to calculate the output activity of each receptor type $d$ due to the binding of each chemical $q$. Receptor activations for each OSN type $d$ were obtained by summing the columns of the matrix $r_{dq}$. The sigmoid functions were different for different odorants across the receptor types (Hallem and Carlson, 2006).

Since we did not want to generate non-linearities in the OSN response to blends at the periphery level, we assumed a linear summation in OSN activities of the blend components. Thus, the columns of this matrix were summed linearly $r_d = \sum_q r_{dq}$ to obtain an eight-dimensional vector with the total activity of each receptor type which was the actual input from the OSNs to the PNs and LNs of the model (see Equation 1). It has been reported by Rospars et al. (2008), that certain type of competitive scheme may occur in around half of the receptors, while others show more complex allosteric interactions. However, since many details of the periphery function are still unknown in the moth, we did not want to add further hypothetical non-linear behaviors at the receptor level of our model, because they would obscure our assessment of the interaction types at the neuronal and network levels. In addition, this generalization makes the model more generally applicable for other non-moth systems.

When a stimulus was present, we added a small positive offset to OSN activations. This offset (set to 1.0) represents the recruitment of non-specific OSNs which activate at very low concentration and was assumed to be equal for each glomerulus for simplicity. For no binding at the input, the values of $d$ were small positive numbers, simulating some degree of spontaneous discharge in the OSNs (Hallem et al., 2004). Notice that we are modeling the receptor activity at a population level and the magnitudes are dimensionless. The parameter ranges were adjusted qualitatively to obtain a family of sigmoid functions that produced similar dose-response curves in terms of dynamic range (up to 3 log units), sensitivity, and response intensity axes to those found experimentally using optical recordings (Carlsson and Hansson, 2003). This scheme resulted in very little blend interactions at the OSN level (see "High correlation in blend interaction types between physiological data and computational model"), which is in agreement with recent observations performed using optical recordings (Kuebler et al., 2012).

#### PROCEDURE TO COMPUTE THE BLEND INTERACTIONS

The procedure used to determine the proportions of blend interactions in the response of single neurons was the same for the model simulations and the AL intracellular recordings, using only the neurons that responded to the stimulus. The stimulation was performed with the single components, the homogeneous blend, and the single components at blend concentration, using a stimulus pulse that lasted for 500 ms. Responsive neurons were then classified according to the relationship between the blend response and the responses to single components. Briefly, the maximum and the standard deviation of the responses to single components ($\max_S, \sigma_S$) and to single components at blend concentration ($\max_{SB}, \sigma_{SB}$) were computed. Then, classification was performed as follows: (1) suppression: blend response $< \max_S - \sigma_S$, (2) hypoadditivity: $\max_S - \sigma_S <$ blend response $< \max_S + \sigma_S$, (3) linear addition: $\max_S + \sigma_S <$ blend response $< \max(\max_S + \sigma_S, \max_{SB} + \sigma_{SB})$, and (d) synergy: blend response $> \max(\max_S + \sigma_S, \max_{SB} + \sigma_{SB})$.

The index of cell activity used to quantify the response in the recordings was the mean firing rate. In the case of the model we used the mean of the activity variable (see "Neuronal model") which ranges from 0 to 1. In both cases, we compared the activity evoked by the stimulus with the activity of a control period before the stimulus onset. The response was taken as the difference between the activities in these two time windows. In the AL of the moth, some neurons exhibited biphasic responses, which consist of excitation followed by inhibition. Our model does not account for this response type, and we thus pooled neurons that responded with excitation with neurons that showed biphasic responses, since the latter also consist of a net increase in firing rate. Hence, we concentrated here on the mean values of the neuronal activity leaving the assessment of the dynamic patterns to be presented in a future study.

As explained above, we followed parallel procedures to calculate the proportions of blend interactions in the recordings and

the simulations. In both cases, we assessed mean response intensity only, and not response duration. This is important because in the physiological data the response outlasted the stimulus, while in the model neurons are endowed with no intrinsic properties and thus the response ended with the stimulus offset. In order to account for the entire response period, the response of the model was considered to be the difference between the mean activity value in the 500 ms following and preceding the stimulus, while in the intracellular recordings the odorant response was assessed for 1400 ms following and preceding the stimulus onset. An assessment of the model with a stimulus lasting 1400 ms gave the same results as using 500 ms. In the model, a neuron was considered to be responsive when the difference in mean activity between the stimulus (with the blend or a single component at low concentration) and the control period exceeded a value of 0.1, which corresponds to 10% of the maximum activity value. This gives a response threshold that is close to one observed in the physiological data (Kuebler et al., 2011).

## RESULTS

### HIGH CORRELATION IN BLEND INTERACTION TYPES BETWEEN PHYSIOLOGICAL DATA AND COMPUTATIONAL MODEL

We performed 100 realizations of the computational model (network connectivity shown in **Figure 1**), each with different receptor binding matrices and sigmoidal functions for the model OSNs. **Figure 2** displays raster plots of an example realization showing the activity of all cells during the stimulus with the homogeneous blend (panel A) and with a single odorant at the blend concentration (panel B).

The biological and computational comparisons of blend interactions were performed by selecting a set of synaptic weights and connection probabilities that allowed a biologically reflective sparsity in the AL neuronal response including an approximate ratio of 1.8:1.0 between neurons that responded with excitation and inhibition, as observed in the recordings (Kuebler et al., 2011). In both cases, excitation was more prevalent in LNs, while PNs exhibited similar levels of excitatory or inhibitory responses. For PNs, the proportion excitation/inhibition was 0.86:1.0 in the model and 1.3:1.0 in the recordings where 12 cells responded with excitation and nine with inhibition. For LNs, this proportion was 3.0:1.0 in the model and also 3.0:1.0 in the recordings where six LNs responded with excitation and two with inhibition.

Responses were classified into four types according to the activity of each neuron in response to the blend vs. its single components. When there is no interaction between the components, the response evoked by the blend is equal to the linear sum of the responses to the individual components. In the case of synergism, the response exceeds the linear sum. Suppression is a reduced response with respect to the single components, while in the case of hypoadditivity (often referred to as overshadowing or blocking) at least one of the components of the blend is ignored and the response resembles that of the most effective component.

The proportions of blend interaction types are shown in **Figure 3** for neurons that respond with excitation (**Figure 3A**) and inhibition (**Figure 3B**). The blue columns represent the model results, while the red squares represent the values found in the experimental recordings of AL neurons. For both the recordings and the simulations, we found that most interactions between odorants were non-linear, and within the non-linear interactions hypoadditivity (blend response = single components) and suppression (blend response < single components) were more common than synergism (blend response > single components at blend concentrations). For the responses consisting of excitation (**Figure 3A**), the red squares are within the error bars of the blue columns, close to its mean value. This indicates a good agreement between the physiological data and the model. This is also the case for synergism and linear addition in the

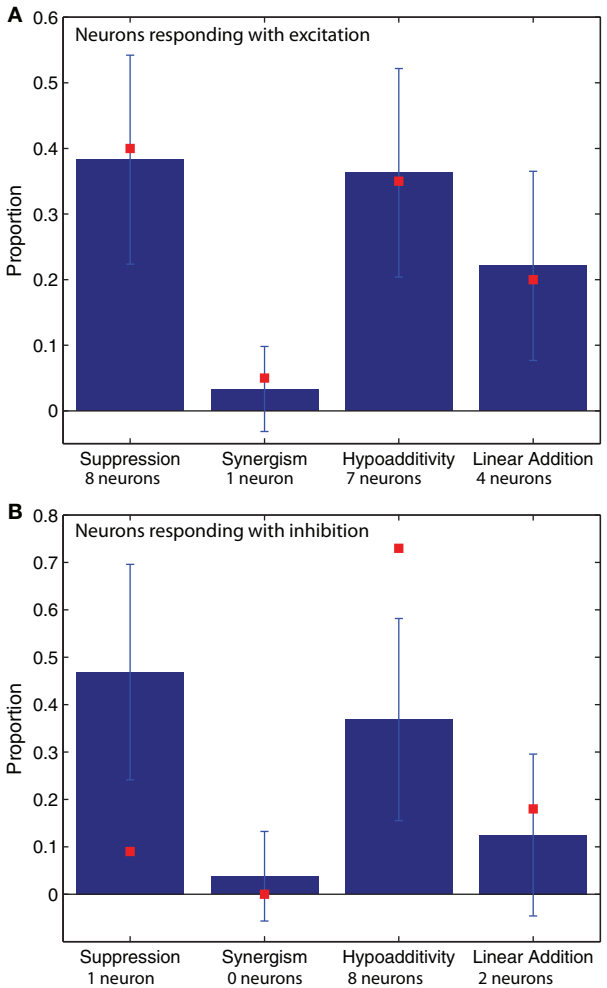


**FIGURE 3 | The proportions of blend interaction types found in 100 model realizations ($\mu \pm$ SD) are shown with blue bars.** The data values obtained from the experimental recordings ($N = 31$ neurons) are plotted with red squares. **(A)** Neurons that respond with excitation ($N = 20$). **(B)** Neurons that respond with inhibition ($N = 11$). The number of neurons used to compute the proportions represented by the red squares are provided under their corresponding abscissa labels. For the model simulations of neurons that respond with excitation (blue bars in **A**) the neuron numbers were 901 for suppression, 822 for synergy, 546 for hypoadditivity, and 81 for linear addition. For the neurons that respond with inhibition (blue bars in **B**) the neuron numbers were 622 for suppression, 520 for synergy, 179 for hypoadditivity, and 54 for linear addition.

neurons that respond with inhibition (**Figure 3B**). However, in this case the model does not fit the experimental results for suppression and hypoadditivity but exhibits more of the former and less of the latter type of blend interaction than the physiology (**Figure 3B**). These two categories are both forms of suppression, and the sum of their relative observations (about 0.8) is equal between the recordings and the model (**Figure 3B**). We suspect that intrinsic neuronal properties that were not included in the model are responsible for this discrepancy, altering the response of the neurons in the vicinity of the threshold between both interaction types.

The results shown in **Figure 3** did not change when we increased or decreased the weight of the lateral excitation or when we increased the weight of the lateral inhibition in the ranges specified in section "Network connectivity of the model". For weaker lateral inhibition values, we observed an increase in linear addition accompanied with a decrease of the same magnitude ($\sim$0.1) in suppression in the neurons that respond with excitation. Conversely, the proportion excitation/inhibition was very sensitive to variations in the values of these parameters (see "Network connectivity of the model").

To assess whether the observed proportions of blend interaction types arose from the AL network (PNs and LNs) or from the OSN periphery of the model, we ran a separate simulation using a reduced version of the model. In this simulation, we suppressed all inhibitory and excitatory connections within the AL and the input/output function of PNs and LNs was linear [$S(x) = x$], so the output of an AL neuron was simply a linear function of the input received from the OSN periphery. Under these conditions, we observed that all responses consisted in excitation, resulting in linear addition for most AL neurons (for every LN and for ¾ of PNs), while the remaining cases showed hypoadditivity. This is in close agreement with experimental observations found with optical recordings of the compound input (Kuebler et al., 2012) and suggests that the periphery has little influence on AL blend interactions in the moth. The same result was found when we suppressed only the lateral inhibition (LN to LN and LN to PN connections) using $S(x) = x/10$ to avoid an explosion of excitation in the simulation. This means that the result depicted in the blue bars of **Figure 3** arises principally from the AL network with a fundamental contribution made by the lateral inhibition. We also performed a control simulation with the full AL connectivity but using the linear input/output function $S(x) = x$ (with negative values rectified to 0) and observed that the results of **Figure 3** and the ratio excitation/inhibition were not significantly modified, implying that they are not due to the particular form of the non-linear squashing function used for AL neurons (see "Neuronal model").

As explained in "Neuronal recordings and odor stimulation," most of the recorded neurons (29 out of 31) could be classified as PNs or LNs (Kuebler et al., 2011). Using this classification, we compared the proportions of blend interaction types for PNs and LNs of different response types (**Figure 4**). Neurons that responded with excitation are depicted in panels A (PNs) and B (LNs), while neurons that responded with inhibition are depicted in panel C (PNs) and D (LNs). Despite the low cell numbers for the physiological measurements, we found that the model follows the trends observed in the recoded data for both PNs and LNs that responded with excitation (**Figures 4A,B**). In the case of PNs that respond with inhibition (**Figure 4C**) the model matched the proportions of the data only for synergism and linear addition. Comparing **Figures 3** and **4** we can conclude that the differences found in the pooled data set (**Figure 3**) are still apparent when assessing PNs and LNs separately (**Figure 4**).

In this work, as in previous experimental studies (Duchamp-Viret et al., 2003; Silbering and Galizia, 2007; Kuebler et al., 2011), blend interaction types (with the exception of synergy) were defined with respect to single component odors delivered at a concentration equal to the blend concentration divided by the number of single components tested (e.g., we used five components with blend concentration of five, resulting in a single concentration of 1). We also confirmed that the results presented in **Figure 3** are similar for blends of 2–7 components, or for blend concentrations from 1.25 to 10. These alterations did, however, affect the proportion or excitation/inhibition, which could be compensated by altering the levels of lateral inhibition. Thus, although our model results in monotonous responses to changes in input concentration, more experimental data is necessary to evaluate the generalization of our simulations over a wide range of input concentrations.

In this subsection, we have shown that our computational model, with a parameter set calibrated in order to reproduce the proportion of excitation/inhibition and response sparsity found in the physiological recordings, can also reproduce the proportions of blend interactions types without any additional tuning. While the model matches the data remarkably well for neurons that respond with excitation, hypoadditivity was underestimated and suppression was overestimated in neurons that responded with inhibition, although the sum of their relative observations was matched. Under these conditions of biologically plausible synaptic interactions, we assess in the following how blend coding is shaped by the different sources of synaptic input received by individual AL neurons.

### LN INPUT SHAPES BLEND INTERACTIONS AND RESPONSE TYPES IN AL

Our goal was to understand how the different types of responses and blend interactions emerged in the AL network. Hence, we analyzed the synaptic inputs to AL neurons and their changes as the stimulus was varied. In **Figure 5A** we plot the difference in total synaptic input between the blend stimulation period and the pre-stimulation period, multiplied by the corresponding synaptic weights for different response categories in the model. This magnitude is referred to as synaptic input. As expected, neurons that responded with excitation experienced an increase in net input with blend stimulation, while neurons that responded with inhibition showed a decrease in their net input (**Figure 5A**).

**Figures 5B** and **C** display the synaptic input arriving from the LNs (left panels), PNs (middle panels), and OSNs (right panels) to the PNs (**Figure 5B**), and LNs (**Figure 5C**). For both cell types, changes in lateral inhibition were the main determinants of response type. In the case of PNs, however, other PNs and OSNs also contributed to the response. In the case of LNs (**Figure 5C**) the only relevant input arrived from other LNs, with

no significant contribution carried by the input arriving from PNs and OSNs (middle and right panels in **Figure 5C**).

As interaction types are defined by the relation between the blend response and the responses to the single components, we performed a similar analysis on the synaptic inputs to each neuron considering the difference between the input during blend stimulation and the mean input during single component presentations. This magnitude, referred as change in synaptic input,

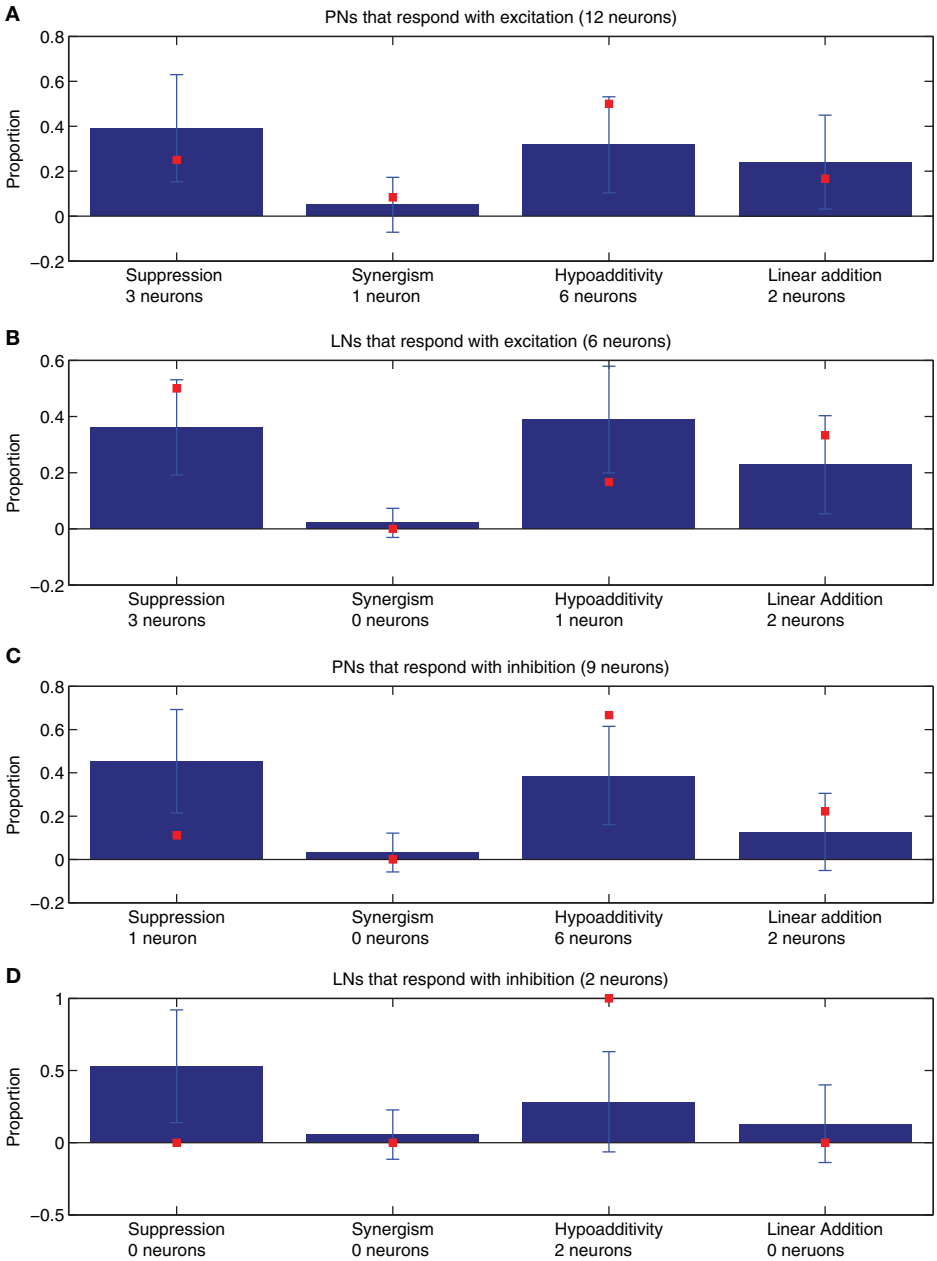


**FIGURE 4 | The proportions of blend interaction types found in 100 model realizations ($\mu \pm$ SD, blue bars) are compared with the data values obtained from the experimental recordings of the neurons that could be successfully classified as PNs or LNs ($N = 29$ neurons, red squares). (A)** PNs that respond with excitation ($N = 12$). **(B)** LNs that respond with excitation ($N = 6$). **(C)** PNs that respond with inhibition ($N = 9$). **(D)** LNs that respond with inhibition ($N = 2$). The number of neurons used to compute the proportions represented by the red squares are provided under their corresponding abscissa labels. For the model simulations of PNs that respond with excitation (blue bars in A) the neuron numbers were 397 for suppression, 306 for synergy, 240 for hypoadditivity, and 47 for linear addition. For the LNs that respond with excitation (blue bars in B) the neuron numbers were 504 for suppression, 516 for synergy, 306 for hypoadditivity, and 34 for linear addition. For the PNs that respond with inhibition (blue bars in C) the neuron numbers were 506 for suppression, 457 for synergy, 151 for hypoadditivity, and 42 for linear addition. For the LNs that respond with inhibition (blue bars in D) the neuron numbers were 116 for suppression, 63 for synergy, 28 for hypoadditivity, and 12 for linear addition.

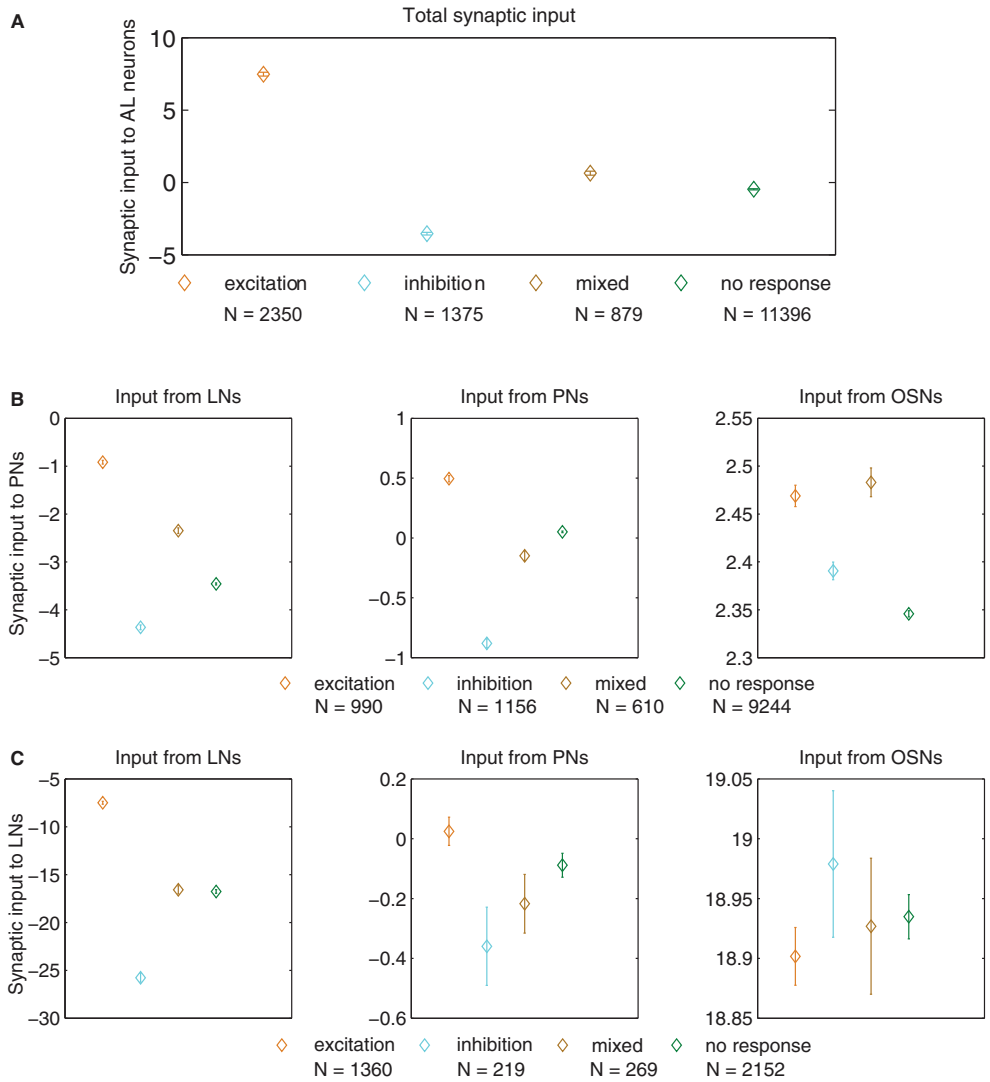


**FIGURE 5 | Synaptic input (defined as the difference in input between the blend stimulation period and the pre-stimulation control period, multiplied by the corresponding synaptic weights) for neurons of different response type ($\mu \pm$ SEM for 100 model realizations). (A)** Total input to AL neurons. All comparisons reached $p < 1 \times 10^{-6}$ in the *t*-test after Bonferroni correction, the most important result being responses consisting of excitation vs. inhibition (orange and cyan diamonds). In panels **B** and **C**, we show the input arriving from different types of neurons (LNs, PNs, and OSNs) to AL neurons (PNs and LNs). **(B)** Input to PNs arriving from LNs (left panel), PNs (middle panel), and OSNs (right panel). **(C)** Input to LNs arriving from LNs (left panel), PNs (middle panel), and OSNs (right panel). The *p* values for cases in which we found significant differences in the *t*-test ($p \leq 0.01$, after Bonferroni correction) are listed in the following, the most important result being responses consisting of excitation vs. inhibition (orange and cyan diamonds). For the input from LNs to PNs (left panel of **B**) all comparisons reached $p < 1 \times 10^{-6}$. For the input from PNs to PNs (middle panel of **B**) comparisons reached $p < 1 \times 10^{-6}$. For the input from OSNs to PNs (right panel in **B**) excitation vs. inhibition $p < 1 \times 10^{-6}$, excitation vs. no response $p < 1 \times 10^{-6}$, inhibition vs. mixed response $p < 1 \times 10^{-6}$, inhibition vs. no response $p < 2 \times 10^{-5}$, and mixed vs. no response $p < 1 \times 10^{-6}$. For the input from LNs to LNs (left panel in C) all comparisons reached $p < 1 \times 10^{-6}$, with the only exception of mixed vs. no response that was not significant.

was calculated as the difference between the blend and the average single components at low concentration, multiplied by the corresponding synaptic weights (**Figures 6–8**). In **Figure 6** we depict the total change in synaptic input for neurons that respond with excitation (**Figure 6A**) and inhibition (**Figure 6B**), irrespective of their neuronal type (PNs or LNs). The following two figures unfold this result separating PNs from LNs and specifying the different sources of input. In **Figure 7** we show neurons that respond with excitation (PNs in **Figure 7A** and LNs in **Figure 7B**), while in **Figure 8** we show neurons that respond with inhibition (PNs in **Figure 8A** and LNs in **Figure 8B**).

**Figure 6** shows that the change in total input grew in the order: suppression, hypoadditivity, and linear addition in neurons that responded with excitation (**Figure 6A**), and it decreased following the same sequence in the case of neurons that responded with inhibition (**Figure 6B**).

**Figure 7** shows that the input change arriving from LNs to LNs that responded with excitation (left panel in **Figure 7B**) grew

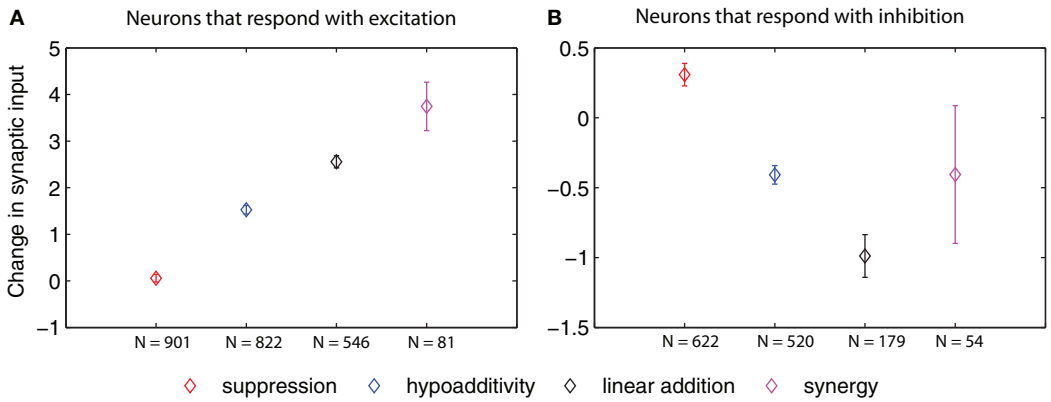


**FIGURE 6 | Change in synaptic input (defined as the difference in input between the blend response and the average response to the single components at low concentration, multiplied by the corresponding synaptic weights) for AL neurons of different blend interaction types ($\mu \pm$ SEM for 100 model realizations). (A)** Total change in synaptic input arriving to neurons that respond with excitation. **(B)** Total change in synaptic input arriving to neurons that respond with inhibition. The $p$ values for cases in which we found significant differences in the $t$-test ($p \leq 0.01$, after Bonferroni correction) are listed in the following. In panel **A**: suppression vs. hypoadditivity $p < 1 \times 10^{-6}$; suppression vs. linear addition $p < 1 \times 10^{-6}$; suppression vs. synergy $p < 1 \times 10^{-6}$; hypoadditivity vs. linear addition $p =< 1 \times 10^{-6}$, hypoadditivity vs. synergy $p < 1 \times 10^{-6}$. In panel **B**: suppression vs. hypoadditivity $p < 1 \times 10^{-6}$; suppression vs. linear addition $p < 1 \times 10^{-6}$; hypoadditivity vs. linear addition $p = 3.8 \times 10^{-4}$.

monotonically from suppression to synergy, creating the image of an ascending ladder. A similar picture applies for the input change arriving from the LNs to the PNs that responded with excitation (left panel in **Figure 7A**), although in this case linear addition and synergy (the last step of the ladder) were not significantly different. This suggests that a stronger lateral inhibition in response to the blend established suppression, while small changes and decreases in lateral inhibition resulted in hypoadditivity and linear addition (or synergy), respectively. The change in input arriving from PNs to PNs that responded with excitation (middle panel in **Figure 7A**) again created the trend of an ascending ladder with a missing last step. This is not the case for the change in input arriving from PNs to LNs that responded with excitation (middle panel in **Figure 7B**) where no significant differences were found. Regarding the input change from OSNs, a decrease for PNs that responded with excitation (right panel in **Figure 7A**) established suppression, but there were no significant differences in input changes from OSNs to LNs that responded with excitation for any interaction type (right panel in **Figure 7B**).

**Figure 8** shows that the change in input establishing suppression for responses consisting of inhibition likewise tended to differ from that establishing the other interactions types. For PNs that responded with inhibition (left panel in **Figure 8A**) the input change from LNs in establishing suppression was greater than both hypoadditivity or linear addition. This situation repeated for the input from OSNs to PNs that responded with inhibition (right panel in **Figure 8A**). For the input from PNs to PNs that responded with inhibition, the input change creating suppression was greater than in the other three categories (middle panel in **Figure 8A**). For the input from LNs to LNs that responded with inhibition the input change creating suppression was greater than linear addition (left panel in **Figure 8B**), but no significant differences were found in the input changes from PNs and OSNs to LNs (middle and right panels in **Figure 8B**). The increased change in synaptic input that created suppression for responses consisting of inhibition resulted from both a decreased inhibition coming from the LNs, and a stronger excitation coming from the OSNs and PNs.

In summary, **Figures 7** and **8** indicate that blend interactions were shaped mainly by the input changes coming from LNs in all AL cells of the model, with an agonistic contribution of smaller magnitude from PNs and OSNs in the case of PNs.

## DISCUSSION

### COMPARISON OF BLEND INTERACTIONS IN THE MODEL AND RECORDINGS

The proportions of non-linear blend interaction types observed in the biological data were accurately predicted by the simulation results in most cases. The matching is almost perfect for neurons that respond with excitation. For neurons that respond with inhibition, a good agreement was found for synergism and linear addition, while in the case of suppression and hypoadditivity the model could only match the sum of both categories, but not the actual proportions of each. Both hypoadditivity and suppression are forms of suppressive interactions (Kuebler et al., 2011), hence this discrepancy is quantitative rather than qualitative. Future research can elucidate whether more realistic single-cell properties, or the presence of inhibitory responses at the OSN level (e.g., Hallem and Carlson, 2006) could result in a better match. Indeed, the high correlation between the model and the physiological data is surprising considering the simplicity of the model employed, and must therefore originate in the morphologically based pattern of neuronal population interactions. As stated in section "High correlation in blend interaction types between physiological data and computational model", the neuronal activation function $S(x)$ (Chong et al., 2012) is not responsible for the proportions of blend interactions observed in **Figure 3**, which are also found to hold over a wide dynamic range of stimulus. This type of non-linearity is widely used in the field of computational

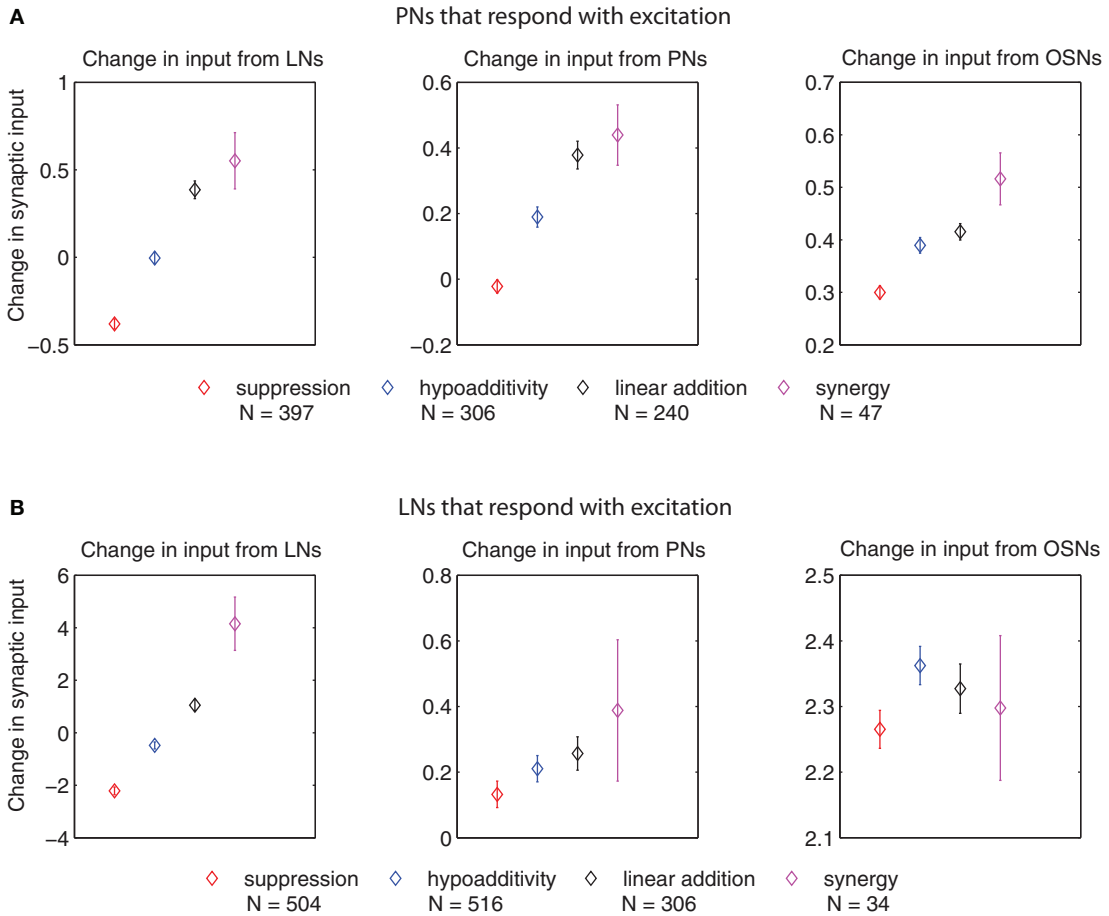


**FIGURE 7 | Change in synaptic input (defined as the difference in input between the blend response and the average response to the single components at low concentration, multiplied by the corresponding synaptic weights) for PNs and LNs that respond with excitation of different blend interaction types ($\mu \pm$ SEM for 100 model realizations).** **(A)** Change in input to PNs arriving from LNs (left panel), PNs (middle panel), and OSNs (right panel). **(B)** Change in input to LNs arriving from LNs (left panel), PNs (middle panel), and OSNs (right panel). The $p$ values for cases in which we found significant differences in the $t$-test ($p \leq 0.01$, after Bonferroni correction) are listed in the following. For the change in input arriving from LNs to PNs that respond with excitation (left panel in **A**): suppression vs. hypoadditivity $p < 1 \times 10^{-6}$; suppression vs. linear addition $p < 1 \times 10^{-6}$, suppression vs. synergy $p < 1 \times 10^{-6}$; hypoadditivity vs. linear addition $p < 1 \times 10^{-6}$; hypoadditivity vs. synergy $p = 1 \times 10^{-6}$. For the change in input arriving from PNs to PNs that respond with excitation (middle panel in **A**): suppression vs. hypoadditivity $p < 1 \times 10^{-6}$; suppression vs. linear addition $p < 1 \times 10^{-6}$; suppression vs. synergy $p < 1 \times 10^{-6}$; hypoadditivity vs. linear addition $p < 1.41 \times 10^{-3}$.For the change in input arriving from OSNs to PNs that respond with excitation (right panel in **A**) suppression vs. hypoadditivity $p = 2.8 \times 10^{-5}$; suppression vs. linear addition $p < 1 \times 10^{-6}$; suppression vs. synergy $p = 1 \times 10^{-6}$. For the change in input arriving from LNs to LNs that respond with excitation (left panel in **B**): suppression vs. hypoadditivity $p < 1 \times 10^{-6}$; suppression vs. linear addition $p < 1 \times 10^{-6}$; suppression vs. synergy $p < 1 \times 10^{-6}$; hypoadditivity vs. linear addition $p =< 1 \times 10^{-6}$, hypoadditivity vs. synergy $p < 1 \times 10^{-6}$, linear addition vs. synergy $p = 7.9 \times 10^{-5}$.

neuroscience and is in agreement with most observations of the activation profile in real neurons.

Our computational model of the AL comprises many levels of biological organization, from the OSN periphery to the network architecture, including the neuronal model and synaptic interactions. We used probabilistic connectivity to create random networks that operate in a balanced regime, with strong excitation and strong inhibition that approximately compensate each other, which is a reasonable strategy considering that the details of the local synaptic efficacy that operates in the biological system are unknown. This allows to reproduce the proportion of the different interaction type even when some key parameters (such as the lateral excitation and lateral inhibition synaptic weights; see "Network connectivity of the model") are varied in a relatively broad range. Whenever possible, morphological and physiological data were used to constrain the model, but in some cases simplifying assumptions had to be made due to the lack of sufficient experimental evidence. In such cases we adopted decisions that were plausible or based on previous literature. For the periphery, a linear combination of ingredients was used because it is the simplest assumption and no information is available about this issue in the moth. The neuronal and synaptic models were taken from a previous modeling study (Chong et al., 2012), and the probabilistic rules used to set the network structure were

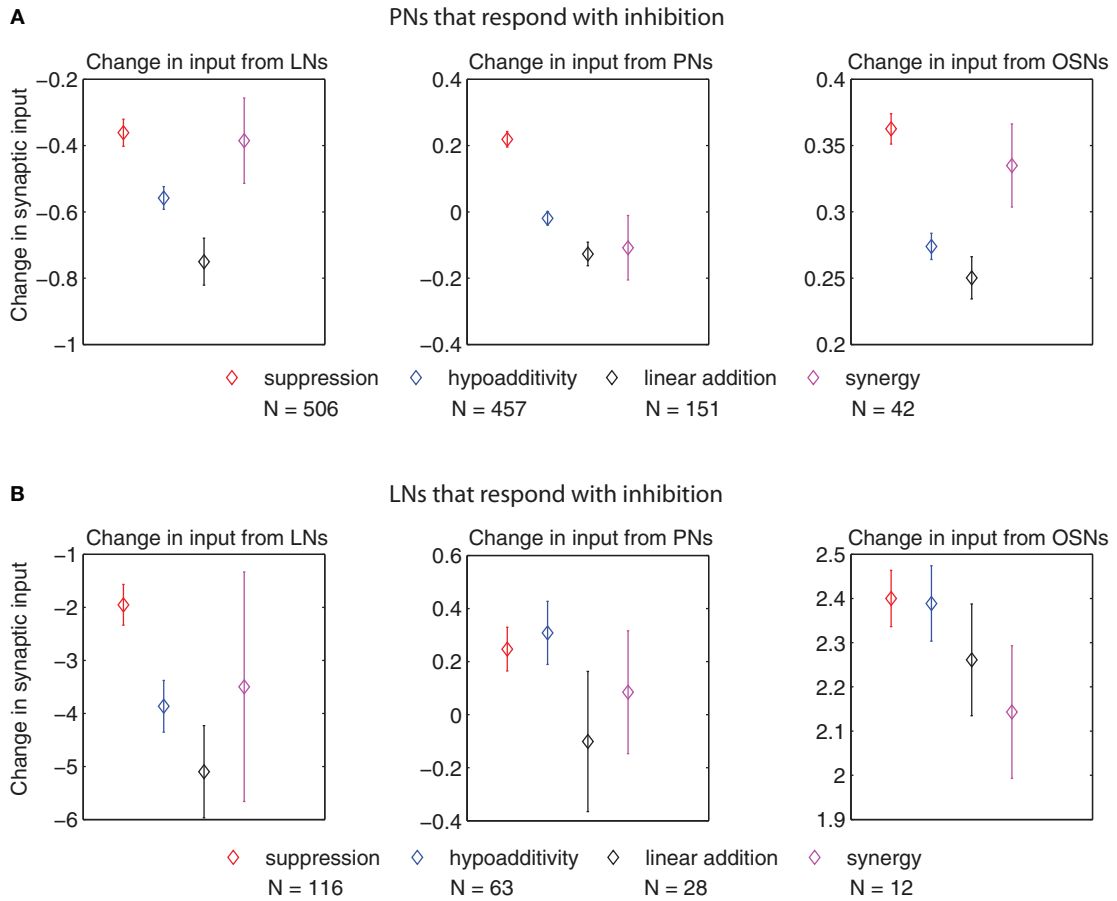


**FIGURE 8 | Change in synaptic input (defined as the difference in input between the blend response and the average response to the single components at low concentration, multiplied by the corresponding synaptic weights) for PNs and LNs that respond with inhibition of different blend interaction types (μ ± SEM for 100 model realizations).** **(A)** Change in input to PNs arriving from LNs (left panel), PNs (middle panel), and OSNs (right panel). **(B)** Change in input to LNs arriving from LNs (left panel), PNs (middle panel), and OSNs (right panel). The $p$ values for cases in which we found significant differences in the $t$-test ($p \leq 0.01$, after Bonferroni correction) are listed in the following. For the change in input arriving from LNs to PNs that respond with inhibition (left panel in **A**): suppression vs. hypoadditivity $p = 1.64 \times 10^{-3}$; suppression vs. linear addition $p = 2.9 \times 10^{-5}$. For the change in input arriving from PNs to PNs that respond with inhibition (middle panel in **A**): suppression vs. hypoadditivity $p < 1 \times 10^{-6}$; suppression vs. linear addition $p < 1 \times 10^{-6}$; suppression vs. synergy $p = 9.78 \times 10^{-4}$. For the change in input arriving from OSNs to PNs that respond with inhibition (right panel in **A**): suppression vs. hypoadditivity $p < 1 \times 10^{-6}$; suppression vs. linear addition $p = 6 \times 10^{-6}$. For the change in input arriving from LNs to LNs that respond with inhibition (left panel in **B**): suppression vs. linear addition $p = 3.3 \times 10^{-3}$.

based on morphological studies (Kuebler et al., 2011, and references therein). The parameters are biologically plausible and allow us to reproduce the excitation/inhibition ratio and response sparsity observed in the recordings. Our results are based on the average behavior of 100 networks generated with probabilistic connectivity rules, hence the possibility that they rely on a specific value for one or more of the non-ranged, fixed parameters is extremely unlikely. The general agreement between the proportions of blend interactions in the simulations and the recordings was not calibrated into the model but arises as a purely emergent phenomenon. This predictive power strongly indicates that the model describes the mean responses of AL neurons to both pure chemicals and odor blends in a physiologically relevant manner, capturing the working principles of the AL network to a considerable extent.

In the following, we discuss the role of synaptic input within the network in determining the type of response and blend interaction displayed by individual neurons of the model. Our analysis is restricted to the mean values of neural activity during the odor stimulus and control period, leaving the influence of the dynamic patterns to be presented in a separate study.

## SYNAPTIC INPUT, RESPONSE TYPES, AND BLEND INTERACTIONS IN THE COMPUTATIONAL MODEL

Neurons that respond with excitation undergo an increase in net synaptic input in response to blend stimulation, while neurons that respond with inhibition experience a decrease in their input, as expected (**Figure 5A**). Individual neurons are implemented as leaky integrators, hence they can only increase (decrease) their activation if their input increases (decreases). A more

surprising result is that the difference in total input depicted in **Figure 5A** is determined mainly by the input arriving from the LNs (**Figures 5B,C**). The LNs that respond with inhibition do so because they received a very strong inhibition from other LNs, and not less excitation from the PNs and OSNs. The LNs that respond with excitation do so because they received weaker inhibition from the LNs and not larger excitation from the PNs and OSNs (**Figure 5C**). In the case of the PNs, the response consisting of inhibition was built up by a very strong inhibition from LNs combined with a weaker excitation from PNs and OSNs, while for the response consisting of excitation a weaker inhibition from LNs was combined with a stronger excitation from PNs and OSNs (**Figure 5B**). To summarize this first finding, we can state that the response type of all neurons depends on the change in LN input in response to olfactory stimulation, with an agonistic contribution of smaller magnitude coming from the PN and OSN input in the case of PNs.

The second finding in our assessment of the pre-synaptic activity (**Figures 6**, **7**, and **8**), is that the change in synaptic input from the LNs is key to determining the type of blend interaction shown by a neuron (PN or LN). In the particular case of LNs that respond with excitation, the change in input from other LNs is the only determinant of the blend interaction type, with suppression receiving the largest amount of inhibition (i.e., lower input value) followed by hypoadditivity, linear addition, and synergy in a sequence of decreasing inhibition. A similar situation holds for PNs that respond with excitation, where this sequence starts in suppression, continues with hypoadditivity, and ends with linear addition (without including synergy). However, the change in input arriving from other PNs also contributes to determine the blend interaction type through an excitation drive that progressively grows in the sequence suppression, hypoadditivity, linear addition, and synergy. In addition, the change in input from OSNs to PNs is smaller in suppression than in the other categories, creating an additional influence that adds agonistically with the input from the LNs and PNs. In the case of neurons that respond with inhibition we can also recognize a key role of the LNs, although in this case it is mainly to determine the difference between suppression and other categories, without the sequence mentioned above. Again, for LNs that respond with inhibition the only significant influence is the one coming from other LNs, while for PNs that respond with inhibition the change in input arriving from PNs and OSNs combines in an agonistic manner with the change in LN input to determine whether the interaction type will be suppression or not. From the three agonistic influences observed in PNs that respond with excitation and inhibition, the one coming from the LNs is stronger as it can be seen in the scales of ordinates in the **Figures 7** and **8**.

As a summary of our synaptic analysis, we can state that the input changes coming from LNs, PNs, and OSNs drive the membrane potential of the PN output from the AL in an agonistic manner that determines the type of blend interaction that they display. In the case of the LNs, the only significant input is the one arriving from other LNs. Suppressive interactions in neurons that respond with excitation are associated with smaller changes in synaptic input than the other types of blend interaction, while the opposite holds for neurons that respond with inhibition.

The observed proportions of blend interactions types were robust to changes in lateral excitation, but were affected by decreases in the weight of lateral inhibition. The fact that less LN to LN coupling decreased the proportion of suppression (increasing linear addition by a similar amount; see "High correlation in blend interaction types between physiological data and computational model") in neurons that respond with excitation makes sense on the light of the analysis presented in **Figure 7B** (left panel), as suppressive interactions are associated with negative values of synaptic input change from LNs. Thus, lateral inhibition appears to be playing a more important role than the lateral excitation (mediated by the PN to PN connectivity) in the shaping of blend interactions types. This agrees with the results of the honey bee modeling studies of Linster and Smith (1997) for suppression and hypoadditivity (referred in Linster's study as blocking and overshadowing, respectively) and Schmuker et al. (2011) who showed that strong lateral inhibition can result in suppressive mixture coding, allowing good odor discrimination in the PNs of the lateral antenno-cerebral tract. Our results suggest that lateral inhibition is also very important for the emergence of linear addition and synergism in the case of the neurons that respond with excitation (left panels in **Figures 7A,B**), since these interaction types are associated with a larger input change arriving from LNs. Behavioral studies have shown that $GABA_A$ antagonists disrupt odor discrimination (Mwilaria et al., 2008) and the bursting response pattern of PNs associated with odor source location (Lei et al., 2009) in *M. sexta*. This indicates that pharmacological or genetic manipulation of the interneuron network of the moth would result in a severe reduction in non-linear interactions to blends, as has been observed for mixture suppression in the PNs of *Drosophila* after picrotoxin application (Silbering and Galizia, 2007). This type of experiments, combined with simultaneous multi-unit and optical recordings that assess a greater proportion of the AL network, would be key to elucidating the nature of AL blend processing mechanisms in the future.

### RELATION WITH PREVIOUS EXPERIMENTAL AND MODELING STUDIES

The results of this computational study provide important global insights into the biological network that are difficult to uncover empirically through current physiological methods. Comparative analyses across several species suggest that odor blends are coded at the first processing stage in a spatiotemporal fashion (for review see Lei and Vickers, 2008) defined by a stereotyped spatial pattern (Galizia and Roessler, 2010), different response onsets (Krofczik et al., 2008), and synchronous ensemble firing patterns (Riffell et al., 2009a,b). However, the close agreement between our neuromorphic model and the electrophysiological data suggests that the connectivity pattern of input OSNs, interglomerular LNs, and output PNs is itself sufficient to confer the level of blend interactions exhibited by the AL. This implies that other cellular characteristics relating to the firing and spatiotemporal dynamics of AL neurons are not obligatory to establish the non-linearity of blend processing witnessed in other electro- and optophysiological analyses of insects (Carlsson et al., 2005; Deisig et al., 2006; Pinero et al., 2008; Silbering et al., 2008; Riffell et al., 2009a). This result is particularly surprising considering the highly reduced assumptions made in our model that

do not consider cellular and network properties such as excitatory interneuron synapses (Shang et al., 2007), heterogeneity of interneuron branching (Fonta et al., 1993), and additional electric coupling between glomeruli (Yaksi and Wilson, 2010).

Further examination of the synaptic interactions in the model reveals that the source of the non-linear processing is due in large part to the interneurons within the network. Such a result is reasonable when one considers the broadly tuned nature of the input to the AL. A blend response results from the activity of several OSNs with different affinities and responses to odor components (Hallem et al., 2004; Hallem and Carlson, 2006). As receptor neurons expressing the same receptor innervate the same glomerulus in the AL (Ressler et al., 1994; Mombaerts, 1996; Vosshall, 2000), some form of interglomerular connectivity is imperative for accurate blend representation, and any apparent non-linearity is subsequently the result of such interconnectivity. Indeed, recent physiological studies in flies (Silbering et al., 2008) and bees (Deisig et al., 2006) have highlighted the vital role of the interneuron network in conferring blend non-linearity. Moreover, the importance of inhibitory sub-networks in shaping the activity of excitatory neurons and synchronous firing is widely recognized in the field of sensory perception [e.g., see Assisi et al., 2011; but note the recent study of Daly et al. (2011) in *M. sexta*], and our study suggests it is also vital for neural encoding of complex odor blends.

Interestingly, the output of the network, relayed by PNs, is ultimately influenced by synaptic input from all three types of AL neurons. This indicates that the final representation of a blend is a composite of all possible interactions within the AL. This also indicates that any blend non-linearities already present at the periphery (not included here but implied by other studies: Carlsson and Hansson, 2002; Hillier and Vickers, 2011; Su et al., 2011) may significantly impact the resultant output from the AL. Additional modulation between PNs (either within or between glomeruli) further modifies the output and creates the ultimate "blend percept" (Kuebler et al., 2011).

Our results suggest that the non-linear processing establishing the unique "blend percept" within the AL can result from network interactions, without the need of intrinsic neuronal properties in the cells within that network. Our findings highlight that such mixture interactions are a natural outcome of the architecture of the AL, and reveal its important role in shaping the perception of olfactory information in the CNS. By design, the AL is not merely a relay station for olfactory information, but filters and processes multicomponent information into a unique representation that reduces signal dimensionality for subsequent processing in the CNS.

## ACKNOWLEDGMENTS

This research was supported by EU 6th Framework Programme FET Project iCHEM and the Max Planck Society. The authors want to thank Dr. Manuel Montanes for his useful comments and suggestions.

## REFERENCES

Assisi, C., Stopfer, M., and Bazhenov, M. (2011). Using the structure of inhibitory networks to unravel mechanisms of spatiotemporal patterning. *Neuron* 69, 373–386.

Baker, T. C. (2008). Balanced olfactory antagonism as a concept for understanding evolutionary shifts in moth sex pheromone blends. *J. Chem. Ecol.* 34, 971–981.

Bruyne, M., and Baker, T. C. (2008). Odor detection in insects: volatile codes. *J. Chem. Ecol.* 34, 882–897.

Carlsson, M. A., Chong, K. Y., Daniels, W., Hansson, B. S., and Pearce, T. C. (2007). Component information is preserved in glomerular responses to binary odor mixtures in the moth *Spodoptera littoralis*. *Chem. Senses* 32, 433–443.

Carlsson, M. A., and Hansson, B. S. (2002). Responses in highly selective sensory neurons to blends of pheromone components in the moth *Agrotis segetum*. *J. Insect Physiol.* 48, 443–451.

Carlsson, M. A., and Hansson, B. S. (2003). Dose-response characteristics of glomerular activity in the moth antennal lobe. *Chem. Senses* 28, 269–278.

Carlsson, M. A., Knusel, P., Verschure, P. F. M. J., and Hansson, B. S. (2005). Spatio-temporal Ca2+ dynamics of moth olfactory projection neurones. *Eur. J. Neurosci.* 22, 647–657.

Chong, K. Y., Capurro, A., Karout, S., and Pearce, T. C. (2012). Stimulus and network dynamics can collide in a ratiometric model of the antennal lobe macroglomerular complex. *PLoS One* 7:e29602. doi: 10.1371/journal.pone.0029602

Christensen, T. A., Mustaparta, H., and Hildebrand, J. G. (1991). Chemical communication in heliothine moths. II. Central processing of intraspecific and interspecific olfactory messages in the male cOSN earworm moth, *Helicoverpazea*. *J. Comp. Physiol. A* 169, 259–274.

Daly, K. C., Galán, R. F., Peters, O. J., and Staudacher, E. M. (2011). Detailed characterization of local field potential oscillations and their relationship to spike timing in the antennal lobe of the moth *Manduca sexta*. *Front. Neuroeng.* 4:12. doi: 10.3389/fneng.2011.00012

Deisig, N., Giurfa, M., Lachnit, H., and Sandoz, J. C. (2006). Neural representation of olfactory mixtures in the honeybee antennal lobe. *Eur. J. Neurosci.* 24, 1161–1174.

Deisig, N., Giurfa, M., and Sandoz, J. C. (2010). Antennal lobe processing increases separability of odor mixture representations in the honeybee. *J. Neurophysiol.* 103, 2185–2194.

Duchamp-Viret, P., Duchamp, A., and Chaput, M. (2003). Single olfactory sensory neurons simultaneously integrate the components of an odour mixture. *Eur. J. Neurosci.* 18, 2690–2696.

Fernandez, P. C., Locatelli, F. F., Person-Rennell, N., Deleo, G., and Smith, B. H. (2009). Associative conditioning tunes transient dynamics of early olfactory processing. *J. Neurosci.* 29, 10191–10202.

Fonta, C., Sun, X., and Masson, C. (1993). Morphology and spatial distribution of bee antennal lobe interneurones responsive to odours. *Chem. Senses* 18, 101–119.

Galizia, C., and Menzel, R. (2001). The role of glomeruli in the neural representation of odours: results from optical recording studies. *J. Insect Physiol.* 47, 115–130.

Galizia, C. G., and Roessler, W. (2010). Parallel olfactory systems in insects: anatomy and function. *Annu. Rev. Entomol.* 55, 399–420.

Grosse-Wilde, E., Kuebler, L. S., Bucks, S., Vogelb, H., Wichera, D., and Hansson, B. S. (2011). Antennal transcriptome of *Manduca sexta*. *Proc. Natl. Acad. Sci. U.S.A.* 108, 7449–7454.

Hallem, E. A., and Carlson, J. R. (2006). Coding of odors by a receptor repertoire. *Cell* 125, 143–160.

Hallem, E. A., Ho, M. G., and Carlson, J. R. (2004). The molecular basis of odor coding in the *Drosophila antenna*. *Cell* 117, 965–979.

Hansson, B. S., and Anton, S. (2000). Function and morphology of the antennal lobe: new developments. *Annu. Rev. Entomol.* 45, 203–231.

Hillier, N. K., and Vickers, N. J. (2011). Mixture interactions in moth olfactory physiology: examining the effects of odorant mixture, concentration, distal stimulation, and antennal nerve transection on sensillar responses. *Chem. Senses* 36, 93–108.

Homberg, U., Christensen, T., and Hildebrand, J. (1989). Structure and function of the deutocerebrum in insects. *Annu. Rev. Entomol.* 34, 477–501.

Homberg, U., Montague, R. A., and Hildebrand, J. G. (1988). Anatomy of antenno-cerebral pathways in the brain of the sphinx moth *Manduca sexta*. *Cell Tissue Res.* 254, 255–281.

Huang, J., Zhang, W., Qiao, W., Hu, A., and Wang, Z. (2010).

Functional connectivity and selective odor responses of excitatory local interneurons in Drosophila antennal lobe. *Neuron* 67, 1021–1033.

Joerges, J., Küttner, A., Galizia, C., and Menzel, R. (1997). Representations of odours and odour mixtures visualized in the honeybee brain. *Nature* 387, 285–288.

Krofczik, S., Menzel, R., and Nawrot, M. P. (2008). Rapid odor processing in the honeybee antennal lobe network. *Front. Comput. Neurosci.* 2:9. doi: 10.3389/neuro.10.009.2008

Kuebler, L. S., Olsson, S. B., Weniger, R., and Hansson, B. S. (2011). Neuronal processing of complex mixtures establishes a unique odor representation in the moth antennal lobe. *Front. Neural Circuits* 5:7. doi: 10.3389/fncir.2011.00007

Kuebler, L. S., Schubert, M., Karpati, Z., Hansson, B. S., and Olsson, S. B. (2012). Antennal lobe processing correlates to moth olfactory behavior. *J. Neurosci.* 32, (in press).

Laing, D. G., Panhuber, H., and Slotnik, B. M. (1989). Odour masking in the rat. *Physiol. Behav.* 45, 689–694.

Lei, H., Riffel, J. A., Gage, S. L., and Hildebrand, J. G. (2009) Contrast enhancement of stimulus intermittency in a primary olfactory network and its behavioral significance. *J. Biol.* 8, 21.1–21.16.

Lei, H., and Vickers, N. (2008). Central processing of natural odor mixtures in insects. *J. Chem. Ecol.* 34, 915–927.

Linster, C., and Cleland, T. A. (2010). Decorrelation of odor representations via spike timing-dependent plasticity. *Front. Comput. Neurosci.* 4:157. doi: 10.3389/fncom.2010.00157

Linster, C., Sachse, S., and Galizia, C. G. (2005). Computational modeling suggests that response properties rather than spatial position determine connectivity between olfactory glomeruli. *J. Neurophysiol.* 93, 3410–3417.

Linster, C., and Smith, B. H. (1997). A computational model of the response of honey bee antennal lobe circuitry to odor mixtures: overshadowing, blocking and unblocking can arise from lateral inhibition. *Behav. Brain Res.* 87, 1–14.

Martin, J. P., Beyerlein, A., Dacks, A. M., Reisenman, C. E., Riffell, J. A., Lei, H., and Hildebrand, J. G. (2011). The neurobiology of insect olfaction: sensory processing in a comparative context. *Prog. Neurobiol.* 95, 427–447.

Matsumoto, S., and Hildebrand, J. (1981). Olfactory mechanisms in the moth *Manduca sexta*: response characteristics and morphology of central neurons in the antennal lobes. *Proc. R. Soc. Lond. B Biol. Sci.* 213, 249–277.

Meyer, A., and Galizia, C. G. (2011) Elemental and con?gural olfactory-coding by antennal lobeneurons of the honey bee (*Apis mellifera*). *J. Comp. Physiol. A* 198, 159–171.

Mombaerts, P. (1996). Targeting olfaction. *Curr. Opin. Neurobiol.* 6, 481–486.

Mwilaria, E. K., Ghatak, C., and Daly, K. C. (2008). Disruption of GABAA in the insect antennal lobe generally increases odor detection and discrimination thresholds. *Chem. Senses* 33, 267–281.

Olsson, S., Kuebler, L., Veit, D., Steck, K., Schmidt, A., Knaden, M., and Hansson, B. (2011). A novel multicomponent stimulus device for use in olfactory experiments. *J. Neurosci. Methods* 195, 1–9.

Pinero, J. C., Galizia, C. G., and Dorn, S. (2008). Synergistic behavioral responses of female oriental fruit moths (Lepidoptera:Tortricidae) to synthetic host plant-derived mixtures are mirrored by odor-evoked calcium activity in their antennal lobes. *J. Insect Physiol.* 54, 333–343.

Rabinovich, M., Huerta, R., and Laurent, G. (2008). Transient dynamics for neural processing. *Science* 321, 48–50.

Reisenman, C. E., Dacks, A. M., and Hildebrand, J. G. (2011) Local interneuron diversity in the primary olfactory center of the moth *Manduca sexta*. *J. Comp. Physiol. A* 197, 653–665.

Ressler, K. J., Sullivan, S. L., and Buck, L. B. (1994). A molecular dissection of spatial patterning in the olfactory system. *Curr. Opin. Neurobiol.* 4, 588–596.

Riffell, J. A., Lei, H., Christensen, T. A., and Hildebrand, J. G. (2009a). Characterization and coding of behaviorally significant odor mixtures. *Curr. Biol.* 19, 335–340.

Riffell, J. A., Lei, H., and Hildebrand, J. G. (2009b). Neural correlates of behavior in the moth *Manduca sexta* in response to complex odors. *Proc. Natl. Acad. Sci. U.S.A.* 106, 19219–19226.

Rospars, J. P., Lansky, P., Chaput, M., and Duchamp-Viret, P. (2008). Competitive and noncompetitive odorant interactions in the early neural coding of odorant mixtures. *J. Neurosci.* 28, 2659–2666.

Schmuker, M., Yamagata, N., Nawrot, M., and Menzel, R. (2011). Parallel representation of stimulus identity and intensity in a dual pathway model inspired by the olfactory system of the honeybee. *Front. Neuroeng.* 4:17. doi: 10.3389/fneng.2011.00017

Shang, Y., Claridge-Chang, A., Sjulson, L., Pypaert, M., and Miesenböck, G. (2007). Excitatory local circuits and their implications for olfactory processing in the fly antennal lobe. *Cell* 128, 601–612.

Silbering, A. F., and Galizia, C. G. (2007). Processing of odor mixtures in the Drosophila antennal lobe reveals both global inhibition and glomerulus-specific interactions. *J. Neurosci.* 27, 11966–11977.

Silbering, A. F., Okada, R., Ito, K., and Galizia, G. (2008). Olfactory information processing in the Drosophila antennal lobe: anything goes? *J. Neurosci.* 28, 13075–13087.

Su, C.-Y., Martelli, C., Emonet, T., and Carlson, J. R. (2011). Temporal coding of odor mixtures in an olfactory receptor neuron. *PNAS*, 108, 5075–5080.

Vosshall, L. (2000). Olfaction in Drosophila. *Curr. Opin. Neurobiol.* 10, 498–503.

Yaksi, E., and Wilson, R. I. (2010). Electrical coupling between olfactory glomeruli. *Neuron* 67, 1034–1047.

Yamagata, N., Schmuker, M., Szyszka, P., Mizunami, M., and Menzel, R. (2009). Differential odor processing in two olfactory pathways in the honeybee. *Front. Syst. Neurosci.* 3:16. doi: 10.3389/neuro.06.016.2009

**Conflict of Interest Statement:** The authors declare that the research was conducted in the absence of any commercial or financial relationships that could be construed as a potential conflict of interest.

*Received: 02 November 2011; accepted: 14 March 2012; published online: 19 April 2012.*

*Citation: Capurro A, Baroni F, Olsson SB, Kuebler LS, Karout S, Hansson BS and Pearce TC (2012) Non-linear blend coding in the moth antennal lobe emerges from random glomerular networks. Front. Neuroeng. **5**:6. doi: 10.3389/fneng.2012.00006*

The Journal of Experimental Biology 207, 2907-2916
Published by The Company of Biologists 2004
doi:10.1242/jeb.01126



# The electric fish *Brachyhypopomus pinnicaudatus* produces jamming avoidance responses to signals that are harmonically related to its own discharges

Alberto Capurro[1,2,*] and Khashayar Pakdaman[3]

[1]*Instituto de Física, Universidade de São Paulo (USP), Rua do Matão, Travessa R187, Cidade Universitaria, Butantã, 05508-900 São Paulo, Brasil,* [2]*Instituto de Investigaciones Biológicas Clemente Estable, Departamento de Neurofisiologia, Facultad de Ciencias, Avenida Italia 3318, Montevideo 11600, Uruguay* and [3]*Institut Jacques Monod, CNRS, Universites Paris 6, Paris 7, 2 Place Jussieu, 75251 Paris Cedex 05, France*

*Author for correspondence at address 1 (e-mail: alberto@fma.if.usp.br)

*Accepted 3 June 2004*

**Summary**

**Jamming avoidance responses (JARs) are exhibited by pairs of pulse type electric fish that discharge with similar frequencies whenever their individual pulses are about to coincide: responses consist of the transient shortenings in inter-discharge intervals in the fish with the higher frequency. This study describes and models novel forms of JARs observed in sexually mature male or female *Brachyhypopomus pinnicaudatus*.**

**One novel JAR was observed in male–female pairs in their natural habitat. It happened when the baseline frequencies were not similar but, rather, when one was almost twice that of the other; moreover, the transient interval shortenings occurred not in the fish with the higher frequency but in the slower one.**

**Transient interval shortenings similar to those in all natural JARs were observed in individual fish in tanks and submitted to periodic electrical pulse trains. They happened not only when pulse frequencies were slightly lower than the unperturbed frequency emitted by the fish but also when slightly lower than the frequency's sub- or higher harmonics (e.g. one half or twice).**

**The proposed model satisfactorily reproduces all experimental observations. In it, forthcoming inter-pulse intervals reflect the differences between the cophases of pulses that arrive within the 'sensitive windows' belonging to either consecutive (i.e. one and the next) or alternating (e.g. every other, every three) intervals.**

**Paired pulse fish embody interacting oscillators, and, in particular, JARs embody either quasiperiodic phase walk-throughs and intermittencies or periodic and locked forms. Hence, their study would profit by the powerful theories and approaches advanced by nonlinear dynamics.**

Key words: electric organ discharge, jamming avoidance response, electric fish, inter-pulse interval, transient interval shortening.

## Introduction

South and central American electric fish use a specialized electric organ in their tail to generate an electric organ discharge (EOD). The EOD generates in the surrounding water a field detected by electroreceptors in the skin of the fish. Primary afferent fibers transmit this information to the electric lobe and other sensory nuclei, in turn connected to pre-pacemaker centers that provide direct synaptic input to the medullary pacemaker centers controlling the electromotoneurons: thus, a closed loop is involved (for comprehensive reviews, see Carr and Maler, 1986; Bastian, 1986). This active electrosensory system has the main function of electrolocation in the watery environment, recognizing distortions of the EOD waveform by surrounding objects, as well as that of social electrocommunication using EOD rate modulations.

Electric fish species have been classified according to their EOD. In wave-type species, the duration of the individual discharges are of the same order as the intervals between them and the EODs are quasi-sinusoidal. In pulse-type species, the individual discharge is very brief in comparison with the intervals.

When several fish are close to one another, the discharges of one fish may perturb and jam the electrolocating abilities of others, regardless of whether socially interacting or not. Such interferences are minimized by changes in their EOD called jamming avoidance responses (JARs; Heiligenberg, 1977, 1986, 1991). JAR strategies differ with species type and, in some cases, between species of the same type (Heiligenberg, 1986). The best-understood strategy is that of the wave-type electric fish *Eigenmannia* and *Apteronotus leptorhynchus* (Watanabe and Takeda, 1963; Bullock et al., 1972; Heiligenberg, 1986; Kaunzinger and Kramer, 1995; Metzner, 1999). To avoid interference between the respective waves, the fish with the higher EOD frequency slightly increases its

frequency, while the fish with the lower frequency may slightly decrease it. This increases the frequency difference, prevents jamming and protects electrolocation. This type of JAR is also observed using an artificial jamming sinusoidal stimuli whose frequency is close to higher harmonics of the fish frequency but not to their subharmonics (e.g. Kaunzinger and Kramer, 1995). Other reports also indicate that wave-type fish can synchronize their EOD to sinusoidal stimuli during episodes where the EOD–stimulus phase relations remain constant (Gottschalk and Scheich, 1979).

In pulse-type species, EODs consist of short pulses separated by comparatively long intervals, and jamming occurs when two fish discharge simultaneously. Typical JARs arise when temporal coincidences are imminent and the fish whose EOD has the higher rate briefly shortens its EOD intervals, thus reducing the probability of jamming (Heiligenberg, 1974, 1976, 1986; Scheich et al., 1977; Heiligenberg et al., 1978; Capurro et al., 1998, 1999; Capurro and Malta, 2004). In some species, these transient interval shortenings in the faster fish may associate with simultaneous lengthenings in the fish with the lower rate (Heiligenberg, 1986; Perrone, 2003).

Studies of electromotor responses under jamming with artificial pulse trains have shown that the pulse-type fish is particularly sensitive to pulses that coincide with the EOD or occur just prior to it (e.g. 1 ms). These pulses distort the perceived map of the environment and perturb the electromotor response. The electrolocation performance tolerates well a single pulse–EOD coincidence and deteriorates only after multiple coincidences have involved successive EODs (e.g. 3–6 EODs; Heiligenberg, 1974, 1976, 1986; Heiligenberg et al., 1978).

Studies of the response to artificial pulses in pulse-type South American species have shown that the necessary condition for a single pulse to have an effect on the fish EOD is that it arrives within the late portion, referred to as the ‘sensitive window’, of the EOD period; thus, at least a minimum time after the preceding EOD referred to as ‘phase’ or ‘delay’ or, equivalently, at most a maximum time (5–15 ms) before the following EOD referred to as ‘cophase’ (Capurro et al., 1998). When this happens, the pulse induces a shortening of several successive EOD intervals, starting in the interval that follows the one containing the pulse. The maximum shortening is usually reached one or two intervals after the beginning of the response and from this point the intervals return exponentially to their value before the perturbation (Capurro et al., 1998). When two or more pulses arrive in sensitive windows, veritable JARs that involve 4–10 shortened intervals are observed. The JAR happen only when the successive phases of the pulses relative to the EOD slowly increase: there is, therefore, a sensitivity to the direction of the phase and cophase shifts (Heiligenberg, 1974; Baker, 1980, 1981; Capurro et al., 1999).

Some South American pulse-type species, in addition to the JARs with transient EOD interval changes described above, also perform JARs involving sustained EOD frequency shifts and synchronization bouts during which phases remain almost constant (Heiligenberg, 1974; Westby, 1979, 1981; Capurro et al., 1999; Perrone, 2003).

The present paper has two related purposes. The strictly biological purpose is to describe JARs not yet reported as far as we know: they arise in pairs of pulse-type fish in their natural habitat and are evoked by signals harmonically related to the EOD. The formal purpose is to describe a mathematical model that reproduces the transient interval shortenings evoked in an isolated fish by pulse trains at harmonic and subharmonic frequencies with respect to the EOD.

## Materials and methods

### *Recording of interactions in the natural environment and the laboratory*

The field recording that motivated the present study was performed immediately after sunset (the active moment in the circadian cycle of the fish) during the breeding season at the natural habitat (Laguna del Tigre, Departamento de Treinta y Tres, Uruguay) (Capurro, 1999; Silva, 2002; Perrone, 2003). A pair, one male and one female, of sexually mature 10–15 cm-long *Brachyhypopomus pinnicaudatus* (Hopkins) (Hopkins et al., 1990) was captured and allowed to move freely in a fenestrated plastic tank (50 cm×50 cm×20 cm height) with circulating lake water (conductivity 300 μS, temperature 20–25°C). Two pairs of electrodes, consisting of 45 cm-long wires along the four bottom edges of the tank, detected the EOD voltages. Voltage differences were measured between each pair of parallel wires, thus the paired electrodes were oriented orthogonally. Voltages were amplified and displayed on an oscilloscope and stored on a stereo audio tape.

Other recordings were obtained in the laboratory after sunset from other sexually mature fish pairs in a tank filled with water from the lake and using the same recording and display set-ups. Storage was on stereo video tapes.

The voltage records were digitized at 5–20 kHz. A peak detection algorithm recognized the peak of the EOD’s head positive wave. Although the recorded voltages depend on the position of the animals relative to the electrodes, generally the male has higher voltages. As two orthogonal electrode pairs were used, amplitude differences in at least one of the pairs could often be found. Hence, the discharges of the male and the female were discriminated by amplitude, within data segments where the voltage reached by the two EOD peaks was clearly different to the naked eye. Lists, one for the male and another for the female, of the instants when each EOD pulse occurred were obtained and used to construct the interval and delay plots and to detect and count the number of simultaneous discharges.

When the two EODs coincided in time it was possible to miss one of them because the two peaks may appear as only one in the digitized file. However, when comparing the digitized and analog records it was clear that the sampling rate was sufficiently high to avoid most of these errors. In the few cases where coincidences were not distinguished in the digitized files, the same time was adjudicated to both signals. In certain cases, the position of the animals made detection of the positive EOD peak of one fish impossible. As, in some of

these cases, the negative peak of the fish could be easily detected, the time between the positive and the negative EOD peaks was subtracted from the list of discharging times of the fish, so as to consider always the peaks of the positive wave.

Mature animals during the breeding season exhibit sexually dimorphic EOD waveforms (Hopkins et al., 1990; Silva, 2002). The head negative wave lasts longer and has larger amplitude in the male, providing a reliable criterion for separation in voltage recordings. Using this criterion, we checked whether all individual discharges had been detected and assigned correctly to the male or the female. Errors apparent to the naked eye were corrected by typing into the ASCII files of the EOD times.

### *Stimulation with artificial pulses*

Electric pulses, evoking in discharging fish responses similar to those observed in natural interactions, are used widely to study pulse-type fish (e.g. Heiligenberg, 1974; Westby, 1975; Heiligenberg et al., 1978; Baker, 1980, 1981). Stimuli were tested in sexually mature isolated fish (10–12 cm length) at day time (room temperature 15–20°C). Individual fish (male or female) were placed in a tank (50 cm×25 cm×25 cm height). They spontaneously entered a plastic tube, open at both ends, and did not change their position during the recordings. The recording electrodes were a pair, one close to the head and the other to the tail, and the recorded signal was amplified and displayed on an oscilloscope. The stimulating pair was one positive 4 cm lateral from the tail and one negative 4 cm lateral from the head. A stimulator delivered square, 2 ms-duration pulses such that the head electrode was negative with respect to the first wave of the fish EOD and arising at equal intervals with different frequencies. Pulse voltage was set to about half that of the EOD head negative wave. This arrangement emulates the EOD of a second fish placed at a short distance from the first.

As the oscilloscope was triggered with the EOD, the relative position of the pulses on the screen served to adjust their generation to the beating frequency. Using this guide, the stimulus frequency was set with a hand-wheel to exhibit ratios of 1:1, 2:1, 3:1 and 1:2 relative to the EOD (corresponding to different harmonics and to the first sub-harmonic). Observations lasted 1–5 min. As explained above, records were obtained and digitized, events (EODs, pulses) were identified, and lists with the respective times of occurrence were obtained. These lists served to construct the joint 'interval and delay' plots whose abscissa is ongoing time. Each point in the graph of intervals corresponds to a single EOD, the abscissa corresponds to the instant when that EOD occurred and the ordinate corresponds to the interval between it and the preceding EOD. Each point in the graph of delays corresponds to a single pulse, the abscissa corresponds to the instant when that pulse occurred and the ordinate corresponds to the interval between it and the preceding EOD (delay or phase).

### *Mathematical model*

A model referred to here as X and published previously first used autoregressive (AR) procedures to reproduce the resting EOD (see Unperturbed inter-discharge intervals; Capurro et al., 1998, 1999, 2001). In addition, it realistically postulated that only single pulses in a sensitive window far from the last EOD event and close to the anticipated next one would shorten the next intervals (see Response to single pulse). It also postulated that JARs would be triggered only if consecutive pulses swept consecutive sensitive windows from left to right (see Response to pulse trains); this meant that intervals separating each pulse from the preceding EOD (phases or delays) slowly increased from one to the next; i.e. intervals to the forthcoming EOD (cophases or co-delays) slowly decreased. Model X accounts for the transient interval shortenings observed in a *Gymnotus carapo* after a single pulse arrives within the sensitive window, as well as for the response to trains of pulses at frequencies close to that of the EOD.

In *Brachyhypopomus pinnicaudatus*, model X reproduced the interaction in which the two fish discharged at close rates. However, it did not reproduce findings when the frequency of the second fish EOD or of the pulse trains was twice as fast or twice as slow. So as to accommodate these failures, a new model, referred to as Z+, will be proposed. Model Z+, as with model X, used AR procedures to reproduce the resting EOD and postulated that only pulses arriving in a sensitive window would shorten the intervals. Two other rules were incorporated. One rule allowed the perturbing events (EODs, pulses) in consecutive sensitive windows to not be consecutive, so that other perturbing events arrive between two consecutive sensitive windows. This means that perturbations can exhibit higher frequencies than the EOD, including those slightly lower than two or more times that of the fish. It means also that the sweeping velocity, i.e. the changes in phases and cophases, is evaluated for pulses within successive, not necessarily consecutive, sensitive windows. It is as if the fish, when deciding whether to generate a JAR, concentrates on the pulses within sensitive windows and ignores those outside of it. The model with this first addition is referred as to Z. The final rule that completed Z+ was that JARs would be triggered when pulses swept from left to right (increasing delays or phases, decreasing cophases) successive sensitive windows that did not have to be consecutive. This means that perturbations can exhibit lower frequencies than the EOD, including those slightly lower than half that of the fish. In the following, the mathematical formulation of models X, Z and Z+ is presented together with the parameter set used in the simulations.

#### *Unperturbed inter-discharge intervals*

In both models (X and Z+), each inter-pulse interval of the spontaneous EOD is assigned according to the following equations:

$$I_{n+1} = M_{n+1} + N_{n+1}\,, \tag{1}$$

$$N_{n+1} = \rho1\times N_n + \rho2\times N_{n-1} + \rho3\times N_{n-2} + \rho4\times N_{n-3} + \sigma\times W_{n+1}\,, \tag{2}$$

where $I_{n+1}$ is the $(n+1)$th interval, and $M_{n+1}$ is the mean of all preceding intervals. $N_{n+1}$, representing the variability of the

spontaneous discharge, is computed with the AR scheme of equation 2, where the $W_i$ are independent identically distributed truncated centered Gaussian random variables, $\sigma$ controls the noise amplitude and the coefficients $\rho_i$ control the level of autocorrection (Capurro et al., 2001).

*Response to single pulse*

The 'cophase $C(t)$' (or co-delay) of a perturbing pulse is the interval from it to the next EOD. The 'phase' or 'delay' of the pulse is the interval from it to the previous EOD and will be used in the interval and delay plots. The interval containing the pulse equals the sum of the delay or phase plus the cophase. In both models, the response of the system to a pulse arriving at time $t_0$ between the $n$(th) and ($n$+1)th discharges depends on its location within the interval between these discharges, thus on its delay and cophase $C(t_0)$; this model uses the cophase but could be enunciated equivalently in terms of the delay.

So as to be effective and shorten the following intervals, pulses must arrive within the sensitive window: this is represented by the condition that the cophase must be smaller than a value $C_H$ called 'maximal cophase'. When $C(t_0)<C_H$, the means of the following inter-discharge intervals are shortened according to:

$$M_n^+ = M_n^- - G_1[C(t_0)] , \quad (3)$$

$$M_{n+1}^+ = M_{n+1}^- - G_2[C(t_0)] , \quad (4)$$

where $M_n^+$ and $M_{n+1}^+$ represent the new values of the mean intervals after the perturbation, while $M_n^-$ and $M_{n+1}^-$ are those before the perturbation. $G_1$ and $G_2$ are piece-wise linear functions given by:

$$G_i(X) = 0, \text{ if } X>C_H , \quad (5)$$

$$G_i(X) = \lambda_i[(C_H - X)/C_H], \text{ if } B<X<C_H , \quad (6)$$

$$G_i(X) = \lambda_i X [(C_H - B)/(BC_H)], \text{ if } 0<X<B , \quad (7)$$

where $\lambda_1$, $\lambda_2$ and $B$ ($<C_H$) are positive constants that depend on the strength of the stimulation. After an interval shortening, if no further perturbation occurs during the sensitive window, the following mean intervals are computed according to:

$$M_{n+1} = (1 - \alpha) \times M_n + (\alpha \times M^*) , \quad (8)$$

where $\alpha$ is the recovery factor, and $M^*$ is the natural interval. Hence, following interval shortenings due to the perturbation, their means, $M_n$, return monotonically to $M^*$.

*Response to pulse trains*

Other conditions must be complied with for pulse trains (i.e. two or more pulses) to evoke the interval shortenings; these conditions differed in models X and Z. In model X (Capurro et al., 1998), the condition reads:

$$0<C(i) - C(i+1)<K , \quad (9)$$

where $C(i)$ and $C(i+1)$ are the cophases of the $i$th and ($i$+1)th pulses, falling in the sensitive windows of two consecutive EOD intervals; no other pulses arrive between the $i$th and ($i$+1)th pulses, which, therefore, are consecutive [in the particular cases where the ($i$+1)th pulse falls in the sensitive window but the $n$th does not, the response also occurs]. This condition requires that, for EOD interval shortenings to occur, consecutive pulses must sweep consecutive EOD cycles from left to right advancing by less than $K$. Parameter $K$ prevents responses to fast left to right sweeps and to right to left sweeps at the moments when the cophase jumps from a large value (just under that of the interval) to a small value close to 0. At this moment, $0<C(i)–C(i+1)$ is met (i.e. the cophases are decreasing) but not $C(i)–C(i+1)<K$.

In model Z, the condition to evoke interval shortenings reads:

$$0<C(i) - C(i+j)<K , \quad (10)$$

where $C(i)$ and $C(i+j)$ are the cophases of the $i$th and ($i$+$j$)th pulses falling in the sensitive windows of two consecutive EOD intervals; $j$–1 pulses arrive between the $i$th and ($i$+$j$)th pulses, which, therefore, are not necessarily consecutive. Hence, for the JAR at close EOD periods $j$=1 (Fig. 2), and for the JAR in which the EOD period of the slower fish is close to twice the period of the faster fish (Fig. 2B) $j$=2 [in the particular cases where the ($i$+1)th pulse falls in the sensitive window but the $n$th does not, the response also occurs].

For low-frequency stimulation, not all sensitive windows receive pulses. For this reason, the condition for interval shortenings was further modified, giving rise to the model Z+. The pulses $i$th and ($i$+$j$)th need not arrive in consecutive sensitive windows; i.e. between the two pulses there may be one (or more) EOD cycles that did not receive a pulse. In other words, the condition that the pulses must arrive in consecutive sensitive windows to evoke a response was relaxed. The impact of this last property of model Z+ is that it allows reproduction of the response to pulse trains at sub-harmonic frequencies with respect to the EOD.

*Selection of parameter values*

Parameter values were maintained invariant in each simulation with the exception of $M^*$ values, which changed from one to another. The AR coefficients, $\rho_i$, were estimated from the EOD intervals of an isolated fish using methods in Capurro et al. (2001). The parameters that control the magnitude of the interval shortenings, $\lambda_i$, as well as those that control the amplitude of the background variability ($\sigma$) and the recovery of the intervals after an interval shortening ($\alpha$) were set to reproduce the record in Fig. 2B. $C_H$ and $B$, which affect the sensitive window as judged by the interval shortening *vs* cophase curve, allowed phase–cophase plots similar to those of a fish stimulated with low-frequency (0.2 Hz) artificial pulses (e.g. Capurro et al., 1999); they reproduced adequately interval and delay plots such as that in Fig. 2B. The commonly used parameter set was the following: $\lambda_1$=2.9 ms; $\lambda_2$=3.0 ms; $C_H$=6.0 ms; $B$=0.2 ms; $K$=5.0 ms; $\alpha$=0.4; $\sigma$ of the slow train=0.3; $\sigma$ of the fast train=0.0025; AR coefficients of both trains, $\rho_1$=0.6662, $\rho_2$=0.2108, $\rho_3$=0.0685, $\rho_4$=0.0052.

The critical interval and frequency ratios are those of the

EODs when not perturbed by pulses. *M**, the mean interval without perturbations, varied in each numerical simulation. The values used for each fish are provided in the figure captions. As such values were not available in the field, they were estimated from the interacting fish record using the low-variability EOD period of one fish and the portions without shortened intervals between JARs in the other.

### *Coincidences*

As suggested by behavioral work, we call 'coincidence' the presence of a perturbing event within 1 ms back and/or forward from a reference EOD event. 'Successive coincidences' are those that involve several consecutive EODs; they are 'double', 'triple', etc. when happening in two, three, etc. consecutive EODs. Coincidences were counted with a program based on a cumulative algorithm that scanned the series of discharging times from fish or numerical simulations. Every time a single coincidence was repeated in the next EOD cycle, the algorithm added a double coincidence to the list (plus a second single one); if the coincidence repeated again in the following cycle, a triple coincidence was counted together with a second double coincidence and a third single one, and so forth. The slower fish EOD was used as the reference event. When both fish exhibit almost the same instantaneous frequency, the number of coincidences is the same using the fast or the slow fish as reference, but this does not hold in cases when the fast fish discharges at higher harmonics of the slow fish frequency because the faster fish can fire more than once between coincidences. We focused upon multiple coincidences that are physiologically more significant than single ones (see Introduction) and, in particular, on double ones because the coincidences of higher order (i.e. those repeated in three or more successive EOD cycles) can occur only if a double coincidence has already taken place.

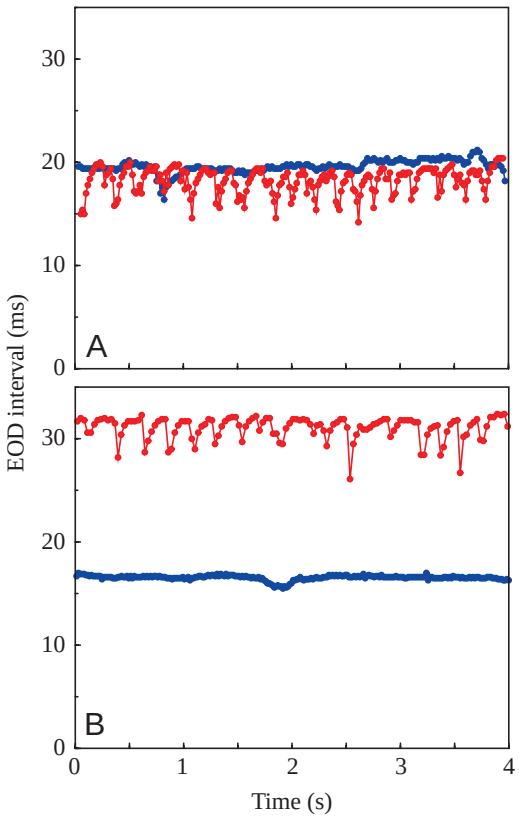


Fig. 1. Jamming avoidance responses (JARs) in interacting pairs of *Brachyhypopomus pinnicaudatus*. Different pairs in A and B. Inter-EOD event intervals (ms) as a function of ongoing time (s). Female, red trace; male, blue trace. Mean intervals estimated from portions without transient interval shortenings. (A) Interval ratio of female to male close to 1:1 (in the laboratory). Mean intervals during the interaction: female, 19.5 ms; male, 20 ms. (B) Interval ratio of female to male close to 2:1 (natural environment). Mean intervals during the interaction: female, 36.0 ms; male, 18.0 ms.

## Results

This section describes JARs observed in freely behaving fish and in response to artificial stimuli, together with possible models for both situations.

### *JARs in freely behaving fish pairs*

Fig. 1, with the inter-EOD intervals of the female (red) and the male (blue) plotted against time, shows the electromotor interactions of freely swimming sexually mature fish. Records in Fig. 1A were obtained in a tank in the laboratory: the female:male mean interval ratio was just under 1:1, with the female's intervals shorter (i.e. instantaneous rates higher) than the male's. During the interaction, the male's intervals (blue trace) are practically invariant. The female's intervals (red trace), on the other hand, fluctuate. Fluctuations include first brief epochs where intervals are longest, having almost the same duration as those of male's; these longer intervals are close to those of the female's EOD when unperturbed. Interspersed between these epochs are irregularly recurring transient interval shortenings (instantaneous rate increases), which are installed rapidly, reaching local interval minima over a few steps, and then return gradually to the longer values. These transient shortenings by the female prevented EOD coincidences and, therefore, constitute veritable JARs; there were no double coincidences in the record.

Records in Fig. 1B were obtained from a fish pair studied in their natural environment (Laguna Tigre). The female:male mean interval ratio was just under 2:1, with the female's intervals longer (i.e. instantaneous rates lower) than the male's. As in Fig. 1A, the male's intervals (blue) are invariant but the female's (red) fluctuate between alternating epochs with relatively stationary longer intervals at about twice those of the male and rapidly installed, slowly recovering transient shortenings. Also these transient shortenings prevented EOD coincidences and thus also constitute veritable JARs; there was only one double coincidence in the record. This, as far as we know, is the first report in pulse fish of JARs where the slower fish shorten their EOD intervals and the male discharges just under the first harmonic of the female's EOD.

Fig. 2A,B shows interval and delay plots, with the EOD

intervals (circles) of one fish and the delays (asterisks) with respect to the first fish of the EOD pulses from the second. These data are selected segments from the records shown in Fig. 1. In Fig. 2A, the female:male mean interval ratio is about 1:1 (mean rates about the same). Delays increase monotonically, sweeping, sliding or walking across the interval of the first fish; when reaching a maximum value just under that interval, they jump to a small value close to 0 and grow along steps that individually are similar to (although not identical) and are in about the same number as those of the previous sweep. A coincidence exists when delays are practically equal to the interval and plots superimpose or, as at 0.75 s, delays are equal to zero. When the monotonically increasing delays approach the interval's value, the paired EODs drift towards a coincidence, and, when sufficiently close, interval shortenings (Fig. 2A) occur rapidly over a few EODs: shortenings avoid coincidences and thus constitute JARs.

In Fig. 2B, the female:male mean interval ratio is about 2:1 (mean rate ratio about 1:2). Delays increase along a zigzag path, with alternating larger and smaller values; considered separately, the larger and smaller values have the same slopes, similar to those in Fig. 2A. The faster fish fires twice within each interval of the slower EOD: the first time is with a shorter delay and prior to the sensitive window; the second, with a longer delay, is within the sensitive window and shortens the extant interval. This finding provides the key for model Z to reproduce this novel behavior (see Response to pulse trains).

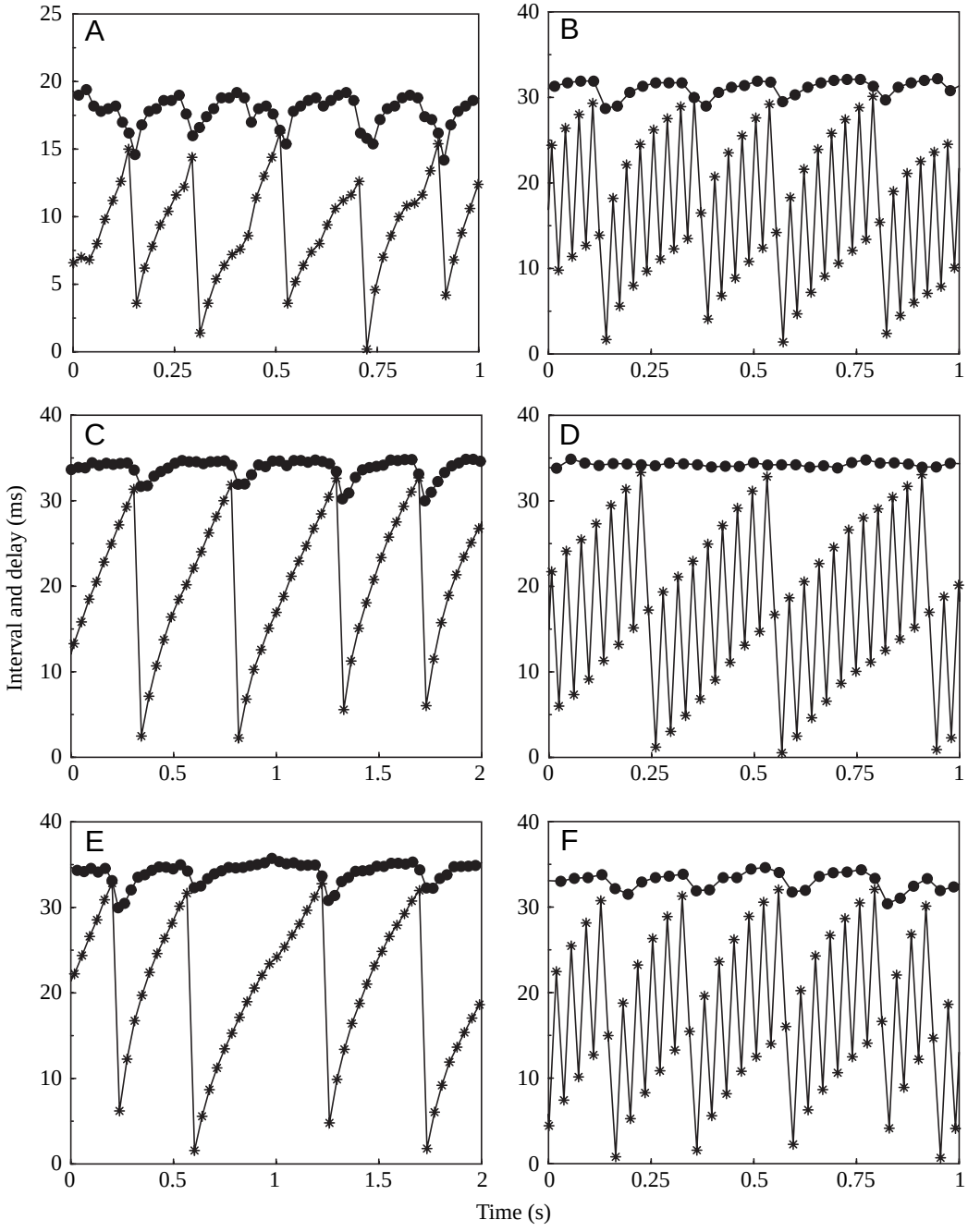


Fig. 2. Jamming avoidance responses (JARs) in different settings or simulated. Interval and delay plots. (A,B) Female electric organ discharge (EOD) intervals are represented by circles; male EOD delay with respect to the female EOD are represented by asterisks plus lines. (A) Fish pair in laboratory settings (depicted in Fig. 1A). (B) Fish pair in natural environment (depicted in Fig. 1B). (C–F) Data generated numerically. Female train shown as interval *vs* time (circles); male train shown as delay *vs* time (asterisks plus lines). $M^*$, mean interval in the absence of perturbations. (C) Data generated with model X attempting to mimic the situation in A; female faster train ($M^*$=36.0 ms); male slower train ($M^*$=36.5 ms). (D) Data generated with model Z attempting to mimic the situation in B. Female slower train ($M^*$=36.0 ms); male faster train ($M^*$=18.0 ms). (E) Data generated with model Z attempting to mimic the situation in A. Female faster train ($M^*$=36.0 ms); male slower train ($M^*$=36.5 ms). (F) Data generated with model Z attempting to mimic the situation in B. Female slower train ($M^*$=36.0 ms); male faster train ($M^*$=18.0 ms).

While model X reproduces results in Fig. 2A well, with the two fish discharging at close EOD frequencies (Fig. 2C), it fails to reproduce the case where one fish fires close to twice as fast as the other (Fig. 2D). Using model Z, both cases could be reproduced (Fig. 2E,F).

Fig. 3A shows the same data set as Fig. 2B but, in this case, represents the male's faster EOD as interval *vs* time and the female's EOD as delay *vs* time. Note the absence of transient interval shortenings in the male's EOD. Fig. 3B shows the same data set as Fig. 2F but, in this case, represents the male's faster EOD as interval *vs* time and the female's EOD as delay *vs* time. These data were generated numerically with model Z attempting to reproduce the situation shown in Fig. 3A. Note that the train representing the male does not produce transient interval shortenings.

The number of coincidences found in the fish interactions depicted in Fig. 1 is within the confidence intervals of the distribution produced by 20 realizations of model Z having the same duration as the recordings; simulation segments are in Fig. 2E,F. The very low number of coincidences (i.e. 0 for Fig. 1A and 1 for Fig. 1B) is indicative of the high efficiency of the JAR. Control simulations of the same duration and relation of periods but without transient interval shortenings ($\lambda_i$=0) included more than 10 successive coincident discharges. When $\lambda_i$=0, successive coincidences occur only when one simulated train fires close to integer multiples of the discharging rate of the other. If transient interval shortenings are allowed in the simulations, model X removes only coincidences when EOD period ratios are close to 1:1. Model Z also removes most of the coincidences that occur when periods are at integral multiples.

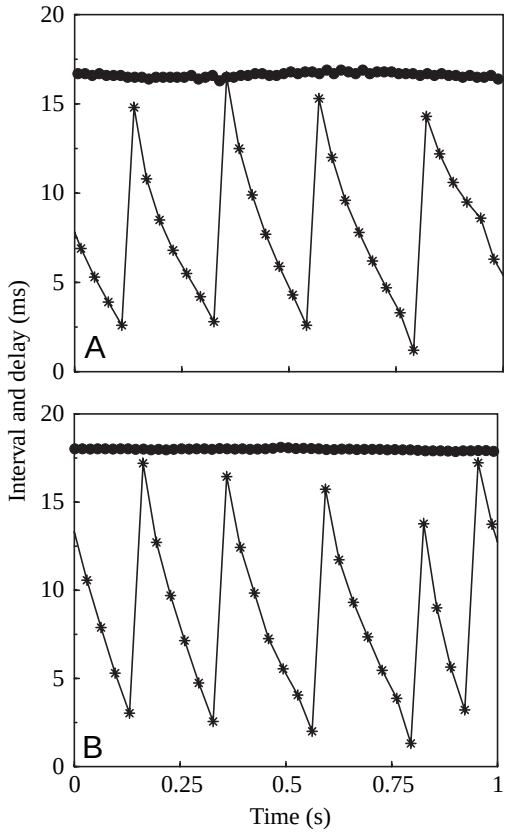


Fig. 3. Jamming avoidance responses (JARs) with 2:1 female:male period ratios: natural and simulated. Interval and delay plots. Fast male electric organ discharge (EOD) represented by intervals (circles); slow female EOD represented by its delay with respect to the male EOD (asterisks plus lines). (A) Fish pair in natural environment (same as in Fig. 2B). (B) Simulation using the incomplete version of model Z (same as in Fig. 2F). Male fast train ($M$*=18.0 ms); female slow train ($M$*=36.0 ms).

### *JARs to artificial pulses*

The same reactions observed during the behavioral interactions (Fig. 1A,B) could be evoked in isolated specimens of both sexes stimulated with artificial pulse trains. The responses were the same, even though, because fish were studied during the inactive period of the circadian cycle, the EOD intervals were larger than those depicted in Figs 1B, 2B.

Fig. 4 displays interval and delay plots, with fish EODs represented by intervals (black circles) and pulse trains represented by delays (asterisks); the pulse train is also represented by intervals (thick gray line). Responses in Fig. 4A,B are very similar to those in Fig. 2A,B, respectively, and can be described in the same manner.

Fig. 4C includes separate EOD portions, both stationary but each at different interval values; the pulse train is the same throughout. The first half, where the longest intervals were practically equal to twice the interpulse interval (rates about one half), shows obvious JARs. The second half, where visibly the EOD intervals were shorter and the alternating delay slopes greater than in the first, had no JARs. Fig. 4B and C (first part) illustrate JAR's in, respectively, male and female specimens: therefore, JARs depend on mechanisms and computations shared by both sexes. In Fig. 4D, the period of the stimulus train (thick gray line) was varied: JARs were present in the first 3 s, where the longest EOD intervals were practically equal to twice the pulse intervals (rates about one half), but disappeared when pulse intervals were lengthened. Thus, Fig. 4C,D shows that JARs vanish whenever the regime departs, because either EODs or pulses changed, from the 2:1 ratio.

JARs also occurred when the mean EOD to pulse interval ratio was about 3:1, as in Fig. 4E, and 4:1 (not shown). These situations have not been observed in naturally behaving fish pairs but should be looked for: conceivably, they are hard to encounter because, as the higher order lockings between interacting pacemakers, their domains may be small and susceptible to the inevitable noise. As in Fig. 4B–D, delays increase along zigzags with successively larger, intermediate and smaller values that, taken separately, have similar slopes.

Fig. 5A illustrates JARs arising when a first spike train (generated with the same parameter set used for the slower train of Fig. 2D,F) and a slower second train, whose frequency was almost half that of the first, are present. Model Z+ reproduces this situation (Fig. 5C), but model Z does not (Fig. 5B). Model Z+ also shows JARs at 1:1, 2:1 and 3:1 relation of periods (not shown).

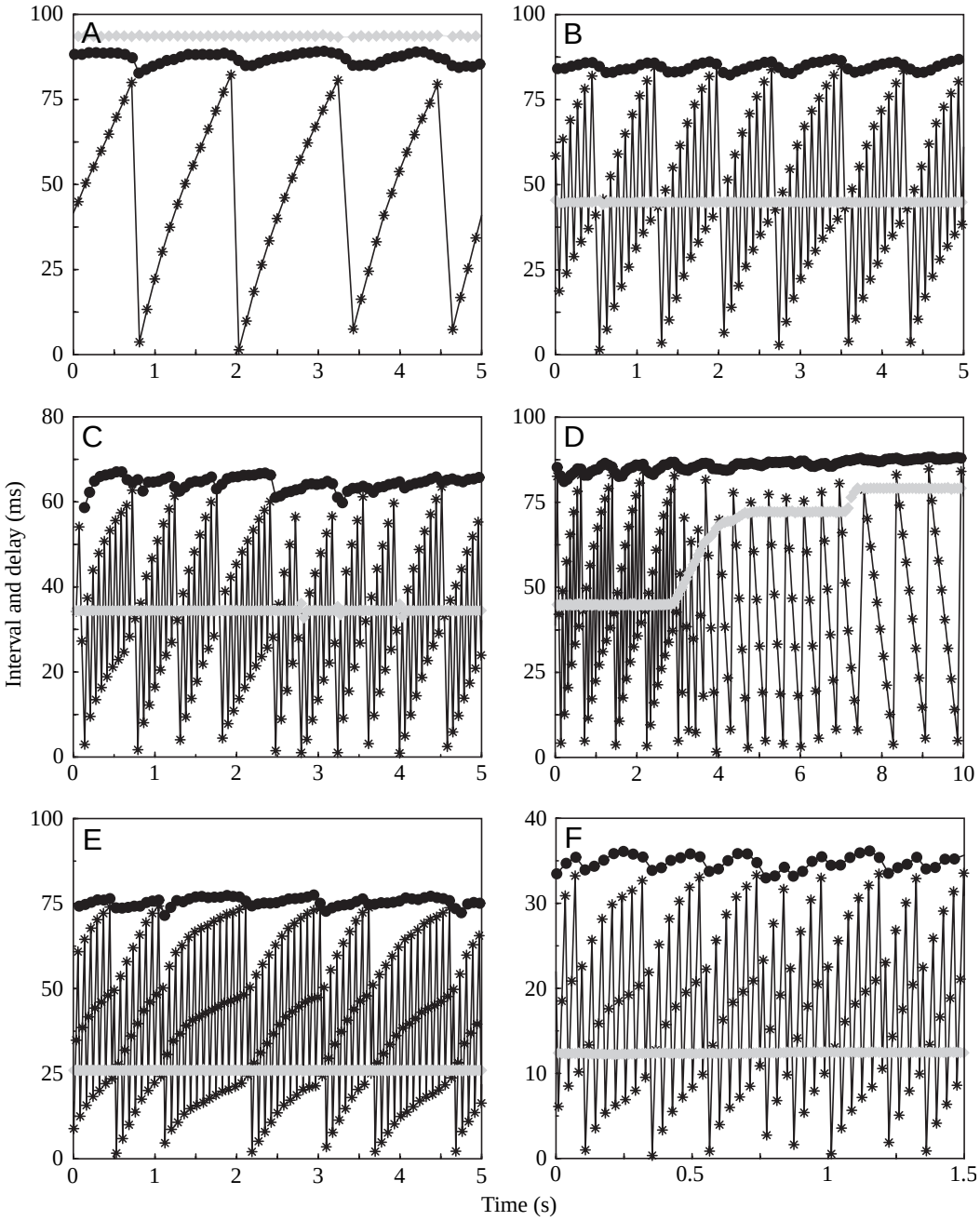


Fig. 4. Jamming avoidance responses (JARs) and artificial pulses. Interval and delay plots. Isolated fish electric organ discharge (EOD) represented by intervals (circles); artificial pulses represented by delays relative to the EOD (asterisks with lines) and intervals (thick gray line). (A) 1:1 period ratio (male EOD). (B) 2:1 period ratio (male EOD). (C) JARs (female EOD) arise with 2:1 period ratios but not when those ratios vary because EOD intervals change. (D) JARs (male EOD) with 2:1 period ratios but not when those ratios vary because pulse intervals change. (E) 3:1 period ratio (female EOD). (F) Numerically generated data referring to the situation depicted in E. The slow train is plotted as interval *vs* time with black circles and represents the fish. The fast train represents the artificial pulses and is plotted both as delay *vs* time (asterisks plus lines) and as interval *vs* time (thick gray line). $M^*$ of the fast train=12.0 ms; $M^*$ of the slow train=36 ms.

## Discussion

This study adds novel features to the catalog of JARs performed by pulse-type electric fish. The main finding is that the fish is able to respond by JARs to pulse trains delivered not only at frequencies close to its EOD but also at frequencies close to its higher harmonics and sub-harmonics. This responsiveness is broader than that of the wave-type fish that, while responding to frequencies close to the EOD and its higher harmonics, does not respond to its sub-harmonics (Kaunzinger and Kramer, 1995). The second contribution of the paper is to develop a mathematical model able to reproduce the reported behaviors. The ethological relevance of the JAR at 2:1 relation of periods, the models and the conjectures about the dynamical behaviors involved are discussed below.

### *Ethological significance of the JAR at 2:1 relation of periods*

From an ethological point of view, the more relevant finding reported here was the JAR triggered in one fish by another's EOD whose period was close to half its own and thus whose frequency was close to its first harmonic. This JAR was witnessed in fish behaving freely in their natural habitat and, therefore, can safely be assigned a genuine ethological significance. The situation in which the period of one fish reaches near twice the period of the other fish can occur often during the breeding season. In the first hours of the night, when the animals have their active period, the male increases its frequency and maintains it with low variability in a high value. This sustained frequency increase is correlated with the locomotor display and electrocommunicatory signals of

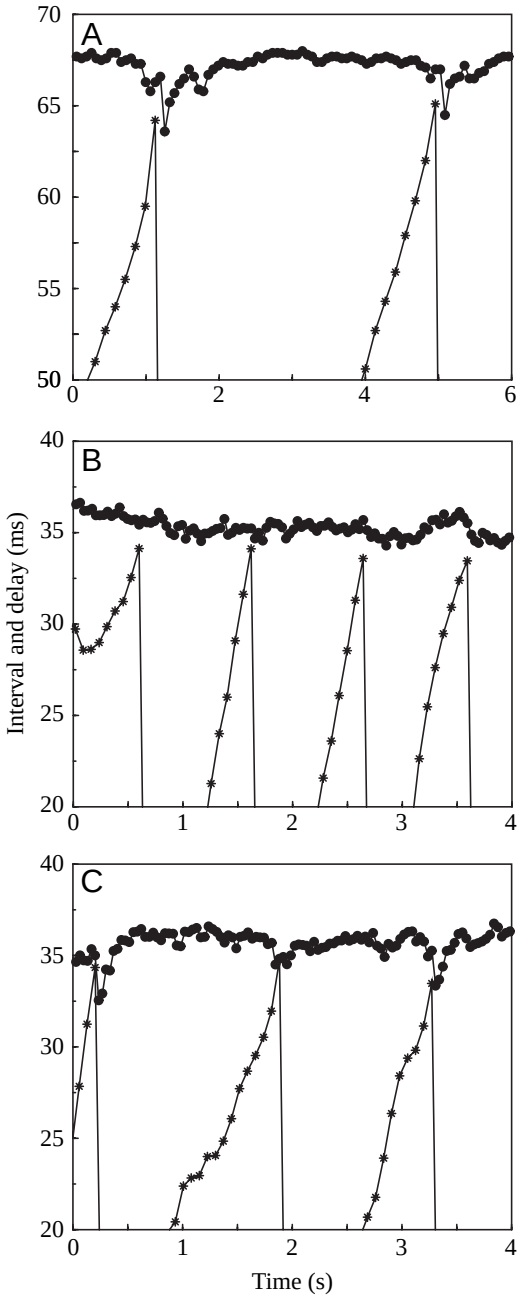


Fig. 5. Jamming avoidance responses (JARs) with 1:2 'electric organ discharge (EOD) to pulse' period ratios: natural and simulated. Interval and delay plots. EODs represented by intervals (black circles); artificial pulses represented by delays relative to the EOD (asterisks with lines). (A) Live fish: mean interval=68.0 ms; pulse interval=141.3 ms. (B) Failure of incomplete model Z, which responds only if pulses occur at consecutive sensitive windows. For B and C, fast train $M^*$=36.0 ms; slow train $M^*$=73.0 ms. (C) Success of complete model Z+, which responds to pulses arriving either at consecutive or every other sensitive window.

courtship and exceeds those during the active period in sexually immature specimens (Macadar et al., 2001; Quintana et al., 2002; Silva, 2002; Perrone, 2003). It may lead to a 2:1 relation of periods (e.g. Fig. 1B). When, as can happen, the female also increases her mean frequency, interactions may be without transient interval shortenings (if the frequencies are far from harmonical relations) or an interaction with transients may be produced by the faster fish (if both frequencies are close to one another; e.g. Fig. 1A).

Observations in the laboratory using artificial pulses showed that JARs were identical in both sexes, suggesting that, in spite of different EOD wave-shapes and external phenotypes (Hopkins et al., 1990; Silva, 2002), both sexes use the same computations. Moreover, the same kind of JARs triggered by harmonically related pulse trains were found in immature specimens with minor sexual dimorphism in their external phenotypes; hence, contrary to the general behavioral aspects of courting, the JAR does not depend on full maturity. Longer observations of natural interactions are needed, however, to evaluate a possible sexual influence in the behavioral determination of the $M^*$ values.

### *Models for JARs*

This study improves on an earlier model (X), proposing models Z and Z+. In all three models, the fish performing the JAR responds only to pulses within a sensitive window that starts at a characteristic instant preceding the forthcoming EOD ($C_H$). Also, in all models, successive effective pulses have to scan the EOD's sensitive windows slowly and from left to right, i.e. with increasing delays and decreasing cophases. This requires a mechanism that stores the position in the cycle of each perturbation and compares it with that of later ones. However, models differ in the identities of the arriving pulses involved in the influential scans.

In model X, proposed previously (Capurro et al., 1998, 1999), the response occurs only if windows in consecutive EOD cycles are scanned by successive pulses that are also consecutive. This model reproduces only situations in which the frequencies and periods of the two EODs are close. With this model, coincidences are avoided through brief interval shortenings in the discharge of the fish having the higher rate (shorter period) of the pair. In model Z, the response occurs if windows in consecutive EOD cycles are scanned by successive pulses that need not necessarily be consecutive. This model also reproduces situations in which the frequency of one EOD is close to two or three times that of the first. Coincidences are avoided through brief interval shortenings in the discharge of the fish having the slower rate (larger period) of the pair.

In model Z+, the response occurs if windows in either consecutive EOD cycles or windows belonging in every other EOD cycle are scanned; perturbations need not be consecutive pulses. Sensitivity to perturbations in every other window requires storage across EOD cycles without arrivals, one at least. Model Z+, reproducing satisfactorily all outcomes encountered in natural habitats and using artificial pulse trains, accounts well for fish behavior. These experiments showed that JARs arise also when EOD to pulse interval ratios are 1:2, involving one interposed cycle without perturbation; further work in progress is examining their maximum number and thus the duration of this memory. Also in progress are experiments

using pulse trains with interval ratios such as 2:3 and 3:2, as well as pulses with different amplitudes.

### *JARs as dynamical behaviors*

Below, we attempt to justify briefly the potential usefulness for studying electric fish interactions of formal approaches inspired by nonlinear dynamics, a powerful theory with widespread practical applications. EODs are periodic so their behaviors, JARs included, embody oscillator interactions. The theory indicates that these, depending on the driver period (relative to the unperturbed driven one) and the coupling strength, can be periodic, quasiperiodic or aperiodic (chaotic). Periodic behaviors, where intervals are invariant and phases locked, have been reported in interacting electric fish (Gottschalk and Scheich, 1979; Westby, 1979; Capurro et al., 1999; Perrone, 2003). We contend that, when performing JARs, fish also embody the quasiperiodic behaviors called 'phase walk-throughs'. Indeed, JARs exhibit the essential characteristics of walk-throughs: namely, the phases (delays) of the driven oscillator move monotonically – walk, sweep, slide – across the driver period, reach a large value, jump to a small value and start the next walk, which, though similar, is not identical to the previous one. Simultaneously, the driven oscillator, mostly periodic, unpredictably destabilizes briefly. Moreover, both walk-throughs and JARs arise when driver period ratios are close to 1:1, 2:1, etc. Walk-throughs, modeled by Ermentraut and Rinzel (1984), appear in interacting fireflies and pacemaker neurons (Segundo, 2003). It is also suggestive that the EODs intervals illustrate a special kind of intermittency. 'Intermittency' is a qualitative concept describing behaviors, most of the time almost periodic, that unexpectedly irregularize briefly in unpredictable ways (Bergé and Dubois, 1988); it has been applied profitably to numerous practical situations. Clearly, the individual EODs with transient interval shortenings behave intermittently (Fig. 1A,B red and others). Further discussion is postponed for a separate publication (A.C. and K.P., manuscript in preparation).

A.C. acknowledges financial support from FAPESP (process number 00/14357-8). A.C. is researcher of PEDECIBA (Uruguay) and thanks the EU Advanced Course in Computational Neuroscience 2001 (Trieste/Italy). Special thanks to Prof. Coraci P. Malta and to the team that provided to us the recording that first motivated the present study: Pablo Errandonea, Dr Ana Silva, MSc Rossana Perrone and Dr Omar Macadar.

## References

**Baker, C. L., Jr** (1980). Jamming avoidance behavior in gymnotoid electric fish with pulse type discharges, sensory encoding for a temporal pattern discrimination. *J. Comp. Physiol*. **136**, 165-181.

**Baker, C. L., Jr** (1981). Sensory control of pacemaker acceleration and deceleration in Gymnotiform electric fish with pulse-type discharges. *J. Comp. Physiol.* **141**, 197-206.

**Bastian, J.** (1986). Electrolocation, behavior, anatomy and physiology. In *Electroreception* (ed. T. H. Bullock and W. Heiligenberg), pp. 577-612. New York: Wiley.

**Bergé, P. and Dubois, M.** (1988). Etude expérimentelle de l'intérmittence et le chaos en convection de Rayleigh-Bénard. In *Le Chaos. Théorie et Expériences* (ed. P. Bergé), pp. 1-83. Paris: Eyrolles.

**Bullock, T. H., Hamstra, R. H. and Scheich, J.** (1972). The jamming avoidance response of high frequency electric fish, I & II. *J. Comp. Physiol.* **77**, 1-48.

**Capurro, A.** (1999). Experimental characterization and development of statistical models of the spontaneous discharge and the jamming avoidance response in the electric fish *Gymnotus carapo*. *Ph.D. Thesis.* PEDECIBA, Montevideo, Uruguay.

**Capurro, A., Macadar, O., Perrone, R. and Pakdaman, K.** (1998). Computational model of the jamming avoidance response in the electric fish *Gymnotus carapo*. *Biosystems* **48**, 21-27.

**Capurro, A., Pakdaman, K., Perrone, R. and Macadar, O.** (1999). Analysis of the jamming avoidance response in the electric fish *Gymnotus carapo*. *Biol. Cybern*. **80**, 269-283.

**Capurro, A., Longtin, A., Bagarinao, E., Sato, S., Macadar, O. and Pakdaman, K.** (2001). Variability of the electric organ discharge interval duration in resting *Gymnotus carapo*. *Biol. Cybern.* **84**, 309-321.

**Capurro, A. and Malta, C. P.** (2004). Noise autocorrelation and jamming avoidance performance in pulse type electric fish. *Bull. Math. Biol.* **66**, 885-905.

**Carr, C. E. and Maler, L.** (1986). Electroreception in Gymnotiform fish, central anatomy and physiology. In *Electroreception* (ed. T. H. Bullock and W. Heiligenberg), pp. 319-373. New York: Wiley.

**Ermentrout, G. and Rinzel, J.** (1984). Beyond a pacemaker's entrainment limit, phase walk-through. *Am. J. Physiol.* **246**, R102-R106.

**Gottschalk, B. and Scheich, H.** (1979). Phase sensitivity and phase coupling, common mechanisms for communication behaviors in gymnotid wave and pulse species. *Behav. Ecol. Sociobiol.* **4**, 395-408.

**Heiligenberg, W.** (1974). Electrolocation and jamming avoidance in a *Hypopygus* (Rhamphichthyidae, Gymnotoidei), an electric fish with pulse-type discharges. *J. Comp. Physiol*. **91**, 223-240.

**Heiligenberg, W.** (1976). Electrolocation and jamming avoidance in the mormyrid fish *Brienomyrus*. *J. Comp. Physiol.* **109**, 357-372.

**Heiligenberg, W.** (1977). Principles of electrolocation and jamming avoidance. In *Studies of Brain Function*, vol. 1 (ed. V. Braitenberg), pp. 1-85. Berlin: Springer-Verlag.

**Heiligenberg, W.** (1986). Jamming avoidance responses. In *Electroreception* (ed. T. H. Bullock and W. Heiligenberg), pp. 613-649. New York: Wiley.

**Heiligenberg, W.** (1991). *Neural Nets in Electric Fish*. Cambridge: MIT Press.

**Heiligenberg, W., Baker, C. and Bastian, J.** (1978). The jamming avoidance response in Gymnotid pulse species, a mechanism to minimize the probability of pulse train coincidence. *J. Comp. Physiol.* **124**, 211-224.

**Hopkins, C. D., Comfort, N. C., Bastian, J. and Bass, A. H.** (1990). Functional analysis of sexual dimorphism in an electric fish, *Hypopomus pinnicaudatus*, Order Gymnotiformes. *Brain Behav. Evol.* **35**, 350-367.

**Kaunzinger, I. and Kramer, B.** (1995). Electrosensory stimulus-intensity thresholds in the weakly electric knifefish *Eigenmannia*, reduced sensitivity at harmonics of its own organ discharge. *J. Exp. Biol.* **198**, 2365-2372.

**Macadar, O., Perrone, R., Capurro, A. and Silva, A.** (2001). Courtship behavior in *Brachyhypopomus pinnicaudatus. Soc. Neurosci. Abstr*. 957.8.

**Metzner, W.** (1999). Neural circuitry for communication and jamming avoidance in Gymnotiform electric fish. *J. Exp. Biol.* **202**, 1365-1375.

**Perrone, R.** (2003). Comportamiento reproductivo en *Brachyhypopomus pinnicaudatus*, Caracterización y correlación entre despliegues locomotores y eléctricos. *M.Sc. Thesis*, PEDECIBA, Montevideo, Uruguay.

**Quintana, L., Perrone, R., Capurro, A., Sierra, F., Blanco, F., Silva, A. and Macadar, O.** (2002). Seasonal and sex differences in locomotor and electric displays in *Brachyhypopomus pinnicaudatus. Soc. Neurosci. Abstr*. 781.16.

**Scheich, H., Gottschalk, B. and Nickel, B.** (1977). The jamming avoidance in *Rhamphichthys rostratus*, an alternative principle of time domain analysis in electric fish. *Exp. Brain Res.* **28**, 229-233.

**Segundo, J. P.** (2003). Nonlinear dynamics of point process systems and data. *Int. J. Bifurcation Chaos* **13**, 2035-2116.

**Silva, A.** (2002). Efectos de la temperatura en Gymnotiformes de la zona templada. *Ph.D. Thesis*, PEDECIBA, Montevideo, Uruguay.

**Watanabe, A. and Takeda, K.** (1963). The change of discharge frequency by A.C. stimulus in a weakly electric fish. *J. Exp. Biol.* **40**, 57-66.

**Westby, G. W. M.** (1975). Has the latency-dependent response of *Gymnotus carapo* to discharge triggered stimuli a bearing on electric fish communication? *J. Comp. Physiol.* **96**, 307-341.

**Westby, G. W. M.** (1979). Electrical communication and jamming avoidance between resting *Gymnotus carapo*. *Behav. Ecol. Sociobiol.* **4**, 381-393.

**Westby, G. W. M.** (1981). Communication and jamming avoidance in electric fish. *Trends Neurosci.* **4**, 205-210.

OPEN ACCESS Freely available online

PLoS one

# Stimulus and Network Dynamics Collide in a Ratiometric Model of the Antennal Lobe Macroglomerular Complex

**Kwok Ying Chong**[¤], **Alberto Capurro, Salah Karout, Timothy Charles Pearce***

Centre for Bioengineering, Department of Engineering, University of Leicester, Leicester, United Kingdom

## Abstract

Time is considered to be an important encoding dimension in olfaction, as neural populations generate odour-specific spatiotemporal responses to constant stimuli. However, during pheromone mediated anemotactic search insects must discriminate specific ratios of blend components from rapidly time varying input. The dynamics intrinsic to olfactory processing and those of naturalistic stimuli can therefore potentially collide, thereby confounding ratiometric information. In this paper we use a computational model of the macroglomerular complex of the insect antennal lobe to study the impact on ratiometric information of this potential collision between network and stimulus dynamics. We show that the model exhibits two different dynamical regimes depending upon the connectivity pattern between inhibitory interneurons (that we refer to as fixed point attractor and limit cycle attractor), which both generate ratio-specific trajectories in the projection neuron output population that are reminiscent of temporal patterning and periodic hyperpolarisation observed in olfactory antennal lobe neurons. We compare the performance of the two corresponding population codes for reporting ratiometric blend information to higher centres of the insect brain. Our key finding is that whilst the dynamically rich limit cycle attractor spatiotemporal code is faster and more efficient in transmitting blend information under certain conditions it is also more prone to interference between network and stimulus dynamics, thus degrading ratiometric information under naturalistic input conditions. Our results suggest that rich intrinsically generated network dynamics can provide a powerful means of encoding multidimensional stimuli with high accuracy and efficiency, but only when isolated from stimulus dynamics. This interference between temporal dynamics of the stimulus and temporal patterns of neural activity constitutes a real challenge that must be successfully solved by the nervous system when faced with naturalistic input.

**Citation:** Chong KY, Capurro A, Karout S, Pearce TC (2012) Stimulus and Network Dynamics Collide in a Ratiometric Model of the Antennal Lobe Macroglomerular Complex. PLoS ONE 7(1): e29602. doi:10.1371/journal.pone.0029602

**Editor:** Thomas Wennekers, The University of Plymouth, United Kingdom

**Received** October 5, 2011; **Accepted** December 1, 2011; **Published** January 10, 2012



**Funding:** This work was supported by EU Framework VI FET Project iCHEM (FP6-032275). http://www2.warwick.ac.uk/fac/sci/eng/eed/research/ichem/. The funders had no role in study design, data collection and analysis, decision to publish, or preparation of the manuscript.

**Competing Interests:** One of the authors (KYC) is employed by a commercial company (The MathWorks Ltd). This does not alter the authors' adherence to all the PLoS ONE policies on sharing data and materials.

* E-mail: t.c.pearce@le.ac.uk

¤ Current address: The MathWorks Ltd., Matrix House, Cambridge Business Park, Cambridge, United Kingdom

## Introduction

The macroglomerular complex (MGC) is a structure within the antennal lobe (AL) of some insect species specialized to process pheromone information. It is composed of a group of specialized glomeruli located where the antennal nerve first enters the AL and is almost entirely functionally separated from the general olfactory system. As such, the MGC can be considered to be an AL in miniature, but with the very specific task of identifying the presence of one behaviourally significant chemical cue: the species-specific pheromone blend [1]. This system is very important for reproduction. During anemotactic orientation for seeking a mate, detecting and identifying the correct ratio of sex pheromone components of a calling female is vital for enabling male moths to fly up the pheromone plume to locate the female [2–4].

Behavioural evidence shows that male moths prefer the full pheromone blend extracted directly from female glands [5]. In wind tunnel experiments, male oriental fruit moths, *Grapholita molesta*, can distinguish between the full pheromone blend and chemical cues composed of incomplete blends of major pheromone component agonists [5]. This moth will usually complete anemotaxis to the source of the full pheromone extract, even when another plume is simultaneously presented composed of an incomplete blend. Also, there are examples of species of moths that live in overlapping habitats that use common pheromone components but do not interbreed because males are attracted only to the conspecific pheromone blend [6].

The olfactory receptor neurons (ORNs) responsible for relaying pheromone information to the MGC are very specifically tuned to individual pheromone components [7]. Each component is detected by just one receptor type that sends convergent axons to the projection neurons (PNs) of just one glomerulus, while the local neurons (LNs) innervate many glomeruli [8,9]. Thus, information regarding each component is integrated in a different glomerulus. This makes the MGC ideal for modelling since it offers a relatively simple system with a specific task.

Electrophysiological studies have found MGC neurons that respond to all pheromone stimuli or selectively to just one pheromone component, or even to a particular blend or ratio [10–14]. For *S. littoralis* in particular, some interneurons responded to one, two, three or all four pheromone compounds, and some just to the mixture of all four indicating that MGC second order neurons are involved in pheromone blend encoding.

The behavioural and electrophysiological studies mentioned above indicate that moths can detect ratios of pheromone blends very precisely. This is a difficult task because it requires the detection of both the individual components and their relative concentrations when presented as a blend varying in time. The optimal solution requires non-overlapping information channels as described in the MGC, and its associated ORN tunings. Since the male moth needs to detect pheromone ratios in odour plumes, the possible conflict between the temporal dynamics of the stimulus with the temporal patterns of neural activity that are used to encode concentration ratios constitutes a real challenge that is successfully solved by the insect in behavioural situations. In this context, we present here a neural network model that is able to encode ratios between the concentrations of two odorants in a blend, and investigate how this goal can be achieved using two types of neural population dynamics that are associated with two different encoding strategies. In particular, we focus on the performance of these two different dynamics to detect concentration ratios when the stimulus pattern displays complex variations in time as happens in odour plumes.

In our computational model [15], the connections are biologically constrained to known morphological details of moth MGC. Two types of dynamics are generated with networks that share the same neural connectivity, except for the LN-to-LN inhibitory connections, that we call fixed point attractor (FPA) and limit cycle attractor (LCA) behaviours, reminiscent of "Winner-Takes-All" and "Winnerless Competition", respectively [16]. FPA networks employ symmetrical inhibition between competitive elements, and the resulting neural network encodes stimulus through the spatial identity of neurons, while LCA networks have asymmetrical inhibition and the output is rich in spatiotemporal dynamics. We compare the ability of the two encoding schemes to represent binary odour ratios and in the process provide insights about certain details of the network connectivity that are still unknown.

## Methods

### Modelling of Neurons

Individual neuron dynamics are modelled using first order differential equation that describes the evolution of the firing-rate activity over time,

$$\tau \frac{da_i}{dt} = -a_i(t) + \mathrm{S}\left(\sum_{j\in \mathrm{P}} w_{i,j} a_j(t) - \sum_{k\in \mathrm{L}} w_{i,k} a_k(t) + R_i(t)\right), \quad (1)$$

where $a_i$ is the activation level of the $i$th interneuron; $\mathbf{P}$ is the subset of neurons that are PNs, and $\mathbf{L}$ the subset of neurons that are LNs; $w_{i,j}$ is the strength of synaptic influence of $j$ on the activity of $i$ (similarly for $w_{i,k}$); $R_i = v_{i,1}r_1 + v_{i,2}r_2 = \mathbf{v}_i \cdot \mathbf{r}$ is the afferent input from receptor neurons to the $i$th interneuron, which is the dot product of glomerular inputs from the two receptor neuron types, $\mathbf{r} = (r_1, r_2)$, weighted by the strength of connections, $\mathbf{v}_i = (v_{i,1}, v_{i,2})$; $\mathbf{S}$ is a sigmoidal squashing function; and $\tau$ (set at 10 ms for all PNs and at 20 ms for all LNs) is the time constant governing the speed of neuronal dynamics. $\mathbf{S}(x) = x^3/(0.5^3 + x^3)$ for $x >= 0$, and $\mathbf{S}(x) = 0$ for $x < 0$, is a rectified sigmoid function that limits the neuronal activity to values between 0 and 1 while still allowing a linear-like response to a range of input levels between non-activation and saturation. Note that synaptic influence from PNs, $j \in \mathbf{P}$, is excitatory and therefore positive, while LNs, $k \in \mathbf{L}$, are inhibitory and negative. More details for the determination of the connection weights $w_{i,j}$ and $w_{i,k}$ are given in the next section. Simulations were carried out on a PC running MATLAB using customized code. The evolution of the neuronal firing-rates over time was calculated using integration by a Runge-Kutta algorithm with fixed time-steps of 1 ms. A Gaussian noise $\xi$ ($\mu = 0$, $\sigma = 5 \times 10–4$) was added to this equation at each time-step to create non-deterministic firing-rates. The value of $\sigma$ was chosen such that the neuronal activity was not completely dominated by noise, but still generated variability between repetitions to allow a comparison of the robustness to noise between different instances of the model.

The initial activation values were taken from a Gaussian random distribution with $\mu = 0.01$ and $\sigma = 0.0025$. In both LCA and FPA models, the values of $a_i$ rapidly converged to an equilibrium point that was zero in the absence of stimulation (i.e., there was no spontaneous activity). We waited 100 ms from the start of the simulation until the stimulus onset to ensure that the initial conditions did not influence the comparison between both dynamics (FPA and LCA).

### Network Connectivity

The general connectivity of the network (Figure 1) was set according to morphological studies of the moth MGC [8,9,13,17–21]. The number of MGC glomeruli equals the number of behaviourally relevant pheromone components, with each ORN type projecting to one MGC glomerulus [21]. This number can typically range between 1 and 8, depending on the species of moth. Since the encoding of blend ratio is investigated here, a two-component pheromone blend and, accordingly, two glomeruli are simulated.

The number of PNs and LNs has large variation in different species of moth. In *Manduca sexta* there are 35–40 PNs in the MCG, and the total number of LNs is 360 in the whole AL (Table 1 in [17]). From this number of LNs the proportion that belongs to the MGC is undetermined, but it is likely to be only a minor fraction because most glomeruli are part of the general olfaction system. In this context, we decided to use 30 PNs (divided in 2 glomeruli) and 30 multiglomerular LNs as a plausible approximation that allows a rich dynamic behaviour in our model network.

In the moth MGC, pheromone sensitive ORNs are specifically tuned to just one pheromone component and relay information to the PNs of one particular glomerulus [9], while the connectivity within PNs is mostly uniglomerular [19]. The input to each glomerulus was taken to be the aggregated activity of ORNs activated by the respective pheromone component, represented by a scalar value within a two element vector $(r_1, r_2)$. Therefore, each PN in the model receives input from just one receptor type (either $v_{i,1}$ or $v_{i,2} = 0$, for all $i \in \mathbf{P}$) via a randomly weighted connection (in order to give most PNs direct afferent excitation, weights were drawn from a normal distribution, $\mu = 1$, $\sigma = 1$, with negative values rectified to 0), and has random excitatory interconnections with other PNs of the same glomerulus. PNs have 0.8 probability of synapsing to another PN within a glomerulus, with a relatively small connection weight of $0.0125 \pm 0.1$ (negative values were rectified to 0). These values have been chosen so as to not cause runaway excitation (PN trajectories showed little change for weight values between 0 and 0.4 in FPA and from 0 to 1.6 in LCA).

In contrast to PNs, the LNs of the moth MGC are generally multiglomerular and receive input from many types of pheromone sensitive ORNs [13]. Therefore, in the model LNs receive input from both receptor types, so receiving information for both pheromone components. The connection probability was set to 1.0, with weights drawn from a normal distribution, $\mu = 1$, $\sigma = 1$, with negative values rectified to 0.

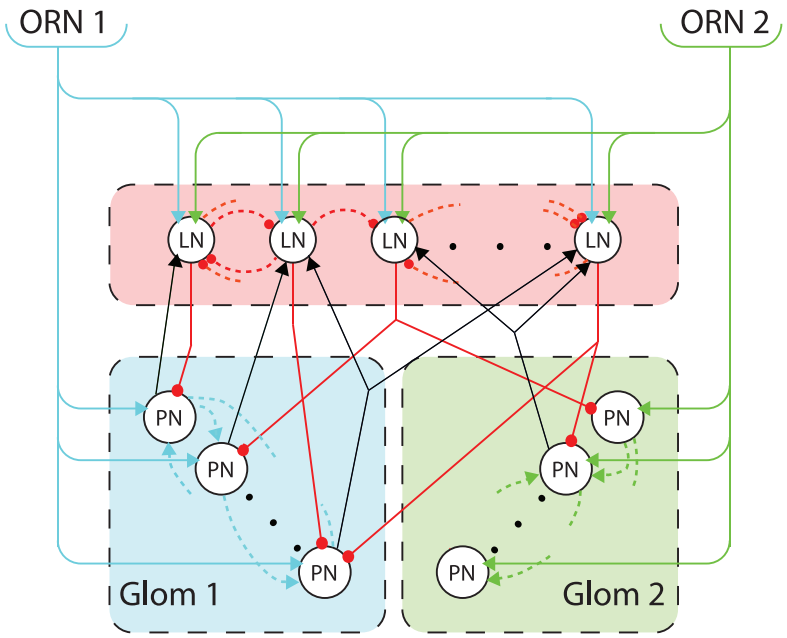


**Figure 1. Neuronal connectivity schematic.** Excitatory connections are represented with arrows and inhibitory connections with circles. Just two glomeruli are modelled, which are the convergent sites for axons of two ORN types (cyan for ORN1 and light green for ORN2). The receptor neurons provide afferent excitation to both classes of AL neurons. PNs, being exclusively uniglomerular, receive excitation from just one type of receptor, while LNs, being multiglomerular, receive excitation from multiple receptor types. LNs and PNs have mutual random connections (red and black solid lines – see Methods). PNs innervating a single glomerulus form random excitatory interconnections with fixed probability (dashed lines – see Methods). Two cases of inhibitory LN interconnectivity are considered: random connections of fixed probability to produce LCA behaviour (as in the example shown here) and all-to-all connectivity generating FPA behaviour (not shown).
doi:10.1371/journal.pone.0029602.g001

As output and input synapses have been identified between LNs and PNs in many species [13], these contacts were included in our model. Inhibitory connections from the LNs to the PNs were chosen randomly. A LN had a probability of 0.2 to connect to any PN, irrespective of the glomerulus to which the PN is associated, and a high strength weighting for that connection ($-2.5 \pm 0.1$). The high strength of connection ensured that any post-synaptic PN would be completely inhibited, and as such, any value smaller than $-1$ would suffice. Relatively sparse connectivity from LNs to PNs was required to ensure that not all PNs were completely inhibited during odour presentation. Although the exact value was not important, 0.2 provided a balance that allowed LNs to influence but not overwhelm PN response. We also included excitatory feedback from PNs to LNs with a connection probability of 0.5, and synaptic weight set to $0.033 \pm 0.1$ (negative values were rectified to 0).

FPA network and LCA network models differed by how interconnections between LNs were determined. For FPA networks, competition between cells was created through mutual inhibition, so LNs were given all-to-all connections with a high inhibitory connection strength ($-15 \pm 0.1$). For LCA networks, cells were connected asymmetrically with high inhibitory connection strength ($-15 \pm 0.1$), leading to uneven competition that prevents a long-term winner, and therefore prevents a stable equilibrium point. To generate this asymmetry, connections between LNs were chosen randomly with a probability of 0.25 for any LN connecting to any other. For this value, the subnetworks of LNs generate switching behaviour. Indeed, any value between 0.2 and 0.4 could also generate switching behaviour. However, for values less than this the subnetworks would lack LN interactions, and for values greater, subnetworks would become largely symmetrical. In either case switching behaviour would not occur.

In FPA models, for each LN that contacts another there exists a reciprocal connection (with both synaptic weights being drawn from the same random distribution), so the coupling must be symmetric. When the connection probability turns lower (e.g., 0.25 in LCA), it becomes very probable that if a given LN contacts another the opposite may not be true, giving rise to an asymmetric connectivity pattern in the LN subnetwork.

20 realizations of each network type (LCA and FPA) were created following the above rules so as to investigate the general properties of the model and the effects of the noise level. The connectivity is summarized in Figure 1.

## Results

### Network Behaviours

The behaviours of the MGC models created are illustrated by an example response of a FPA network, and one of a LCA network (left and right panels in Figure 2a, respectively). The LNs in the FPA network compete directly with one another through the all-to-all inhibitory connectivity. The random ORN to LN connectivity determines that for any ratio there is one LN that receives greater excitation, and inhibits its competitors becoming dominant. In the left panel of Figure 2a, this FPA competition can be seen in the LN responses: after a short initial transient only one LN remains active, and the network settles into a stable spatial pattern of activity. This is also reflected in the PN responses, showing a very brief activity transient immediately after stimulus onset until a stable pattern is established. In contrast, the LNs in the LCA network do not settle to a stable spatial pattern within the time period considered (500 ms), but change continuously, driving the PN activity to do the same. This results in a sequence of PN activation patterns comprising rich spatiotemporal dynamics (right

panel in Figure 2a). We investigated the evolution of these complex dynamics for longer stimulus durations (5 seconds) and found that the network typically reaches a fixed point (Figure S1) or a periodic orbit (not shown) after 0.5 to 1 second of simulation. This later fixed point includes many LNs active at the same time, in contrast with the earlier fixed point of the FPA network (Figure 2a) in which only a single LN remains active. As pheromone information in natural odour plumes is presented in pulses of short duration, this fixed point is unlikely to be reached in the moth during behaviuoral situations. For this reason we kept the term LCA, as it refers to the dynamics observed during the stimulus period used in our simulations (500 ms). However, this issue is interesting from a theoretical point of view in the comparison between LCA and "Winerless Competition" types of neuronal dynamics because this late fixed point is not reached in the last case, although it was observed in electrophysiological recordings performed in the locust AL [22] (see Discussion).

The transient PN responses can also be seen in the trajectory plots depicted in the lower panels of Figure 2. The FPA model responses (left panel in Figure 2b) show fast onset transients that lead to stable attractors at a given instant. The system stays near these stable attractors until the return transients after stimulation. The LCA model (right panel in Figure 2b) also displays fast transients from rest at stimulus onset, and then enters into complex spatio-temporal patterns which are both sensitive to the input ratio and repeatable over trials perturbed with different realizations of noise.

The trajectories show how the responses differ across input ratios in each network (lower panels of Figure 2). In both networks, the PN population responses to different ratios are separated. In the FPA model, trajectories never cross for different ratios during the transient phase or as these approach the fixed point. The separation of the fixed points for different ratios indicate reliable encoding of the blend ratios considered over time. In the LCA model, the trajectories are shown to be localized in different regions of the PN phase space that do not overlap. In both networks, the trajectories also show that responses that are closest together are induced by neighbouring ratios, suggesting that the response trajectories and their associated attractors vary smoothly and continuously with changes in the input ratio.

## Conflict between Stimulus Dynamics and Network Dynamics

An issue with using time as an encoding dimension for odour quality is that this temporally structured code may become confounded with the dynamics of the stimulus. This is especially problematic for animals such as the moth that perform anemotactic orientation in odour plumes, where the stimulus dynamics can be very complex and have been shown to be behaviourally relevant [23,24].

Both FPA and LCA models can preserve and accurately pass on the stimulus dynamics to downstream neural processes, as illustrated in Figure 3. The smallest pulse in Figure 3 is around 40 ms, which is realistic for odour plumes [24]. However, we wondered if the stimulus dynamics reflected in the activity of the PN population could interfere with the encoding of the blend ratio. To assess this issue, we correlated the spatiotemporal output patterns of the PN population for a single stimulus pulse of long duration with the patterns obtained from stimulation with differently timed pulses. This result is presented in the next section for both the FPA and LCA models. The spatiotemporal output was taken to be the activity of the PNs partitioned into time-bins. The mean activity for each PN was found over each time-bin, $\Delta t = t_j - t_{j-1} = 10$ ms, for each time-step $j$. This produced a matrix, $A_{ij}$, composed of a time series of activity for each PN, $i \in \mathbf{P}$:

$$A_{ij} = \frac{1}{\Delta t}\int_{t_{j-1}}^{t_j} a_i(t)dt. \quad (2)$$

**Correlating PN Population Responses.** To assess the evolution of the PN code over time and its dependence upon the stimulus, the matrix of spatiotemporal responses to a 500 ms duration stimulus, $A_{ij}$, was broken into a set of column vectors $A_j$, each describing the instantaneous spatial activation pattern of the PNs at the $j$th time-bin. This process was repeated for the PN responses to a differently timed pulsed stimulus, generating the set of vectors $A'_j$. The similarity between PN responses for the two different stimuli and at different times $j_1$ and $j_2$ was measured using the correlation coefficient between response vectors defined as

$$c = \frac{A_{j1}^T A'_{j2}}{\left[A_{j1}^T A_{j1} . A_{j2}'^T A'_{j2}\right]^{1/2}}. \quad (3)$$

In this way, we assessed the effect of inter-pulse intervals on the correlation (Figure 4).

The different network behaviours are clearly evident in the cross correlation diagrams. The stable spatial patterns of the FPA models result in high correlation coefficients between all time-steps for the 500 ms single pulse (Figure 4a). The large square region of almost perfect correlation shows that the network dynamics were relatively consistent over time. The transients leading to the stable attractor can be seen as a small region of high correlation on the diagonal immediately after stimulus onset. In contrast, the temporally rich behaviour of the LCA models results in relatively low correlation except for a narrow band on the upward diagonal (Figure 4e). This narrow diagonal shows that the changes in spatial patterns happen smoothly but quickly, with the width being no greater than 50 ms, as the spatial pattern must be switching within this time.

When 10 ms inter-stimulus intervals are introduced to break up the single long pulse, in both the FPA and LCA models (Figure 4b and f), the systems begin to return to rest at each interval, but these return transients have not enough time to get established. Thus, the progression of responses is temporarily halted at each interval, but then resumes at the onset of the next pulse.

Longer inter-stimulus intervals of 100 ms (Figure 4d and h) allows enough time for these networks to fully reset and start responses afresh, and so each pulse produces the same initial spatiotemporal response. For FPA models, there is still the block of high correlation for each pulse (Figure 4d), and for LCA models, there is the same diagonal for each pulse (Figure 4h). For both networks, the correlation pattern during the pulse is the same as the first 50 ms of the 500 ms pulse. In the next 50 ms after each pulse, the correlation pattern does not change significantly from that at stimulus offset. This indicates that the spatial response pattern does not change during the return transients. However, it decreases in strength until fading away due to the decorrelation introduced by the noise in the firing-rate.

In the case of 50 ms inter-stimulus intervals, this intermediate time length allows overlap between the return transients after each pulse and the initializing transients of the next pulse (Figure 4c and g). Given the simple temporal structure of the

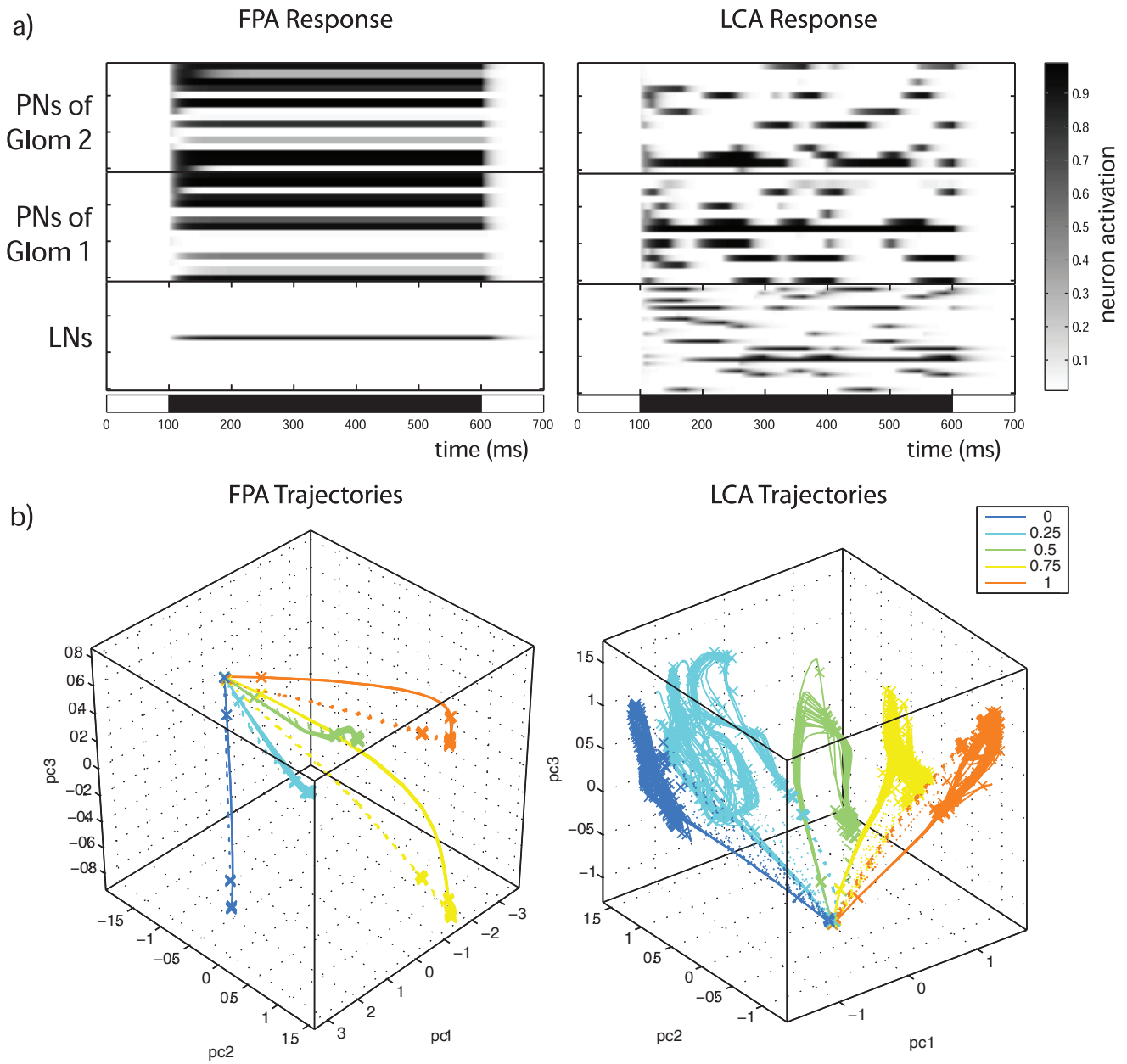


**Figure 2. Examples of modelled responses.** a) These two panels show examples of the response to stimulation from a FPA network (left) and a LCA network (right). The bar in the horizontal abscissa indicates stimulus duration and timing. For illustrative purposes, a 0.5:0.5 ratio stimulus was used. In the sub-panels, the rows are the activity for each neuron. The top two sub-panels show PN activity in the two glomeruli, while the bottom sub-panel shows LN activity. The FPA model displays transient activity patterns before settling to a stable spatial pattern around 100 ms after stimulus onset, whereas the LCA model displays rich temporal patterning during the stimulus period. b) Trajectories of the PN responses to different input ratios for the same model realizations displayed in the rasters above, each with 20 repeats perturbed with different realizations of Gaussian white noise of $\mu = 0$ and $\sigma = 5 \times 10{-}4$. The first three principal components have been taken to produce 3-dimensional plots so that a point in these plots represents a spatial response pattern at an instant in time (bin size was 5 ms). Solid lines indicate the trajectories during stimulation, while dotted lines indicate return trajectories after stimulation. The crosses are plotted at regular time intervals of 50 ms, and thus indicate the local velocity of the trajectories and its variability between trials. The different network behaviours are also apparent in these plots. The time in which the mean Euclidean distance between the trajectories reaches a maximum value is $358 \pm 198$ ms for FPA, and $226 \pm 143$ ms for LCA ($\mu \pm \sigma$ for 20 model realizations, $p = 0.02$ in the t-test).
doi:10.1371/journal.pone.0029602.g002

responses in the FPA models, the high correlation for each pulse is re-stablished, as happened for the 100 ms interval pulses (Figure 4c). However for LCA networks, 50 ms intervals do not allow a full reset in the dynamics as for longer intervals, nor a continuation of the temporal sequence as for shorter intervals (Figure 4g). Instead, except for the first 20 ms after stimulus onset, the spatial patterns appear to be altered and are no longer correlated with spatiotemporal response for the 500 ms pulse. This has a profound effect on the encoding of ratio identity by the spatiotemporal PN responses when the network is exposed to stimulus dynamics on certain time scales, as we show in the next section.

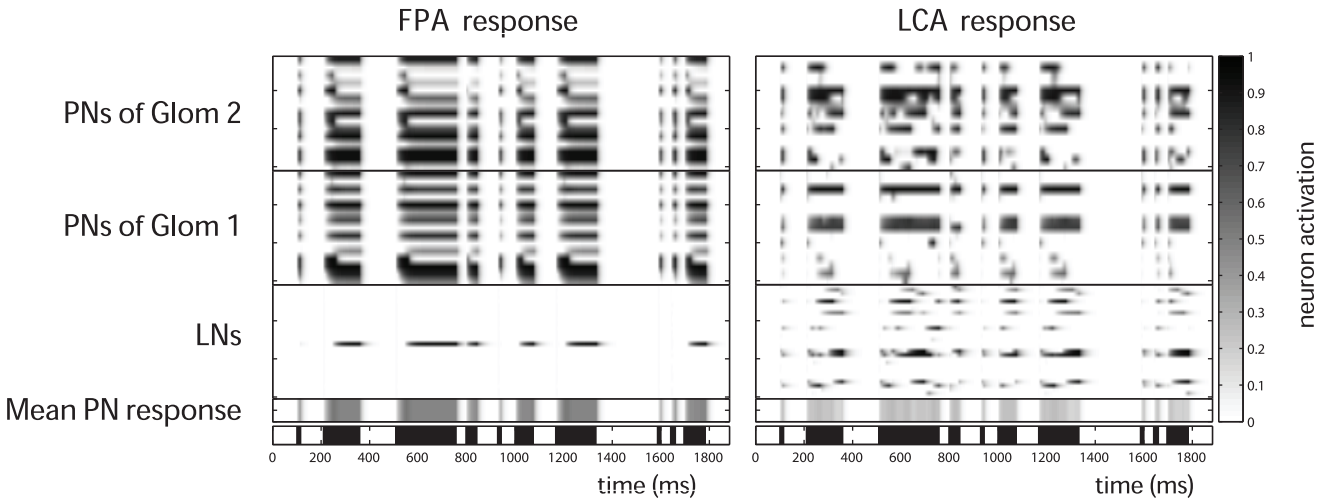


**Figure 3. Responses to randomly timed stimulus pulses.** Responses to randomly timed stimulus pulses. The FPA network (left) and the LCA network (right) were presented with the same randomly timed stimulus. Both models were able to follow the odour pulses, and at each onset of stimulus, the initial transients governed by networks dynamics appear to start anew. The averaged PN activity shows that both models follow the odour pulses closely and this averaged activity accurately relays the timing information of the stimulus.
doi:10.1371/journal.pone.0029602.g003

**Identifying Ratios from PN Responses.** In order to investigate how well FPA and LCA models encode odour ratios, we assessed the separability of the spatiotemporal outputs between ratios, and its robustness to noise. This was done by discriminant analysis, to quantify how well the input ratio could be identified from the PN responses. Stimuli were created by randomly selecting ratios from a uniform distribution. They were categorized into five ratio groups 0:1, 0.25:0.75, 0.5:0.5, 0.75:0.25, 1:0 corresponding to $\mathcal{R} = 0, 0.25, 0.5, 0.75, 1\ (\pm 0.125)$ respectively. More formally, for a ratio $r_1{:}r_2$, $\mathcal{R} = r_1/(r_1 + r_2)$.

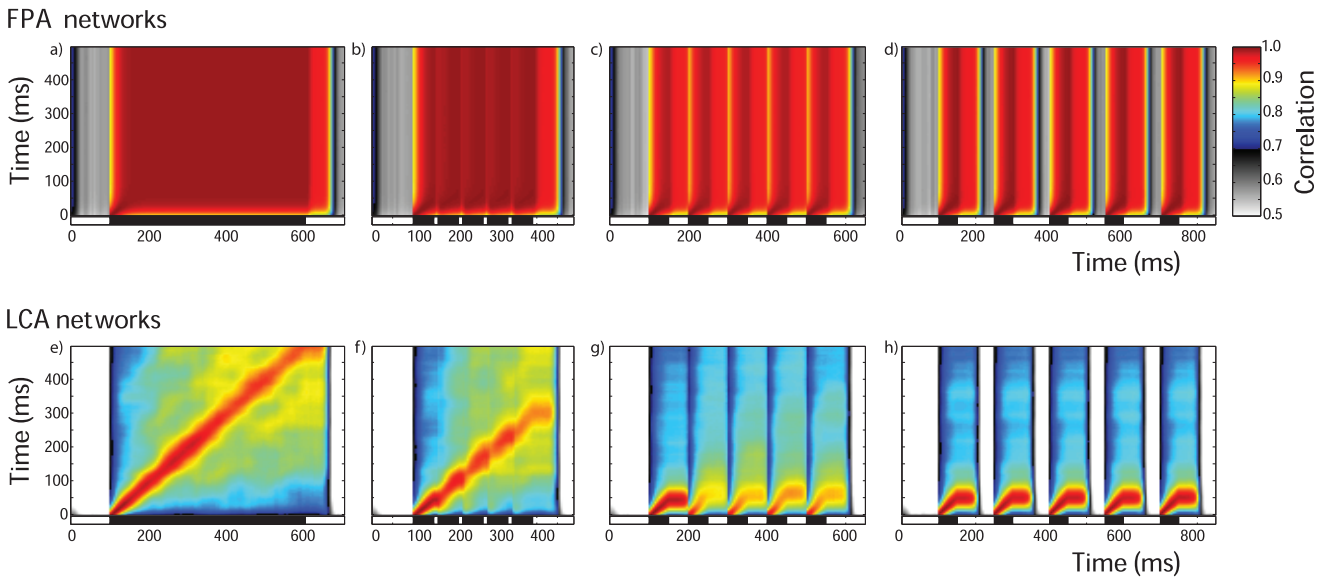


**Figure 4. Cross correlation and stimulus timing.** Cross correlation and stimulus timing. Time-binning the PN population responses results in a series of instantaneous spatial activity patterns. The spatial activity patterns for a 500 ms duration stimulus (vertical axis) were correlated with the spatial patterns from differently timed pulsed stimuli (indicated by bars on horizontal abscissas). This was done for FPA networks (a–d) as well as for LCA networks (e–h). The pulse patterns are: a) one 500 ms pulse and; b) five 50 ms pulses with inter-stimulus intervals of 10 ms, c) 50 ms and d) 100 ms. The same patterns were used for LCA (e–h). The correlation coefficients shown are mean values taken from 400 random input ratios and 20 networks. The different network behaviours between FPA and LCA networks result in very different looking cross correlation maps for the 500 ms pulse results (a and e). FPA networks show high correlation throughout periods of stimulation, indicating that the spatial patterns are very similar across time-bins (a). LCA networks display lower correlations, with highest values in a thin region along the diagonal (e). For both FPA and LCA networks, very short inter-stimulus intervals of 10 ms have little effect except to slow the progression of the sequence of spatial patterns (b and f). The pulses with long inter-stimulus intervals of 100 ms do not interfere, and each pulse elicits a separated response that is almost identical to each other pulse (d and h). However, for 50 ms inter-stimulus intervals, the tail of the previous pulse overlaps with the next response (c and g). This has no apparent effect on FPA models, but LCA models show a marked difference in the shape of pattern of correlation for pulses following the first.
doi:10.1371/journal.pone.0029602.g004

In the same way as for correlation analyses, the spatiotemporal output was taken to be the time-binned PN responses. Thus, for each odour presentation, a time series of instantaneous PN activity patterns was constructed. A 500 ms pulse was used to generate a training set of 100 stimuli, which gave 100 instantaneous PN responses for each time-step. These time-steps were set on the vertical axis of the plots in Figure 5. Then, the time steps of a data set composed of 400 stimulations were placed on the horizontal axis and classified using discriminant analysis. In this way, we can visualize the times at which the data set is coherent with the training set and therefore allow correct classification. The colour code represents success rate of ratio blends correctly classified.

As part of the discriminant analysis algorithm, the covariance matrix of the variables has to be inverted. In this situation, redundant linearly dependent dimensions of the training set can cause failures in the calculations. To avoid this problem, principal component analysis (PCA) was applied beforehand to retain only the principal dimensions reflecting 90% of variance before classification was attempted.

Figure 5 confirms the underlying behaviours of the FPA and LCA models observed in Figure 4. FPA models show a large square region of almost perfect classification from 50 ms after stimulus onset to the stimulus end in both axes (Figure 5a). This is indicative of the constant spatial code generated by the stable attractor that the FPA networks attain after initial transients. The transients leading to the stable attractor are evident in the line of high classification rates along the diagonal in the first 50 ms after stimulus onset.

LCA models show a narrow band where the accuracy is greater than 90% (Figure 5e). The narrow width indicates the fast switching behaviour of the spatiotemporal PN code. This diagonal is pronounced for the whole stimulus duration in this analysis, showing that the temporal code spans the whole stimulation. There are also elevated success rates that are off of the diagonals during the last half of the stimulation. This is evidence of the LCA models entering limit cycles, repeating spatiotemporal output. However, these regions do not seem well defined since the properties of these limit cycles are different for each model instantiation and stimulus ratio. These features were also evident in the correlation analysis, but the colour scale of the diagram made it more difficult to visualize, and also the correlation analysis was more affected by the variability of the neural activity, which accumulates over time, gradually weakening the correlation.

The effect of short 10 ms intervals can be seen to momentarily halt the progression of the response dynamics, which resume at the next pulse (Figure 5b and f). During these intervals the drop in classification rates can be seen clearly. The 100 ms intervals provide enough separation for each pulse to start a completely new response for both FPA and LCA models (Figure 5d and h). The most interesting case of the intermediate length 50 ms intervals shows that FPA responses allow classification in each pulse just as if they were presented individually (Figure 5c). However, LCA models suffer a big drop in classification accuracy as the tail of responses to the first pulse is confounded with the spatiotemporal responses of subsequent pulses (Figure 5g). This shows that the spatiotemporal encoding scheme cannot reliably convey odour identity for certain dynamical stimuli, specifically when the stimulus dynamics are on a similar time scale thus interfering with the intrinsic dynamics of the LCA network.

## Time as an Encoding Dimension

**Measure of Ratio Specificity.** The advantage of using time as an extra encoding dimension is that, theoretically, it can greatly

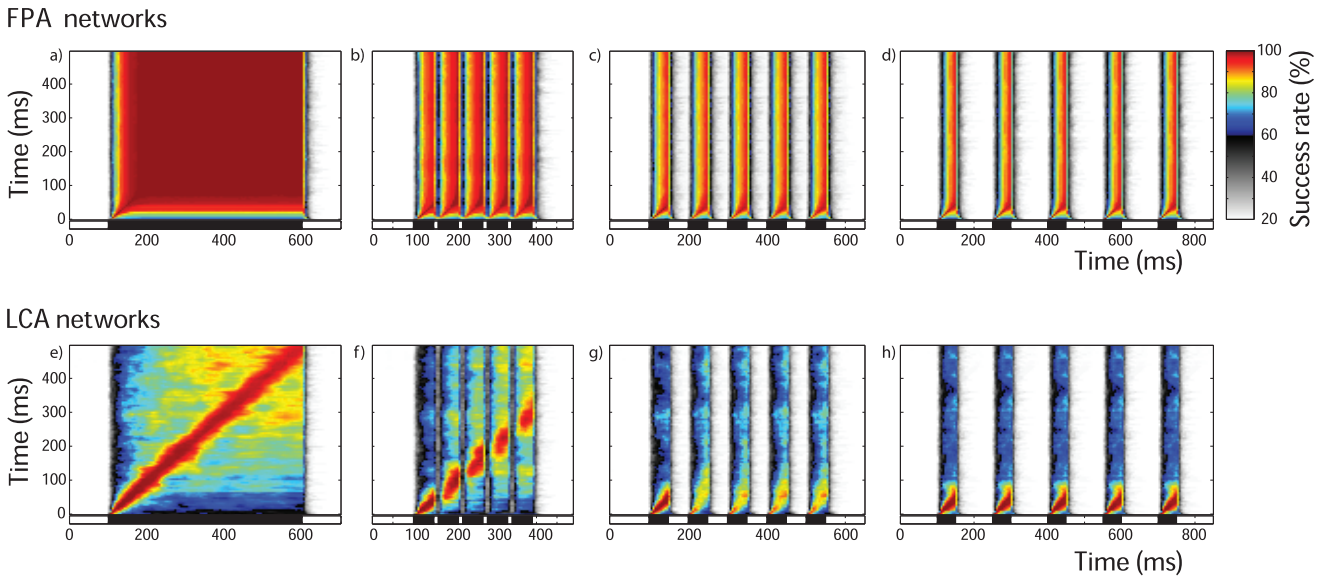


**Figure 5. Cross classification and stimulus timing.** Again, we use the series of instantaneous spatial patterns as in Figure 4. FPA (a–d) and LCA (e–h) networks were repeatedly stimulated with 500 ms pulses of five different ratios. The subsequent PN spatial patterns for each time-bin were used to train a linear model. The networks were also stimulated with the differently timed pulses of the same 5 ratios, generating spatial patterns which were then classified by the linear model, estimating which ratios generated each spatial pattern (see methods). The colour scale is the same for all panels, and shows the mean success rate for multiple trials and networks. 20% is the chance success rate. For the single pulse of 500 ms, there is high accuracy along the diagonal for both FPA and LCA networks (a and e). LCA networks have a thin region around the diagonal of high accuracy (e), indicating a smooth transition between spatial patterns, which are constantly switching. FPA networks simply show a block of high accuracy (a), indicating that the spatial patterns change very slowly or not at all. The dynamics is not affected for inter pulse intervals of 10 ms (b and f) and 100 ms (d and h). For inter pulse intervals of 50 ms, LCA models suffer a big drop in classification accuracy as the tail of responses to the first pulse is confounded with the spatiotemporal responses of subsequent pulses (g), while FPA responses allow classification in each pulse just as if they were presented individually (c).
doi:10.1371/journal.pone.0029602.g005

increase the potential encoding space available. No longer is the information confined to just a static spatial activity pattern, but can entail a sequence of spatial patterns, multiplying the possible representations with each time step. Here, we compare the spatiotemporal PN codes for the FPA and LCA models to investigate if the more temporally complex output of LCA models utilizes this advantage.

In this section, analyses are performed on the spatiotemporal code including time, not just instantaneous 'snapshots' as before. Here, the response to stimulation is taken to be a vector produced by all the elements of the matrix $A_{ij}$ (as defined by equation 2), giving

$$(A_{11},A_{12},...,A_{1m},A_{21},...,A_{nm}),$$

if $A_{ij}$ is an $n \times m$ matrix. This makes a vector space with a dimension for each time-step for each PN.

When the response to one input ratio is correlated with other ratios, the closest ratios have highly correlating neuron responses while very different ratios have low correlating responses. This creates a bell-shaped curve (Figure 6a). We use the second moment about the peak correlation as a measure for the width of this bell-shaped curve, and thus the specificity of the PN code. Let the input ratio be denoted by the proportion of the input composed of type 1 receptor input, $\mathcal{R}=r_1/(r_1+r_2)$, then the curve width, $\sigma_{\mathcal{R}_\mu}$, for a particular ratio, $\mathcal{R}_\mu$, is defined to be

$$\sigma^2_{\mathcal{R}_\mu} = \int_p^q (\mathcal{R}-\mathcal{R}_\mu)^2 . c(\mathcal{R}_\mu,\mathcal{R}) . d\mathcal{R}, \qquad (4)$$

where $p=\mathcal{R}_\mu$ and $q=\mathcal{R}_\mu+0.5$ for $0<\mathcal{R}_\mu\leq 0.5$, and $p=\mathcal{R}_\mu-0.5$ and $q=\mathcal{R}_\mu$ for $0.5<\mathcal{R}_\mu\leq 1$ in order to avoid problems at the boundaries of $\mathcal{R}$. $c(\mathcal{R}_\mu,\mathcal{R})$ is the correlation coefficient for the spatiotemporal responses to the two ratios. The average width for a network was taken to be the mean width over ratios.

This bell-curve width is indicative of the specificity of the PN output to ratios. Since the correlation between the spatiotemporal output to different stimuli gives a measure for the similarity of the these outputs, a narrow bell-curve would be produced by a spatiotemporal code that changes greatly across ratios. The sharper the bell-curve, the better the differentiation can be of the input ratios from the spatiotemporal output. This measure for ratio specificity was used to assess the importance of time to FPA and LCA models. The time-length from stimulus onset of the spatiotemporal PN responses was changed, and the analyses were carried out for each time-length. In this way, we tested the effect of the time-length of the code on the ability of PN population responses to encode ratios.

The temporal consistency of the PN responses from FPA models determines that the ratio specificity is not enhanced by taking longer time-lengths of PN responses. The fixed spatial response patterns do not allow any more information to be conveyed once the transient patterns have completed. Therefore for FPA models, one would not expect that ratio specificity is dependent on code length once the stable attractor has been reached, and this is indeed the case (Figure 6b). Interestingly however, specificity is not dependent on code length, except for the first 10 ms transient phase before a stable spatial pattern is fully established, as depicted in Figure 6b by a horizontal plot for code lengths of over 50 ms.

In contrast, LCA models have much improved ratio specificity as time allowed for encoding is increased. The largest drop in bell-curve width is within the first 200 ms, after which the rate of change is reduced, and a stable value is reached by 500 ms (Figure 6b). This drop in bell-curve width corresponding to an increase in ratio specificity of the PN code demonstrates that the spatiotemporal activity of PN responses in LCA models does indeed utilize time as a coding dimension. Part of this effect can be related to the fact that PN responses are sparser because they receive larger inhibition from the LN population, which is more active due to a lesser degree of inhibitory self coupling.

In summary, our results suggest that a spatiotemporal code can and does carry more information than spatial-only code, allowing a more precise determination of the input ratio over time.

**Response Length and Reliability.** In this final section, we take the idea of the spatiotemporal code over limited time-lengths presented in Figure 6a, and apply it to the training and data set responses used in Figure 5. Then, we perform the discriminant analysis on this spatiotemporal output (Figure 6c). Surprisingly, the FPA models display a strong time dependence for classification

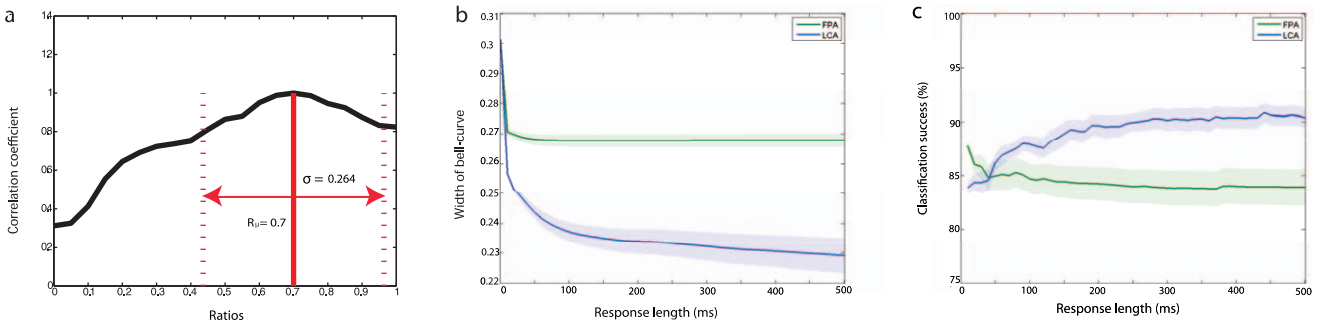


**Figure 6. Ratio specificity, output reliability and code length.** a) An example illustrating the bell-shaped correlation curve. Correlating the PN population response for a particular ratio, $\mathcal{R}_\mu$, against all other ratios gives this approximately bell-shaped curve, which peaks at $\mathcal{R}_\mu$ with a correlation coefficient of value 1. The more specific the PN response to a ratio, the sharper and thinner the bell-shaped curve. Thus, the width of the bell-curve, $\sigma$, marked by the dotted lines (see text for definition) indicates the specificity of the PN response. b) The effect of response length on code specificity. This shows the specificity of the spatiotemporal PN responses as the response length taken into account is changed, indicating how the ability of the models to encode ratios is dependent on the temporal dynamics. The shaded areas show standard error. c) The effect of response length on reliability. Discriminant analysis was used to predict the input ratios from PN responses according a training set of responses (see text). The accuracy of this classification indicates the reliability of the PN responses for the identification of input ratios. This test was applied to different response lengths as in b). The accuracy of both types of networks becomes stable by 100 ms, with FPA networks at around 85% and LCA networks at around 91%. LCA networks start with lower accuracy but quickly increase and exceed that of FPA networks. The FPA networks' ability to hold ratio information actually decreases as they reach the stable attractors. Again, shaded areas represent the standard error.
doi:10.1371/journal.pone.0029602.g006

accuracy for the first 100 ms period after stimulus onset. Moreover, the accuracy largely decreases as code length initially increases. This is because the FPA network has a limited number of discrete attractors, so the encoding space is smaller for the stable patterns than during the transient phase before neural activity has saturated.

LCA models behave more intuitively, with accuracy increasing during the transient phase, and plateauing around 100 ms with better accuracy than the best that FPA models achieve during stimulation. Classification accuracy is dependent on the consistency of the PN responses as well as on the separability between responses to different input ratios. The PN output of LCA models have increasing separability for the first 100 ms since the ratio specificity increases (Figure 6b).

## Discussion

In the present article we presented a neuronal model constructed with a connectivity pattern based on the morphology of the moth MGC, and showed how this model is able to encode ratios between odour concentrations in a binary blend. We aim to contribute to the ongoing discussion about spatial and temporal coding strategies in the insect AL. The two different dynamical regimes FPA and LCA were generated without using any special intrinsic neuron properties (all neurons were first-order linear equations except for the addition of a sigmoidal squashing function), so that as few as possible assumptions were made and we can be sure that they arise as a purely network phenomena, due entirely to the way in which LN inhibitory interconnections were chosen. Using this simple modelling approach, we intend to gain insight into MGC working principles rather than provide an extensive recreation of its physiology in a particular species, because the two types of dynamics explored here may be operative to a certain degree in very different invertebrate nervous systems.

The connectivity of our model was based on morphological studies of the moth, principally *Manduca sexta* [8,9,13,17–21,25] To keep the network patterns as simple as possible, we did not include some features that were described in other insects but not confirmed in the moth, such as the existence of excitatory LNs [26] or feedback from LNs to ORNs [27]. Similarly, the dynamics of the receptors (e.g., [28]) were omitted in order to focus on the ratio encoding capabilities of the MGC circuitry.

From the previous efforts to model different aspects of the AL, only a handful have been specific to the MGC [29–36]. Linster *et al.* (1994) describes an oscillatory model, showing that by balancing numbers of inhibitory and excitatory neurons in a network receiving two component input, a system can oscillate when a particular ratio is presented. Linster *et al.* (1996) built a more biologically constrained model including LNs that mediate information to PNs. Again, the balance between inhibitory and excitatory elements is investigated, this time to show that PN response patterns can be made dependent on the input ratio. The model can be tuned such that PNs will display both inhibitory and excitatory influences from the LNs when a particular ratio is presented. As such, model PNs will respond with a pattern of activation, which includes mixed periods of excitation and inhibition, only for input that is close to a particular ratio. The recent article of Zavada *et al.* [36] presents minimalistic feed-forward networks displaying "Winner-Takes-All" type of competition between LNs in the MGC of the moth. These models are based on specific connection strength ratios between ORNs and LNs that allow the recognition of pheromone component ratios across a wide range of concentrations.

In some studies that model the MGC, and those that model the AL for general olfaction, focus has been on generating biologically realistic PN response patterns. Highly-detailed neurons exhibiting bursting behaviour have been used within different neuronal circuits of four-or-less interneurons [29–31]. It was shown that these circuits can be designed such that the model PNs display excitation or inhibition depending on which components are present in a simulated pheromone blend input. This replicated some responses observed in the activity of PNs in the Sphinx moth, *Manduca sexta*, when pheromone components were presented [11,12].

From a theoretical point of view, the issue of excitatory-inhibitory synaptic balance has been addressed in [37], analysing the conditions to have reproducible encoding in "Winnerless Competition" dynamics, which is comparable to LCA. Concerning the FPA dynamics, an AL model of this type has been used for identification of real mixture data using an artificial sensor array to address classification methods and working memory in insect olfactory systems [38,39].

The existence of a population code in which odours are represented as spatial activation patterns that evolve in time has been extensively described in insects using functional imaging methods, e.g., [9,40]. On the other hand, both LCA networks and the theoretical framework of "Winnerless Competition" proposed by Laurent's group and collaborators [16,22,41–44] produce orbits in the PN phase space as a suitable principle by which odour identity and concentration can be represented. In the case of "Winnerless Competition", the trajectories are defined by sequences of unstable attractors, each corresponding to the transient activation of a specific subset of synchronized PNs. They share the property of being robust against perturbations and, at the same time, very sensitive to the input. There exists considerable evidence that this type of sensory encoding is used in the locust AL [22,45], and may also constitute a general principle of perceptual representation of multi-dimensional signals widely extended across species and sensory modalities [46,47]. Our LCA networks show similar sensitivity to the input whilst also being robust to perturbations, although they do not depend upon heteroclinic dynamics.

The facts outlined in the previous paragraph highlight that both spatial and spatiotemporal codes can carry information about odour identity in the insect olfactory system. This illustrates the point of our present modelling effort aimed to address the dynamical behaviours underlying both encoding strategies and compare their ability to encode ratio information. We found that the main advantage of the spatiotemporal code resides in holding more information by its improved specificity between ratios (Figure 6c), and the earlier time in which it reaches the maximum Euclidean distance between the ratio-specific trajectories (legend of Figure 2). The disadvantage is, however, that the potential collision between stimulus and network dynamics can degrade ratio specific information. This is particularly a problem for olfactory coding in moths, since highly dynamic odour plumes occur in the natural environment, generating a temporal structure that is very significant for anemotactic search [23,24].

We focused on the problem of a potential interference between the stimulus temporal patterns and the network dynamics and found that the LCA encoding of ratios can be indeed disrupted by inter-pulse intervals durations of a range that can occur in pheromonal odour plumes. The simulations show that LCA encoding can seriously fail in certain cases compared with FPA. The interference may arise when frequencies within the natural plume and network dynamics are in the same range. This is not a purely hypothetical issue since frequencies in natural odour plumes

have some overlap with those observed in the temporal patterns of PN recordings [23], which also match those found in the dynamics of our LCA model. The real MGC may be able to deal with this problem by having neurons with different time constants so as to ensure the precise encoding in the behaviourally relevant frequency range of stimulus using a LCA scheme. The simulations presented here were done using identical time constants for all the neurons of each type (PNs and LNs). This does not allow a triphasic (inhibition-excitation-inhibition) response pattern as observed in *M. sexta* MGC-PNs [48], except as a random network behaviour. Having a triphasic response pattern would also help to separate the pulses by resetting the responses before coding of the next odour pulse, preventing interference. Another factor that can potentially contribute to avoid interference in biological neural networks is the presence of an offset response to the stimulus that may allow the system to discriminate between blends in spite of collisions between the dynamics of the stimulus and those generated by the network. This type of offset response, described in the locust [49], depends on intrinsic properties of the cells that were not considered in our model. An additional possibility to preserve ratio encoding under complex stimulation patterns would be to rely upon FPA encoding strategies, or to use a combination of FPA and LCA dynamics working in parallel using different neuropils within the MGC.

The biological relevance of the computational simulations presented here can be appreciated in light of Mazor and Laurent's (2005) results in the locust AL. In this study [22], the authors recorded multiple PNs simultaneously while stimulating the antennae with long lasting pulses of odour blends. They found that odour representations can be described as trajectories in PN state space with a transient phase lasting 1–2 seconds, a stable fixed point attractor for about 8 seconds and a final off transient. The optimal stimulus separation occurred during the dynamic phase of the response rather than at the fixed point. Moreover, the period of maximum odour discriminability corresponds to the few hundreds of milliseconds following the stimulus, which is in accordance with behavioural evidence from the reaction time to odours in insects. The dynamical trajectory of the PN vector in the phase space is not only the most informative segment of the response, but it is also responsible for most of the increase in the total activity of the Kenyon cells, that are the targets of the PNs in the mushroom body [22]. The dynamical response that occurs before reaching the fixed point (see Figure 4 in [22]) strongly resembles the LCA dynamics we show in this paper (right panels of Figure 2-A and B), while the fixed points reached some seconds later resemble the FPA framework results (left panels of Figure 2-A and B). Regarding our LCA network, the time in which the trajectories reach maximum Euclidean distance is around 250 ms (legend of Figure 2), and we checked that they reach a fixed point (Figure S1) or a periodic orbit (not shown) after 0.5 to 1 second of simulation. This is similar to Mazor's observations, and differs from the "Winnerless Competition" framework in which a fixed point is never reached (see page 669 in [22]). The late fixed point shown by the LCA network is different from the early fixed point of the FPA network because it includes many LNs active at the same time instead of a single winner. Thus, the difference between both dynamics is not only how fast they can reach a fixed point. As explained above the first 0.5 seconds in which the two dynamics are radically different constitute the most relevant time window from a biological point of view.

In the context of our reductionist modelling approach, many details of MGC morphology and physiology were included as had been observed in the MGC of moths, e.g., the afferent input to the two classes of AL neurons, LNs and PNs, and their interconnections in the glomerular structure [13]. Although it is known that LN dendritic arborization is multiglomerular, more precise connectivity is not known, and our computational simulations test two possible connection arrangements and their respective consequent encoding schemes. Considering the same general architecture and set of synaptic weights, if the LNs' inhibition pattern is symmetric we get FPA dynamics, while an asymmetric connectivity leads to LCA. This is potentially a simple way to explain differences in the dynamics observed in different species that may share a general connectivity pattern in the odour processing networks. More precisely, our results predict that the total LN to LN connectivity should be roughly symmetrical in insects where the spatial coding of odour identity is prominent. Indeed, the odour-specific trajectories in the left panel of Figure 2 appear to follow similarly shaped paths to trajectories of glomerular activity observed in the honeybee [50]. This suggests that the total strength of inhibition between glomeruli should be symmetric. Conversely, in species where temporal patterns seem to be prominent, as the example of the locust mentioned above (e.g., compare the Figure 4 of [22] with the right panels of Figure 2), a more asymmetric inhibition between LNs would be expected. If we consider long term changes in the efficacy of some LN to LN synapses, this line of thinking can also offer possible explanations to learning related modifications in the network dynamics that we plan to address in our forthcoming research.

## Supporting Information

**Figure S1 Fixed point in LCA.** Long lasting LCA simulation showing that the dynamics reaches a fixed point at the end of the first second. The stimulus elapse is shown with a bar under the abscissa. Stimulus ratio was 0.5:0.5, and LN to LN connection probability 0.25.
(EPS)

## Acknowledgments

We thank to Dr. Fabiano Baroni for his useful comments about the model, and to Dr. Shannon B. Olsson and Dr. Linda Klueber for their help on the biological aspects.

## Author Contributions

Conceived and designed the experiments: KYC AC TCP. Performed the experiments: KYC AC SK. Analyzed the data: KYC AC SK. Contributed reagents/materials/analysis tools: KYC AC SK TCP. Wrote the paper: KYC AC TCP.

## References

1. Hansson BS Functional characteristics of the antennal lobe, Springer, chapter 5. pp 125–161.
2. Murlis J, Elkinton JS, Carde RT (1992) Odor plumes and how insects use them. Annual Review of Entomology 37: 505–532.
3. Baker TC, Haynes KF (1996) Pheromone-mediated optomotor anemotaxis and altitude control exhibited by male oriental fruit moths in the field. Physiological Entomology 21: 20–32.
4. Hartlieb E, Anderson P Olfactory-released behaviours, Springer, chapter 11. pp 315–349.
5. Valeur PG, Lofstedt C (1996) Behaviour of male oriental fruit moth, grapholita molesta, in overlapping sex pheromone plumes in a wind tunnel. Entomologia Experimentalis et Applicata 79: 51–59.
6. Kaissling K, Kramer E (1990) Sensory basis of pheromone-mediated orientation in moths. Verhandlungen der Deutschen Zoologischen Gesellschaft 83: 109–131.

7. Akers RP, O'Connell RJ (1988) The contribution of olfactory receptor neurons to the perception of pheromone component ratios in male redbanded leafroller moths. Journal of Comparative Physiology A-Neuroethology Sensory Neural and Behavioral Physiology 163: 641–650.
8. Hansson BS, Ljungberg H, Hallberg E, Lofstedt C (1992) Functional specialization of olfactory glomeruli in a moth. Science 256: 1313–1315.
9. Carlsson MA, Galizia CG, Hansson BS (2002) Spatial representation of odours in the antennal lobe of the moth spodoptera littoralis (lepidoptera : Noctuidae). Chemical Senses 27: 231–244.
10. Wu WQ, Anton S, Lofstedt C, Hansson BS (1996) Discrimination among pheromone component blends by interneurons in male antennal lobes of two populations of the turnip moth, *Agrotis segetum*. Proceedings of the National Academy of Sciences of the United States of America 93: 8022–8027.
11. Christensen TA, Mustaparta H, Hildebrand JG (1989) Discrimination of sex-pheromone blends in the olfactory system of the moth. Chemical Senses 14: 463–477.
12. Christensen TA, Hildebrand JG, Tumlinson JH, Doolittle RE (1989) Sex-pheromone blend of Manduca-sexta responses of central olfactory interneurons to antennal stimulation in male moths. Archives of Insect Biochemistry and Physiology 10: 281–291.
13. Hansson BS, Anton S (2000) Function and morphology of the antennal lobe: new developments. Annual Review of Entomology 45: 203–231.
14. Heinbockel T, Christensen TA, Hildebrand JG (2004) Representation of binary pheromone blends by glomerulus-specific olfactory projection neurons. Journal of Comparative Physiology A Neuroethology Sensory Neural and Behavioral Physiology 190: 1023–1037.
15. Chong KY (2007) Encoding of odour blends in the moth antennal lobe. PhD thesis, Department of Engineering, University of Leicester.
16. Rabinovich M, Huerta R, Volkovskii A, Abarbanel HDI, Stopfer M, et al. (2000) Dynamical coding of sensory information with competitive networks. Journal of Physiology-Paris 94: 465–471.
17. Homberg U, Christensen TA, Hildebrand JG (1989) Structure and function of the deutocerebrum in insects. Annual Review of Entomology 34: 477–501.
18. Akers RP, O'Connell RJ (1991) Response specificity of male olfactory receptor neurons for the major and minor components of a female pheromone blend. Physiological Entomology 16: 1–17.
19. Sun XJ, Tolbert LP, Hildebrand JG (1997) Synaptic organization of the uniglomerular projection neurons of the antennal lobe of the moth manduca sexta: A laser scanning confocal and electron microscopic study. Journal of Comparative Neurology 379: 2–20.
20. Carlsson MA, Hansson BS (2002) Responses in highly selective sensory neurons to blends of pheromone components in the moth agrotis segetum. Journal of Insect Physiology 48: 443–451.
21. Kárpáti Z, Dekker T, Hansson B (2008) Reversed functional topology in the antennal lobe of the male european corn borer. The Journal of Experimental Biology 211: 2841–2848.
22. Mazor O, Laurent G (2005) Transient dynamics versus fixed points in odor representations by locust antennal lobe projection neurons. Neuron 48: 661–673.
23. Vickers NJ, Christensen TA, Baker TC, Hildebrand JG (2001) Odour-plume dynamics influence the brain's olfactory code. Nature 410: 466–470.
24. Balkovsky E, Shraiman BI (2002) Olfactory search at high reynolds number. Proceedings of the National Academy of Sciences of the United States of America 99: 12589–12593.
25. Capurro A, Baroni F, Olsson S, Kuebler L, Karout S, et al. (2011) Complex blend coding in the moth antennal lobe emerges from balanced random networks. Submitted.
26. Shang Y, Claridge-Chang A, Sjulson L, Pypaert M, Miesenbo G (2009) Excitatory local circuits and their implications for olfactory processing in the fly antennal lobe. Cell 128: 601–612.
27. Root CM, Masuyama K, Green DS, Enell LE, Nassel DR, et al. (2008) A presynaptic gain control mechanism fine-tunes olfactory behavior. Neuron 59: 311–321.
28. Raman B, Joseph J, Tang J, Stopfer M (2010) Temporally diverse firing patterns in olfactory receptor neurons underlie spatiotemporal neural codes for odors. The Journal of Neuroscience 30: 1994–2006.
29. Av-Ron E (1994) Modeling olfactory neurons of the insect antennal lobe. Boston: Kluwer Academic Publishers. pp 173–178.
30. Av-Ron E, Rospars JP (1995) Modeling insect olfactory neuron signaling by a network utilizing disinhibition. BioSystems 36: 101–108.
31. Av-Ron E, Vibert JF (1996) A model for temporal and intensity coding in insect olfaction by a network of inhibitory neurons. Biosystems 39: 241–250.
32. Linster C, Masson C, Kerszberg M, Personnaz L, Dreyfus G (1992) A formal model of the insect olfactory macroglomerulus: simulations and analytical results. In: Giles C, Hanson S, Cowan J, eds. Advances in neural information processing systems, 5. Morgan Kaufmann. pp 239–252.
33. Linster C, Masson C, Kerszberg M, Personnaz L, Dreyfus G (1993) Computational diversity in a formal model of the insect olfactory macroglomerulus. Neural Computation 5: 228–241.
34. Linster C, Kerszberg M, C M Pheromone detection, ratio discrimination and oscillations: a new approach to olfactory coding., Kluwer Academic Publishers. pp 179–184.
35. Linster C, Dreyfus G (1996) A model for pheromone discrimination in the insect antennal lobe: Investigation of the role of neuronal response pattern complexity. Chemical Senses 21: 19–27.
36. Zavada A, Buckley C, Martinez D, Rospars J, Nowotny T (2011) Competition-based model of pheromone component ratio detection in the moth. PLoS ONE 6: 1–12.
37. Huerta R, Rabinovich M (2004) Reproducible sequence generation in random neural ensembles. Phys Rev Lett 93: 1–4.
38. Muezzinoglu MK, Vergara A, Huerta R, Nowotny T, Rulkov N, et al. (2008) Artificial olfactory brain for mixture identification. NIPS 2008: 1121–1128.
39. Muezzinoglu M, Huerta R, Abarbanel H, Ryan M, Rabinovich M (2009) Chemosensor-driven artificial antennal lobe transient dynamics enable fast recognition and working memory. Neural Computation 21: 1018–1037.
40. Joerges J, Kuttner A, Galizia CG, Menzel R (1997) Representations of odours and odour mixtures visualized in the honeybee brain. Nature 387: 285–288.
41. Laurent G, Stopfer M, Friedrich RW, Rabinovich MI, Volkovskii A, et al. (2001) Odor encoding as an active, dynamical process: Experiments, computation, and theory. Annual Review of Neuroscience 24: 263–297.
42. Afraimovich VS, Rabinovich MI, Varona P (2004) Heteroclinic contours in neural ensembles and the winnerless competition principle. International Journal of Bifurcation and Chaos 14: 1195–1208.
43. Rabinovich M, Volkovskii A, Lecanda P, Huerta R, Abarbanel HDI, et al. (2001) Dynamical encoding by networks of competing neuron groups: Winnerless competition. Physical Review Letters 87: 068102.
44. Stopfer M, Jayaraman V, Laurent G (2003) Intensity versus identity coding in an olfactory system. Neuron 39: 991–1004.
45. Geffen M, Broome BM, Laurent G, Meister M (2009) Neural encoding of rapidly fluctuating odors. Neuron 61: 570–586.
46. Rabinovich M, Huerta R, Laurent G (2008) Transient dynamics for neural processing. Science 321: 48–50.
47. Niessing J, Friedrich RW (2010) Olfactory pattern classification by discrete neuronal network states. Nature 465: 47–52.
48. Heinbockel T, Christensen TA, Hildebrand JG (1999) Temporal tuning of odor responses in pheromone-responsive projection neurons in the brain of the sphinx moth manduca sexta. Journal of Comparative Neurology 409: 1–12.
49. Brown SL, Joseph J, Stopfer M (2005) Encoding a temporally structured stimulus with a temporally structured neural representation. Nature Neuroscience 8: 1568–1576.
50. Galan RF, Sachse S, Galizia CG, Herz AVM (2004) Odor-driven attractor dynamics in the antennal lobe allow for simple and rapid olfactory pattern classification. Neural Computation 16: 999–1012.

# The Neural Correlates of Perceptual Awareness


Abstract

*The study of the neural correlates of awareness is nowadays an active research field in Neuroscience. This has been basically boosted by the study of neural correlates of conscious perception with single cell recordings in monkeys and voxel activities with human fMRI experiments. In this review, we discuss the main experiments with recording of single neurons and related evidence about the neural events underling visual perceptual awareness.*



Alberto Capurro[i] and Rodrigo Quian Quiroga[ii]
*University of Leicester*
*Department of Engineering*
*NeuroEngineering Lab*[iii]


Several researchers are now experimentally addressing the study of the neural correlates of the different aspects of consciousness. This issue was considered to be an exclusive matter of philosophy until a short time ago (Crick, 1994; Crick and Koch, 1995; Koch, 2004). Consciousness or awareness can, in principle, be defined as the occurrence of perceptions, thoughts and feelings (Sutherland, 1996). A precise definition, however, remains elusive, because covering every aspect of the conscious experience is difficult. For instance, speaking about the perception of something that we see and recognize is not the same as speaking about our self consciousness, or about the different levels of awareness that we experience during the sleep-wake cycle. To begin with, we must distinguish between the factors that enable consciousness to occur (such as the ascending activation system of the brainstem and basal forebrain, or the glutamatergic neurotransmission) from the so called content of consciousness, that is, the formation of specific percepts. In this review we will address this last issue through evidence of neural correlates underling visual perceptual awareness.


[i] ac331@leicester.ac.uk
[ii] rqqg1@leicester.ac.uk
[iii] LE1 7RH Leicester, United Kingdom
Tel / Fax: +44 (0)116 252 2314 / 2619
www.le.ac.uk/neuroengineering

# Perception and Neural Coding in the Visual Pathways

The processing of visual information in the cerebral cortex takes place through two hierarchically organized neural streams with extensive feedback. The dorsal or action pathway, going from the V1 area in the striate occipital cortex to the parietal and frontal cortices, processes information related to the position of an object as required for performing an action, such as reaching for a given target location. The ventral pathway, going from the V1 area to the infero-temporal (IT) cortex, is related to the recognition of objects, particularly faces and places (Ison and Quian Quiroga, 2008; Logothetis and Sheinberg, 1996; Mishkin et al., 1983; Tanaka, 1996).

Converging evidence from monkey recordings supports the notion that visual awareness is linked to the neural activity of the ventral visual stream (Logothetis, 1998; Tanaka, 1997). The preferred stimulus of the neurons increases in complexity and selectivity in successive hierarchical levels of the pathway. In V1, neurons respond to contours or edges with specific orientation. Cells having the same stimulus preferences are grouped into columns that occupy the entire thickness of the cortex. These columns are in turn grouped in functional units that examine contours in all orientations of their receptive fields with both eyes, covering the contra-lateral half of the space (Hubel, 1988). From V1 the information is conveyed to V2 and then to V4, where neurons have larger receptive fields and respond to angles and curves pointing in particular directions (Tanaka, 1996). At the top of the visual hierarchy, the IT cortex has even larger receptive fields that are not retino-topically organized but include the center of the gaze with the strongest response to stimuli presented in the projection of the fovea (Gross, 2008). In the IT cortex most neurons respond to complex stimuli, such as faces and hands, in a way that is often relatively invariant to changes in stimulus size, contrast, color and position within the receptive field (Gross, 2008). In the human brain, the ventral surface extending from the occipito-temporal border to the middle part of the temporal cortex is considered to be the homologue of the monkey IT cortex (Tanaka, 1997).

The IT cortex provides massive projections to the medial temporal lobe (MTL), which also receives input from multiple sensory modalities and is essential for declarative memory (Squire, Stark and Clark, 2004). The MTL includes the hippocampal region (CA fields, dentate gyrus, and subicular complex) and the adjacent perirhinal, entorhinal, and parahippocampal cortices. The main cortical input to the hippocampus is the entorhinal cortex, which receives projections from the peri-rhinal and parahippocampal cortices, which in turn receive projections from unimodal and polymodal areas in the frontal, temporal, and parietal lobes. Thus, the hippocampus lies at the end of a cortical processing hierarchy (Squire et al., 2004).

# Neural Responses in MTL

Patients suffering from MTL epilepsy refractory to medication may undergo the implantation of intracranial electrodes to determine the seizure focus and to evaluate the feasibility and potential outcome of a curative resection of the focus (e.g., Engel, 1996). Extra-cellular single unit recordings conducted in this type of patient led to the discovery of MTL neurons that responded selectively to visual stimuli from different categories, such as faces, landmarks and animals (Kreiman, Koch and Fried, 2000). A few years later, neurons that responded selectively to the identity of a given person were found (Quian Quiroga et al., 2005). For example, one neuron in the left hippocampus responded only to a variety of images of the actress Jennifer Aniston, and another neuron in the right hippocampus responded only to photos of Halle Berry and even to her written name. These results suggest that hippocampal neurons are encoding an abstract representation of a given individual known to the patient.

The remarkable degree of selectivity and invariance found in MTL neurons has led to the idea of a sparse and abstract representation of concepts (Ison and Quian Quiroga, 2008; Quian Quiroga, Kreiman, Koch and Fried, 2008a; Quian Quiroga, Reddy, Kreiman, Koch and Fried, 2005; Waydo, Kraskov, Quian Quiroga, Fried and Koch, 2006). These findings are in line with the classic concepts summarized in Barlow's five dogmas of perceptual physiology (Barlow, 1972), and particularly with the fourth dogma, which states that perception corresponds to the activity of a small selection of the very numerous high level neurons: "*Just as physical stimuli directly cause receptors to initiate neural activity, so the active high-level neurons directly and simply cause the elements of our perception". (380)*

This does not mean that any particular object is represented by only one specific cell, often referred as the "grandmother cell" (e.g., Barlow, 1994), but it seems conceivable that a relatively small set of highly specialized neurons that remain silent most of the time could be tuned to codify specific objects that are highly significant for the species, such as faces and homes in the case of humans, or flying bugs in the case of frogs (Quian Quiroga et al., 2008a). Indeed, the original idea of Jerry Lettvin (see appendix in Barlow, 1994) was that a cluster of "18000" units would encode a concept. Often used to remark on the unlikeliness of this concept, the single grandmother cell has been proposed as the theoretical extreme of a sparse representation. One of the main criticisms to the grandmother cell theory, however, is that there would not be enough cells to encode every possible percept, because the number of stimuli that can be encoded increases linearly with the number of cells. In addition, the death of only one particular cell would imply the loss of the encoded concept. So, although the brain may encode concepts using very sparse representations (Ison and Quian Quiroga, 2008; Quian Quiroga et al., 2008a; Quian Quiroga et al., 2005), it is clear that a one to one mapping is impossible.

# Neural Correlates of Visual Perception

A particularly interesting methodology that has been used to study the function of the ventral visual pathway is the presentation of visual stimuli that can be perceived in more than one way, as the case of binocular rivalry (Leopold and Logothetis, 1996; Logothetis, 1998; Logothetis, Leopold and Sheinberg, 1996; Logothetis and Sheinberg, 1996) and ambiguous pictures (Logothetis, 1998). These bi-stable (or multi-stable) stimulation paradigms constitute an invaluable tool for the study of visual perception, because they permit the dissociation of the neural responses that underlie what is perceived from the straight forward sensory representation of the visual pattern.

In the binocular rivalry paradigm, two different images are shown for each eye and the resulting percept does not correspond to a fusion of both but rather to an alternating perception of each of them (Logothetis, 1998). The perceived image changes spontaneously between both figures in a random manner, but a switch can be induced when a new image is presented, because the novel picture perceptually suppresses the other for a certain time. This effect, known as flash suppression (Wolfe, 1984), is extremely useful. It allows one to manipulate experimentally which image of the pair (that creates the bi-stable pattern) will capture the perception in a given moment.

Using binocular rivalry and flash suppression in monkeys trained to report their perception, Logothetis (1998) determined that some cells are activated by the actual visual pattern, while others are affected by the way in which the stimulus is perceived. The proportion of the latter type of cells increased in the higher processing stages of the visual system. For example they increased from 20% in V1, to 90% in IT neurons. Experiments with flash suppression in epileptic patients showed a similar picture in human MTL: two out of three neurons modulated their activity according to the perceived stimulus (Kreiman, Fried and Koch, 2002).

Results obtained with fMRI techniques in humans usually parallel the results of studies using single cell recordings in monkeys (for a comprehensive review see Kanwisher, 2001). For example, regions of the human visual cortex, such as the fusiform face area and the parahippocampal place area, were activated specifically by the perception of faces (Kanwisher, McDermott and Chun, 1997) and images of places (Epstein and Kanwisher, 1998), respectively. Studies with binocular rivalry have shown that the neural activation was correlated with the content of the subject's awareness and not with the retinal input (Kanwisher, 2001).

Using single cell recordings in patients, a different experiment was recently designed to assess if a neuron was activated just by a given image or by its conscious recognition (Quian Quiroga et al., 2008b). To this end, the presentation time of the image was controlled through stimulus masks, and photos eliciting responses were shown very

briefly, such that they were sometimes recognized and sometimes not. Interestingly, although the stimulus was exactly the same, the neurons fired only when a photo was recognized by the patient and remained mostly silent when it was not. Furthermore, the duration of the responses did not increase with the stimulus duration. Thus, we can conclude that the firing of these neurons strongly correlates with the conscious recognition of the photos. These results parallel the observations of Grill-Spector using fMRI (Grill-Spector, Kushnir, Hendler, and Malach, 2000), and support the idea that the higher visual areas respond mainly to the image that is actually perceived.

Given clinical and lesion studies about the function of the hippocampus and surrounding areas (e.g., Squire et al., 2004) and the long latency of the MTL responses (300 ms) (Mormann et al., 2008) compared to the latencies reported for picture recognition (150 ms) (Thorpe, Fize and Marlot, 1996), it is likely that MTL neurons are not performing the recognition process itself. The fact that they are mainly modulated by conscious perception is in line with the interpretation that these cells may be underlying the link between consciously perceived inputs and long-term memory (Quian Quiroga et al., 2008a; Quian Quiroga, Mukamel, Isham, Malach and Fried, 2008b). Indeed, to form an abstract representation that could be memorized, neurons must encode the identity of the individual in an abstract manner, and this is achieved through an invariant response. Based on these findings, it seems plausible that MTL neurons play a key role in the transformation of visual percepts into long term abstract memories, and in the recollection of memory traces related to a concept (Ison and Quian Quiroga, 2008; Quian Quiroga et al., 2008a). In line with these ideas, a recent report has shown that neurons in the hippocampus and entorhinal cortex that were specifically activated during the display of short films also responded during the free recall of the same sequences by the patients (Gelbard-Sagiv, Mukamel, Harel, Malach and Fried, 2008).

## Causal Relations Between Neural Activity and Awareness

The evidence that neural activity in the ventral stream is correlated with visual perception of faces or places leads to the issue of the underlying causal structure (Kanwisher, 2001). In other worlds, is there a causal relationship between neuronal firing and perception, or just mere correlation? Evidence for a causal connection was provided by experiments using cortical micro-stimulation in a cluster of face neurons of monkeys trained to report the presence of a face in images degraded by visual noise (Afraz, Kiani and Esteky, 2006). When the cluster of face neurons was stimulated, the monkeys were more likely to report faces, even when only visual noise was presented. This effect was restricted to the area in which face neurons were located and to the time window in which they responded to the face. In line with these findings, previous studies in epileptic patients reported that cortical micro-stimulation in fusiform electrode sites with face selective responses produced perceptual experiences of a face (Puce, Allison and McCarthy, 1999).

These experimental results imply that the activation of brain areas where the perceptual representation occurs can bias perception. The activation of such areas, however, may not always be sufficient or be the cause of conscious perception. As discussed by Kanwisher (2001), subjects could be unaware of the low contrast grid stimulation that evoked clear fMRI responses in V1-V4. Similarly, people did not report having perceived briefly presented angry or happy faces (masked with neutral expression faces) although the angry faces evoked a significantly larger activation of the amygdala (Whalen, Rauch, Etcoff, McInerney, Lee and Jenike, 1998). There also exists considerable evidence in psychological research indicating that stimulus information can affect measures of forced-choice discrimination even when it is not consciously perceived (Merikle, Smilek, and Eastwood, 2001). What else is needed for conscious awareness? Of many proposed suggestions, Baars has offered the simpler idea that certain strength of activation may be required (1998). In this context, non-conscious representations could be explained in terms of sub-threshold activations. The threshold does not need to be a clear cut edge but a range of values that may also depend on attention levels. In this threshold range, the perception might not be conscious but the information contained in the stimulus could still be influential in a forced choice, or could condition perceptions related to another supra-threshold stimulus. In addition to this strength activation hypothesis, it has been suggested that a focal representation may also have to be accessible to other parts of the brain in order to reach awareness (Kanwisher, 2001). Indeed, a local activation pattern can rapidly reach distant areas of the neocortex through long range connections. According to Buzáki (2007), in order to enter in the conscious experience, environmental inputs would need to reach a long enough duration and intensity to extend beyond local circuits and perturb the ongoing rhythmic activity of the brain. In the specific case of visual awareness, connections within the IT cortex and executive parts of the brain, as prefrontal and anterior cingulated cortices, are likely to be involved (Koch, 2004). However, the specific locus that would be needed for awareness remains an open discussion because perceptual representations are present in multiple cortical areas. This issue is related to the so called binding problem outlined in the next section.

## The Binding Problem and Neural Oscillations

The problem of how a visual scene composed of different objects is combined to form a unified perceptual experience is known as the binding problem (for example, Roelfsema, 2006).

The idea of binding can be applied to many levels, from grouping parts of the visual field into particular objects, to the combination of these objects into a complete visual scene, and the integration of stimuli coming from different sensory modalities in a unified perceptual experience.

In the visual pathways, different attributes of the image, such as color, orientation, size, distance and movement are mapped in parallel pathways. In a first step of binding,

known as pre-attentive process, selected aspects of these feature maps converge in a bottom-up manner into a coherent map that contains the distinction of objects from the background. After that, the focus of attention can highlight selected parts of this unified map by referring back to the feature maps in a serial and top-down manner (Treisman, 1986).

The detailed neuronal mechanisms underlying the different steps of perceptual binding are an open issue at present. It has been suggested that this binding could be constructed through the correlated firing of the neurons that respond to the properties of the different elements that compose an object. This correlated firing could be achieved through coherent oscillations of neural assemblies in the gamma frequency (35-75 Hz) (Eckhorn et al., 1988; Gray and Singer, 1989). This idea can be extended to the binding of a whole perceptive scene. Then, gamma oscillations may constitute a neural correlate for visual awareness through the activation of a network able to join together relevant aspects of the existing information into a coherent percept (Crick and Koch, 1990). Alternatively, such binding could be just represented by the activity of a cell population, with coherent oscillations playing little or no roll at all (Shadlen and Movshon, 1999). The relevance of gamma oscillations for perceptual binding has been a topic of active research and controversy in neuroscience (for example, Gray, 1999; Shadlen and Movshon, 1999).

Independent of the fact that oscillations or single cell firing are the basis of perception, another question presents itself. Where does this binding actually takes place? In other words, is there a "reader" of this activity? A simple answer is that the neurons of the following step in the visual hierarchy could be performing this reading. This is in line with Barlow's idea of a relatively small population of "cardinal" neurons, which when activated, would cause the perceptual experience (Barlow, 1972). As an alternative proposal, it has been suggested that perception is not linked to single cells but to field oscillations in an extended mass of tissue. In this conception, coherent gamma oscillations could be organized as spatiotemporal fields that may represent the contents of consciousness (Freeman, 2007). Since the field oscillations are sustained by networks of cells, both hypotheses do not necessarily exclude each other completely. After all, the idea of a cell or process to which consciousness would be attached is not new (for example, James, 1890). Although nowadays we understand many more details about the physiological processes involved in neural function, the basic quest outlined in the prophetic writings of James seems to remain essentially the same. As remarked by Crick (1994), the key difference is that we are now able to address this question experimentally.

## References


Afraz, S-R., Kiani, R., & Esteky, H. (2006). Microstimulation of inferotemporal cortex influences face categorization**.** *Nature*, 442, 692-695.

Baars, B. (1988). *A cognitive theory of consciousness*. Cambridge: Cambridge University Press.

Barlow, H.B. (1972). Single units and sensation: A neuron doctrine for conceptual psychology? *Perception*, 1, 371-394.

Barlow, H.B. (1994). The neuron doctrine in perception. In M. Gazzaniga (Ed.), *The Cognitive Neurosciences*. (pp. 415-435). Boston: MIT press.

Buzáki, G. (2007). The structure of consciousness. *Nature*, 446, 267.

Crick, F. (1994). *The astonishing hypothesis*. NY: Touchstone.

Crick, F., & Koch, C. (1990). Towards a neurobiological theory of consciousness. *Seminars in the Neurosciences*, 2, 263-275.

Crick, F., & Koch, C. (1995). Why neuroscience may be able to explain consciousness? *Scientific American*, 273, 84-85.

Eckhorn, R., Bauer, R., Jordan, W., Brosch, M., Kruse, W., Munk, M., & Reitboeck, H.J. (1988). Coherent oscillations: A mechanism of feature linking in the visual cortex? Multiple electrode and correlation analyses in the cat. *Biological Cybernetics*, 60, 121-130.

Epstein, R., & Kanwisher, N. (1998). A cortical representation of the local environment. *Nature*, 392, 598-601.

Engel, J. (1996). Surgery for seizures. *New Eng J Med*, 334, 647-652.

Freeman, W.J. (2007). 2007 Special Issue: Indirect biological measures of consciousness from field studies of brains as dynamical systems. *Neural Networks*, 20, 1021-1031.

Gelbard-Sagiv, H., Mukamel, R., Harel, M., Malach, R., & Fried, I. (2008). Internally generated reactivation of single neurons in human hippocampus during free recall. *Science* , 322, 96-101.

Gray, C.M., & Singer, W. (1989). Stimulus-specific neuronal oscillations in orientation columns of cat visual cortex. *PNAS USA*, 86, 1698-1702.

Gray, C.M. (1999). The Temporal Correlation Hypothesis of Visual Feature Integration: Still Alive and Well. *Neuron*, 24, 31-47.

Grill-Spector, K., Kushnir, T., Hendler, T., & Malach, R. (2000). The dynamics of object-selective activation correlate with recognition performance in humans. *Nature Neuroscience*, 3, 837-893.

Gross, C.G. (2008). Single neuron studies of inferior temporal cortex. *Neuropsychologia*, 46, 841-852.

Hubel, D.H. (1988). *Eye, brain, and vision*. New York: Scientific American Books.

Ison, M.J., & Quian Quiroga, R. (2008). Selectivity and invariance for visual objects perception. *Frontiers in Bioscience***,** 4889-4903.

James, W. (1890). *The Principles of Psychology*. New York: Dover Publications.

Kanwisher. N, McDermott, J., & Chun, M.M. (1997). The fusiform face area: a module in human extrastriate cortex specialized for face perception. *Journal of Neuroscience*, 17, 4302-4311.

Kanwisher, N. (2001). Neural events and perceptual awareness. *Cognition*, 79, 89-113.

Koch, C. (2004). *The Quest for Consciousness*: *A Neurobiological Approach*. Englewood: Roberts & Company.

Kreiman, G., Koch, C., & Fried, I. (2000). Category-specific visual responses of single neurons in the human medial temporal lobe**.** *Nature Neuroscience*, 3, 946-953.

Kreiman, G., Fried, I., & Koch, C. (2002). Single-neuron correlates of subjective vision in the human medial temporal lobe**.** *PNAS*, 99, 8378-8383.

Leopold, D.A., & Logothetis, N.K. (1996). Activity changes in early visual cortex reflect monkeys' percepts during binocular rivalry. *Nature*, 379, 549-553.

Logothetis, N.K., Leopold, D.A., & Sheinberg, D.L. (1996). What is rivaling during binocular rivalry? *Nature*, 380, 621-624.

Logothetis, N.K., & Sheinberg, D.L. (1996). Visual object recognition. *Annual Review of Neuroscience* , 19, 577-621.

Logothetis, N.K. (1998). Single units and conscious vision. *Philosophical Transactions of the Royal Society B: Biological Sciences*, 353, 1801-1818.

Merikle, P.M., Smilek, D., & Eastwood, J.D. (2001). Perception without awareness: perspectives from cognitive psychology. *Cognition*, 79, 115-134.

Mishkin, M., Ungerleider, L.G., & Macko, K.A. (1983). Object vision and spatial vision: Two cortical pathways. *Trends in Neurosciences*, 6, 414-417.

Mormann, F., Kornblith, S., Quian Quiroga, R., Kraskov, A., Cerf, M., Fried, I., & Koch, C. (2008). Latency and selectivity of single neurons indicate hierarchical processing in the human medial temporal lobe. *Journal of Neuroscience*, 28, 8865-8872.

Puce, A.., Allison, T., & McCarthy, G. (1999). Electrophysiological studies of human face perception. III. Effects of top-down processing on face-specific potentials. *Cerebral Cortex*, 9, 445-458.

Quian Quiroga, R., Reddy, L., Kreiman, G., Koch, C., & Fried, I. (2005). Invariant visual representation by single neurons in the human brain**.** *Nature*, 435, 1102-1107.

Quian Quiroga, R., Kreiman, G., Koch, C., & Fried, I. (2008a). Sparse but not "Grandmother-cell" coding in the medial temporal lobe. *Trends in Cognitive Sciences***,** 12, 87-91.

Quian Quiroga, R., Mukamel, R., Isham, E., Malach, R., & Fried, I. (2008b). Human single neuron responses at the threshold of conscious recognition. *PNAS*, 105, 3599-3604.

Roelfsema, P.R. (2006). Cortical algorithms for perceptual binding. *Annu. Rev. Neurosci.*, 29, 203-227.

Shadlen, M.N., & Movshon, J.A. (1999). Synchrony unbound: A critical evaluation of the temporal binding hypothesis. *Neuron*, 24, 67-77.

Squire, L.R., Stark C.E.L., & Clark, R.E. (2004). The medial temporal lobe. *Annual Review of Neuroscience*, 27, 279-306.

Sutherland, S. (1996). *The International Dictionary of Psychology*. US: Crossroad Publishing Co.

Tanaka, K. (1996). Representation of visual features of objects in the inferotemporal cortex. *Neural Networks*, 9, 1459-1475.

Tanaka, K. (1997). Mechanisms of visual object recognition: monkey and human studies. *Current Opinion in Neurobiology*, 7, 523-529.

Thorpe, S., Fize, D., & Marlot, C. (1996). Speed of processing in the human visual system. *Nature*, 381, 520-522.

Treisman, A. (1986). Features and objects in visual processing. *Scientific American*, 255, 114-125.

Waydo, S., Kraskov, A., Quian Quiroga, R., Fried, I., & Koch, C. (2006). Sparse representation in the human medial temporal lobe. *Journal of Neuroscience*, 26, 10232-10234.

Whalen, P.J., Rauch, S.L., Etcoff, N.L., McInerney, S.C., Lee, M.B., & Jenike, M.A. (1998). Masked presentations of emotional facial expressions modulate amygdala activity without explicit knowledge. *Journal of Neuroscience*, 18, 411–418.

Wolfe, J.M. (1984). Reversing ocular dominance and suppression in a single flash. *Vision Research*, 24, 471-478.